DOTTORATO DI RICERCA IN INGEGNERIA GEOTECNICA
XX CICLO
Anno 2008

"Stability and strength analysis of leaning towers"

by

Michela Marchi

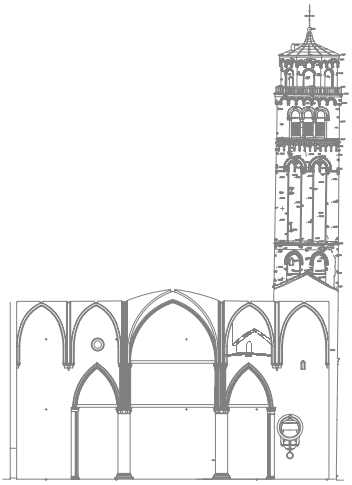

Supervisor: *Prof. Guido Gottardi,* UNIVERSITA' DEGLI STUDI DI BOLOGNA

Co-supervisors: *Prof. Roy Butterfield,* SOUTHAMPTON UNIVERSITY
Prof. Renato Lancellotta, POLITECNICO DI TORINO

A thesis submitted for the degree of Doctor of Philosophy at the University of Padova
January, 2008

UNIVERSITÀ DEGLI STUDI DI PARMA

ALMA MATER STUDIORUM
UNIVERSITÀ DI BOLOGNA

ABSTRACT

Stability and strength analysis of leaning towers

A thesis submitted for the degree of Doctor of Philosophy

Michela Marchi

Dottorato di ricerca in Ingegneria Geotecnica, XX ciclo
Università degli studi di Parma
January, 2008

Many ancient towers are afflicted by stability problems. The evaluation of the overall safety of historical towers is one of the most important items in the preservation of the national and worldwide artistic heritage. This thesis is concerned with models appropriate for the stability assessment of tower foundations, which is related to: bearing capacity failure, due to lack of soil strength, and instability of equilibrium, due to lack of soil stiffness. Both of these hazards are tackled using a work-hardening plasticity model for surface footings.

New developments have been introduced into the foundation modelling in relation to prediction of displacements and creep behaviour. These improvements have been used develop a methodology that can deal in a unified way with the two major failure mechanisms of such foundations.

Finally, a new interpretation of the influence of creep on tower stability is explained. Such an analysis provides not only a complete framework within which both possible collapse mechanisms can be assessed but also a prediction of which of them is most likely to occur.

The analysis, which has been developed in the form of a Mathematica notebook, and applied to the Pisa Tower and the Santo Stefano bell tower, can be also used to study the influence of foundation strengthening procedures.

Contents

C H A P T E R 4
A contribution to stability analysis of towers

PART III ***--Applications to real cases--***

C H A P T E R 5
Using Mathematica in soil-structure interaction

Introduction

Background

It is rather common whilst travelling or simply walking around a town (especially an italian one) to notice an ancient tower, and not infrequently the inclination of the structure may appear dangerous.

In fact, the Italian peninsula is full of historical towers, built with different objectives: bell towers, civic towers, chimneys, the watch towers of city walls, etc. A considerable number of structural configurations have arisen as a consequence of the great variety of purposes served by them. In many cases they became a distinctive features of their historical centres so that evaluation of the overall safety of historical towers is one of the most important points in the preservation of the national and worldwide artistic heritage.

Structural and foundation behaviour are both areas where our understanding needs to be improved if we are to reduce uncertainty in their lifespan. The two major collapse mechanisms of tower foundations are bearing capacity failure, due to lack of soil *strength*, and instability of equilibrium, due to lack of soil *stiffness*. The study proposed in the thesis, which gained its initial impetus from the analysis of some historical bell towers in Venice, is an attempt to include in one single framework, an analysis of these two mechanisms: problems that are usually separately treated. Such a generalised intepretation of the overall stability of a tower would constitute a considerable advance in predicting their behaviour.

Aim and Objectives

The thesis is concerned with the possible collapse mechanisms of leaning towers. Whilst maintaining a balanced approach to leaning tower modelling it aims to extend knowledge of analytical techniques in two key areas:

- foundation modelling (with the addition of creep),
- soil-structure interaction,

The purpose of this approach is to achieve understanding of, and confidence in, our estimates of all the components affecting the response of ancient towers.

The ***foundation modelling*** is tackled by using strain hardening plasticity theory, capable of predicting the strength and stiffness of the soil-foundation system. An important objective of this thesis was to extend (in relation to both hardening laws and plastic potentials) the formulation of elasto-plastic models for surface pads, to deal consistently with the tower behaviour. The investigation of the response of such old tower foundations is generally related to the viscous behaviour of soils, consequently, ***creep*** has become a significant ingredient of the work.

The ***soil structure interaction*** is herein treated in relation to towers. In particular, an analytical methodology is introduced to deal consistently with the two major collapse mechanisms of tower foundations: bearing capacity failure, due to lack of soil *strength*, and instability of

equilibrium, due to lack of soil *stiffness*. The latter, more developed in the structural field than in geomechanisc, is an important component of the soil-structure interaction.

Outline of the thesis

The outline of this thesis follows 3 main steps: the *review of case histories and theoretical analysis*, summarised in *PART I*, the *theoretical contribution* in *PART II* and the *applications to real cases* in *PART III*. The whole work has been conducted using *Mathematica*, from the numerical elaboration to the writing up of the results. The Most of the diagrams, shown in the treatment, are developed using this program, numerical integration of the model and application to real cases are elaborated into independent *Mathematica Notebooks.*

Review of case histories and theoretical analysis (PART I): **Chapter 1** collects some case histories of italian towers. A selection of few, but significant case histories has been made: the Pisa Tower; Venetian bell Towers, in particular Santo Stefano bell tower, the latter provided the first input for the development of this work. The information reported is related to the history of the construction, structural peculiarities and soil characteristics. Both Pisa tower and Santo Stefano will be used in the final part of the work as examples for the application of the model developed in the central part of the thesis. **Chapter 2** contains a literature review of analysis techniques relevant to the two distinct mechanisms identified for tower foundations: (1) *bearing capacity failure*, due to lack of strength of the soil and (2) *instability of equilibrium*, due to lack of stiffness. A different aspect, which does not involve foundation and soil, is the stability of masonry walls. Such 'material failure' is not discussed, since it lies completely outside the scope of geotechnical modelling. Nevertheless, ancient and old towers, in the presence of weak and disconnected masonry, can suffer sudden catastrophic failure, as attested by the collapse of the San Marco bell tower, in Venice in 1902 . The bearing capacity of foundations is discussed using both the classical and interaction diagram approaches. In addition, this chapter includes a review of literature related to the instability of equilibrium of the soil-structure interaction of tall structures. The central part of chapter 2 concentrates on work hardening plasticity models for surface pads. Results coming from these models establish a link between the two simple collapse mechanisms. This is one of the key points of the work and is the reason why these models have been expanded and modified in relation to the tower behavior, in Chapters 3.

Theoretical contribution (PART II): The central unit of the thesis, including Chapter 3, on foundation modelling, and Chapter 4, on soil structure interaction, contains analytical contributions specific to the performance of towers. **Chapter 3** deals with novel extensions of the work hardening plasticity models for surface pads. In particular, this chapter explains the origin and development of "universal load-path" plastic potentials for predicting the displacements of surface pads subjected to combined load. It also includes discussion of modified hardening rules, a new method of estimating a vertical stiffness curve from oedometer tests and a new methodology to incorporate a creep process (using the model developed by Bjerrum in the 7th Rankine Lecture) within the foregoing model, in order to obtain a useful and realistic representation of the response of campanile over time. The numerical integration of the model has been developed in the *Mathematica* environment as explained in **Appendix A**. A numerical model incorporating all these developments has been used to generate the M-θ curve used for the analysis developed in **Chapter 4**. In the latter a comprehensive analytical tool is introduced that can deal with the two major collapse mechanisms of towers foundations, bearing capacity failure, and instability of equilibrium. Both of these problems, are tackled using a work-hardening plasticity model for surface footings. Such an analysis provides not only a complete framework within which both possible collapse mechanisms can be assessed but also a prediction of

which of them is most likely to occur. A new interpretation of creep influence on tower stability is finally explained, on the basis of the new model proposed in chapter 3.

Applications to real cases (PART III): **Chapter 5** contains the whole elaborated methodology applied, in the form of a Mathematica Notebook, to two case histories: Pisa Tower and Santo Stefano bell tower. Results of the analysis are shown and discussed in this chapter, whilst the notebooks are provided as runnable examples. For completeness the printed notebook is shown in **Appendix B**. This final chapter is significant because it both summarises and applies the main contributions of the thesis.

PART I - *Review of case histories and theoretical analysis*

CHAPTER 1

Case histories

Figure 1.1. Large-scale panoramic view of Venice, by Friedrich Bernhard Werner, 3rd Quarter 18th Century (From: http://www.georgeglazer.com/maps/europe/werner/werner-venetia.html)

"Knowing the past to project the future"
Anonym (From http://torre.duomo.pisa.it/towersposters/english_version/)

Introduction

— The Italian peninsula is full of historical towers, built with different objectives: bell towers, civic towers, chimneys, the watch towers of city walls, etc. A considerable number of structural configurations have arisen as a consequence of the great variety of purposes served by the towers. In many cases they became a distinctive features of their historical centres so that evaluation of the overall safety of historical towers is one of the most important points in the preservation of the national and worldwide artistic heritage. In this chapter some historical italian towers are presented. A selection of few, but significant case histories has been made: the Pisa Tower, whose fame is unnecessary to recollect; Venetian bell Towers, in particular San Marco, Frari and Santo Stefano bell towers, the latter provided the first input for the development of this work; and Bologna's two towers: Garisenda and Asinelli, symbols of the town. The reported information is related to the history of the construction, structural peculiarities and soil characteristics. Both Pisa tower and Santo Stefano will be used in the final part of the work as examples for the application of the model developed in the central part of the thesis.

1.1 Pisa Tower

A wide study of the Pisa Tower (Figure 1.2) has been made over many centuries, especially in the second half of the last century, before the geotechnical intervenction conducted in 1999. Many official documents have been published in different ways, all the following information comes from the comprehensive review published by the Italian Ministery [Various Authors (2006)] and the official website of the Tower [http://torre.duomo.pisa.it/].

Figure 1.2. The Pisa Tower and the Cathedral (Piazza dei Miracoli, September 2007)

1.1.1 History and characteristics of the Tower

Construction history

- The Tower was constructed in the course of about 200 years
- The history of the building works is only partially documented, and has been reconstructed on the basis of indirect sources
- Work on the foundation began on 9 August 1173.
- The third order had only just been completed when, in c. 1178, the building works were suspended.
- Around 1272 the construction was recommenced, only to be interupted again, at the level of the 7th cornice, in c. 1278.
- The construction of the belfry (8th order) began around 1360 and was completed c. 10 years later.
- The Tower has subsided vertically by c. 2.8m as a result of the unstable nature of the underlying ground. The catino at the base was excavated in 1838 to bring to light the bases of the columns which had sunk underground.
- The differential subsidence is 1.89m; this means that the extreme north and south have subsided by 1.86m and 3.75m respectively.

Characteristics of the Tower

- The height of the building from the foundations to the belfry is c. 60m
- The ring shaped foundation has an external diameter of 19.6m
- The Tower weighs c. 142 MN
- The Tower is shaped like a hollow cylinder (Figure 1.3) formed by two concentric walls (in marble blocks) which contain mortar and other matter
- A spiral stair within the cylindrical body allows access to the arcaded storeys and to the summit of the tower
- The current inclination is c. 5½ degrees towards the south

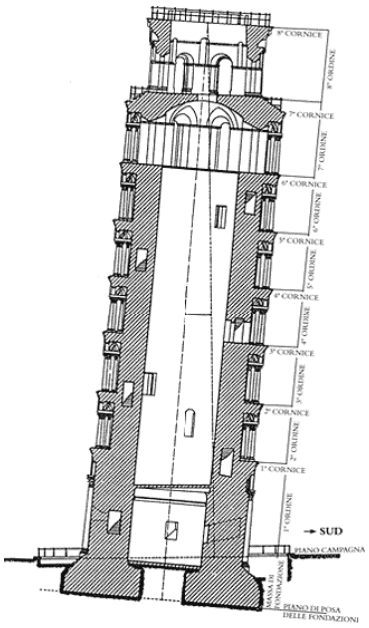

Figure 1.3. Section of the Tower

1.1.2 History of the inclination

During construction

The Tower was constructed in three stages punctuated by long periods of inactivity. The inclination towards the south manifested itself in the second stage (1272-1278), as can be deduced from the curve towards north of the axis of the Tower. This is the result of adjustments made by the builders to reduce the extent to which the building became distanced from the vertical. The correction attempted in 1360, during construction of the belfry, is also evident: here the base, which was then horizontal, has six steps to the south and only four to the north; this corresponds to the correction of a rotation towards south of about one and a half degrees.

In past centuries

The evolution of the inclination of the Tower over time can be reconstructed only summarily on the basis of a fresco painting executed by Antonio Veneziano in 1384 (Life of San Ranieri), which shows the Tower visibly leaning, and three measurements of the projection executed respectively by Vasari in 1550, Cresy and Taylor in 1817 and Rouhault de Fleury in 1859, using a plum line lowered from the 7th cornice. Comparing the two measurements made in the XIX century leads to the hypothesis of a relatively rapid rotation in concurrence with the excavation of the catino at the foot of the Tower undertaken by Alessandro della Gherardesca in 1838-1839. However, it is not possible to ascertain whether, before that moment, the Tower stayed still or maintained a slow rotation towards the south.

The XX century

In 1911 the first measurements of the tower with instruments and methods capable of accurately following the course of the Tower's inclination began. The inclination measured in 1911 was 5°14'46", corresponding to a projection of 4.22m from the seventh cornice to the first. The first surveys were based on the measurement of the angle "θ" between the first cornice and the seventh, using a theodolite placed at a precise point. Later (1928), four benchmarks were placed on the base of the Tower, from the levels of which the value of the inclination could be deduced. In 1934 a pendulum was introduced within the hollow cylinder and a highly accurate spirit level was placed in the instrument room at the 1st order. Finally, in 1992, an electronic monitoring station was installed, with automatically recording inclinometers which allow the real time transmission at the frequency intervals required (even every 4 minutes if necessary) of the values north-south and east-west of the inclination. With the help of instruments it is also possible to distinguish the movement of the base upon which the tower rests through analysis of deformations in the upper structure, in order to identify the effects of single causes, potentially of brief duration, such as winds and seismic activity. The diagram below shows the inclination of the Tower over time, reconstructed according to measurements taken in the XX century. This confirms the great sensitivity of the Tower to any variation in the ground conditions and to works undertaken at the base. Leaving to one side variations caused by specific occurrences, the rotation speed of the Tower has accelerated from 4" per year in the 1930s to 6" per year at the end of the 1980s.

The complete history of construction and rotations is shown in Figure 1.4 and the recent evolution of rotation, since 1911, in Figure 1.5.

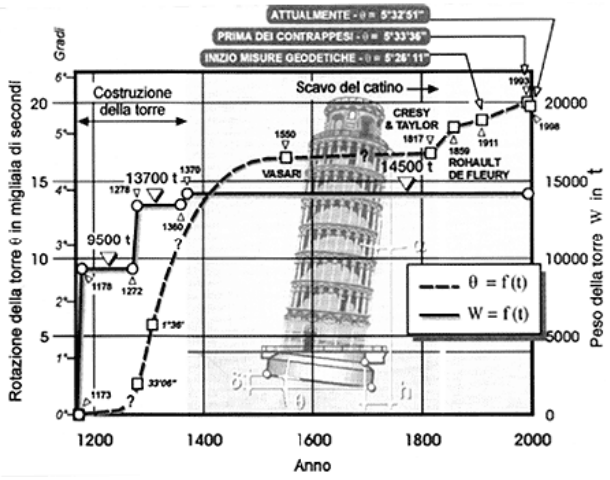

Figure 1.4. Rotation and history of construction of the Pisa Tower.

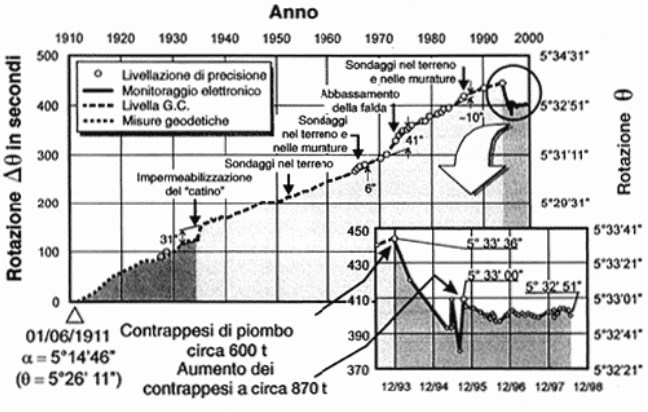

Figure 1.5. Rotation of the Pisa Tower since 1911

1.1.3 Foundation soil profile

Stratigraphy

The subsoil of the entire plain of Pisa is composed of geologically recent lagoon and marsh deposits (Pleistocene-Oligocene). Following extended investigations undertaken since the beginning of the XX century, the materials present in the subsoil beneath the Tower are well known (Figure 1.5).

• Between ground level and a depth of about 10 m (complex A): sands and silts with irregular stratifications, but with a prevalence of clayey silts under the southern part of the Tower (it is maintained that this is the cause which led to the inclination of the monument).

• Between 10 and circa 40 m depth (complex B): soil composed primarily of soft clays with an interlying layer of sand. The upper surface of the clay, more or less horizontal over all of the square, is depressed by more than two metres underneath the Tower; this is a deformation induced over the centuries by the weight of the Tower. This fact leads to the estimation that the overall subsidence of the Tower is between 2.5 and 3 metres.

• Below 40 m depth (complex C): dense sands

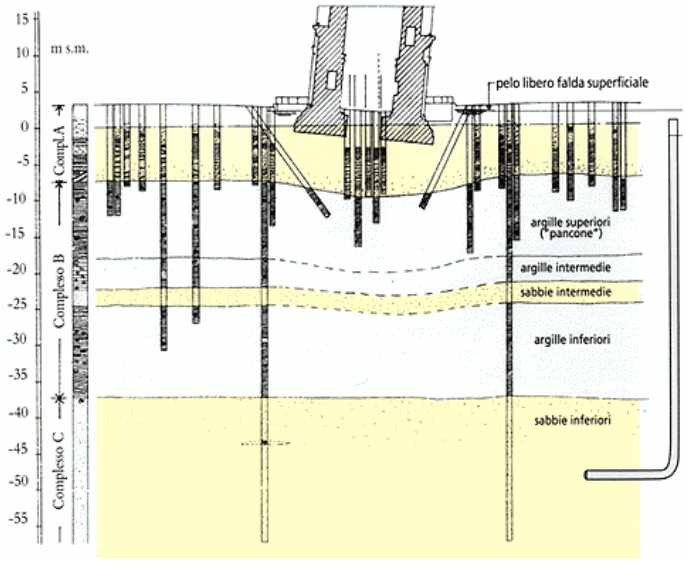

Figure 1.6. Schematic stratigraphic section of the subsoil of the Tower

1.1.4 Geotechnical intervention

Temporary stabilisation of the foundations was achieved during the second half of 1993 by the application of 600 tonnes of lead weights to the north side of the foundations via a post-tensioned removable concrete ring, cast around the base of the Tower at plinth level. This caused a reduction in inclination of about one minute of arc and, more importantly, reduced the overturning moment by about 10%. In September 1995 the load was increased to 900 tonnes in order to control the movements of the Tower during an unsuccessful attempt to replace the unsightly lead weights with temporary ground anchors. The masonry problem was tackled in 1992 by binding a few lightly post-tensioned steel tendons around the tower at the first cornice and at intervals up the second storey.

A permanent solution was sought that would result in a small reduction in inclination by half a degree, which is not enough to be visible but which would reduce the stresses in the masonry and stabilise the foundations. Given that the foundation of the Tower was on the point of instability and that any slight disturbance to the ground on the south side would almost certainly trigger collapse, finding a method of reducing the inclination was far from straightforward and gave rise to many heated debates within the Commission. Many possible methods of inducing controlled subsidence of the north side were investigated. These included drainage by means of wells, consolidation beneath the north side by electro-osmosis and loading the ground around the north side of the Tower by means of a pressing slab pulled down by ground anchors. None of these methods proved satisfactory.

A method known as soil extraction gradually evolved. This involves installing a number of soil extraction tubes adjacent to and just beneath the north side of the foundation (Figure 1.7). The method had been successfully used previously, notably to reduce the damaging differential settlements within the Metropolitan Cathedral of Mexico City.

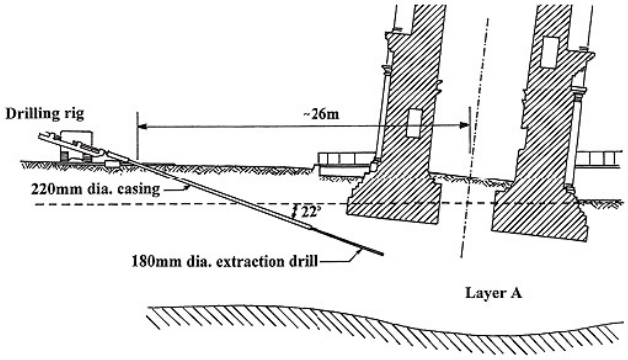

Figure 1.7. Scheme of the the intervention of sub excavation

In April 1996 the Commission agreed to carry out limited soil extraction from beneath the Tower with a view to observing its response.

The success of preliminary soil extraction persuaded the Commission that it was safe to undertake full soil extraction over the full width of the foundations. Accordingly, between December 1999 and January 2000, 41 extraction holes were installed at 0.5 m spacing, with a dedicated auger and casing in each hole. Full soil extraction commenced on 21 February 2000 and the results of both preliminary and full soil extraction are shown in Figure 1.8.

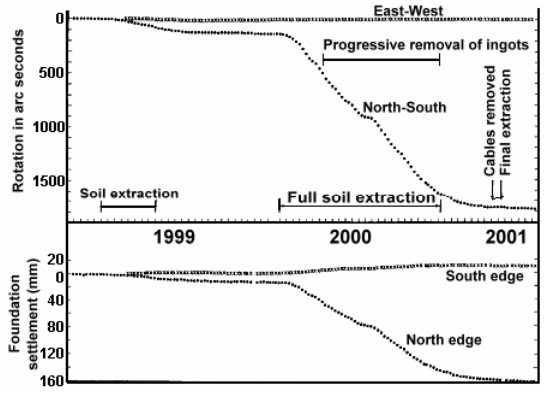

Figure 1.8. Results of both preliminary and full soil extraction

In addition to reducing the inclination of the Tower by half a degree, a limited amount of strengthening work has been carried out on the most highly stressed areas of masonry.

The technique of soil extraction has provided an ultra-soft method of increasing the stability of the Tower which at the same time is completely consistent with the requirements of architectural conservation. Its implementation has required advanced computer modelling, large-scale development trials, an exceptional level of continuous monitoring and day-by-day communication and control.

Most of the above arguement is developed almost identically in http://torre.duomo.pisa.it/ and http://www3.imperial.ac.uk/geotechnics/research/leaningtowerofpisa.

1.2 Venetian bell towers

Venezia skyline

In general, the analysis of historical buildings, such as ancient bell towers in Venice, herein presented, is often full of uncertainties. Unearthing information about traditional construction technologies becomes a useful instrument for deducing missing information about each specific case and for confirming results of surveys. Consequently the first part of this section is dedicated to a brief description of historical foundations in Venice.

Typology of historical foundations in Venice

The peculiar environmental conditions in which foundations of historical buildings had to be built in Venice produced a typical and recurrent structural form. Scarce availability of materials and low bearing capacity of the subsoil imposed severe constraints. The shallowest quaternary basin that supports most historic foundations in Venice is essentially characterized by up to 10 metres of recent lagoon deposits (Holocene), followed by soils of continental depositional environment (Würmian), up to 60m. The main feature of these deposits is the presence of a predominant silty fraction which characterizes both the upper soft (organic) silty clay, and the underlying fine sand, silty sand and clayey-silt. A shallow typically yellow over consolidated clay (locally named "Caranto") can be sometimes found in the city centre and covers a great part of the rest of the lagoon area [Simonini and Cola (2000)]. The fabric of most foundations remained substantially unchanged until the beginning of the last century. Two types predominate:

- shallow foundations, for low buildings, not bordered by canals.
- wooden piled foundations, for major buildings and usually for walls bordering canals.

Foundations of the first type are located between 1.5 m and 2.5 m depth. Their breadth may vary between 1.5 m and 2 m and, in some cases, they are bedded on a wooden platform. The foundations were made of bricks and mortar (masonry) or, more rarely, mixing stones and bricks. The use of the locally well-known Istrian limestone ("Pietra d'Istria") was aimed at preventing the capillary rise of saline water through the masonry walls. The successful use of direct foundations on such soft soil was due to the slow building process and to the existence of frequent sandy layers which speeded up the soil consolidation [Ricceri, Mazzucato and Soranzo (1992)].

The second type of foundation, rather time consuming and quite expensive, was characterized by short wooden piles ("compaction piles"), driven very close to each other, and was adopted for major structures, like, for example, bell towers. The length of the of piles rarely exceeded 3 m and the diameter varied from 15 cm to 25 cm. The purpose of this technique was to compact the soil and create an "artificial ground" [Zuccolo (1975)]. In this case the stone foundation very often rested on a wooden platform with the function of distributing loads on the underlying piles and creating a solid base for the stone blocks.

Bell tower foundations

Little information is available about foundations of bell towers in Venice, except for the cases in which the towers collapsed (San Marco), were demolished (Sant'Agnese, Figure 1.9), or important remedial measures were undertaken (Frari and Santo Stefano).

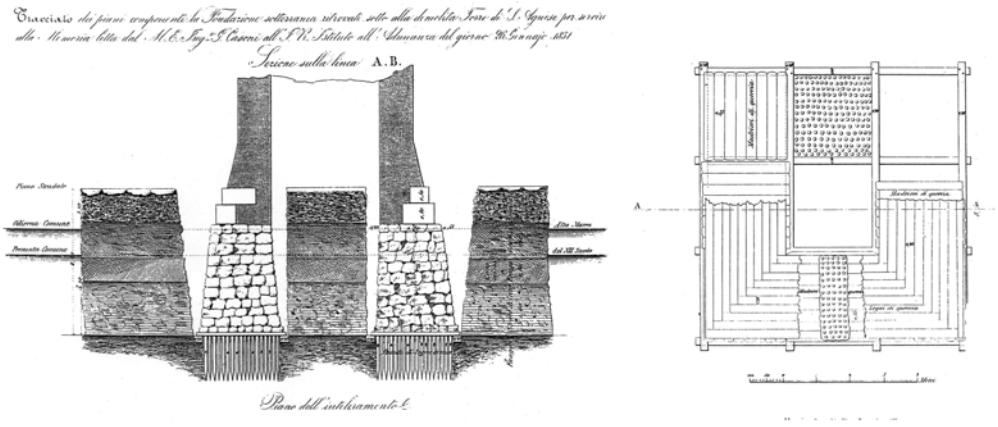

Figure 1.9. Section and plan view of the foundation of Sant'Agnese bell tower (from [Casoni (1851)]).

An interesting case-history was the Sant'Agnese bell tower, a record of which has been preserved thanks to a report written by the engineer, Giovanni Casoni, who carried out a detailed survey of the foundation (Figure 1.9) after the demolition of the tower: it represents a typical and very instructive example of bell tower foundations in Venice. Comparing case-histories [Casoni (1851)], a recurrent structure has been identified. The "compaction piles" were always found and very often the wooden boarding as well, detailed in Figure 1.9, for the Sant'-Agnese case. In general the Istrian limestone block appears to be hollow in the middle, probably not only for fulfilling strict economical criteria but also for better keeping dry large excavations in presence of a high ground water level.

1.2.1 Santo Stefano

History, characteristics and rotation of the Tower

Construction of the Santo Stefano bell tower (Figure 1.10) began in 1450. When it had reached a height of 27 m work stopped. The reason for this was a very evident rotation of the structure, which demonstrated that the foundation had been inadequate from the start of construction. Work recommenced nearly 100 years later, in about 1550. The vertical axis of the bell tower is not straight, because, in an attempt to correct the lean, the masonry walls were built vertically in the second stage of construction – this also occurred in the Pisa Tower.

The height of the building from its foundations to the belfry is c. 62 m and the foundation has an external width of 9 m.

Figure 1.10. Picture of the tower.

The first record of leaning, dated 1774, was measured as a horizontal displacement of 0.8 m (Figure 1.11) at the level of the belfry towards the east side, along which a little canal ("Ric Malatin") flows. Later on, in 1900, the rate of such movement was 7 mm per year, which led to a deviation from vertical up to 1.7 m, still measured at the level of the belfry. After the fall of the San Marco bell tower, in 1902, there was an animated local debate on the possible need to demolish the tower. The Municipality eventually decided to support the project of engineers Antonelli and Caselli and assigned them the direction of the work. The intervention, realized from the 1903 to the 1905, was characterized by the construction of five buttresses along the canal, resting on a rectangular shaped concrete bed (4 m x 10 m) founded on 3 m long concrete screw piles. During the works a sudden leaning increase of 0.15 m was recorded, but, at the end of the works the rate of movement slowed down to 1.5 mm per year (Figure 1.11). At present, a recently installed new monitoring system seems to show an even slower rate, but a longer observation period is required in order to draw any reliable conclusions.

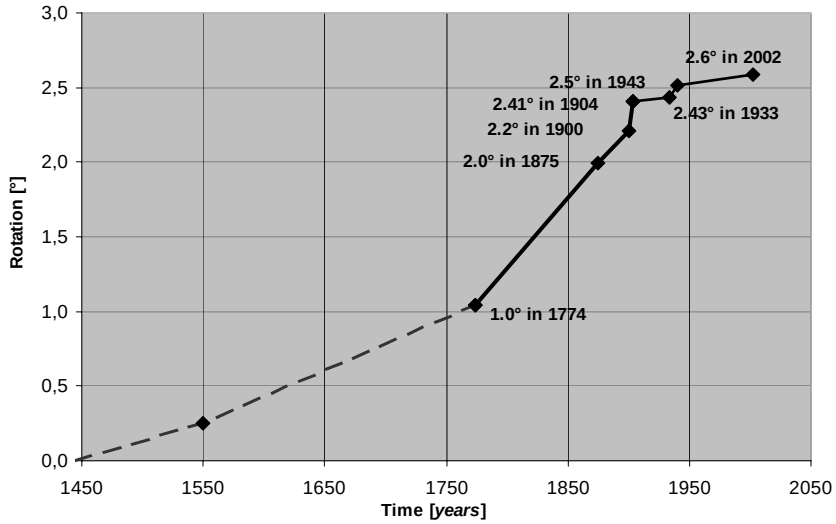

Figure 1.11. History of rotation of the Santo Stefano Bell Tower.

Geotechnical Investigations

During the 1904 works a large part of the foundation was excavated and described in a report, which became an important document for future interventions. A second extensive investigation started at the end of the 1980's. In particular, two geotechnical investigations were carried out in 1989 and 2004. The latter included 2 penetrometer tests with piezocone, 2 short boreholes, 1 dilatometer test, 2 inclined borings on the foundation, 1 inclined borehole and 1 vertical borehole with extraction of undisturbed soil samples for laboratory tests (Figure 1.12).

Stratigrafical and mechanical characterization of the subsoil was subsequently carried out. The ground profile underlying the tower (Figure 1.13) consists of three distinct soil units:

- between ground level and a depth of about 3.5 m: anthropic fill;
- between 3.5 m and about 7.6 m: normally consolidated and slightly overconsolidated silty clay with organic inclusions and shells (the foundation is located 4 m deep);
- between 7.6 m and 13 m depth: fine silty sand with layers of clayey-silt;

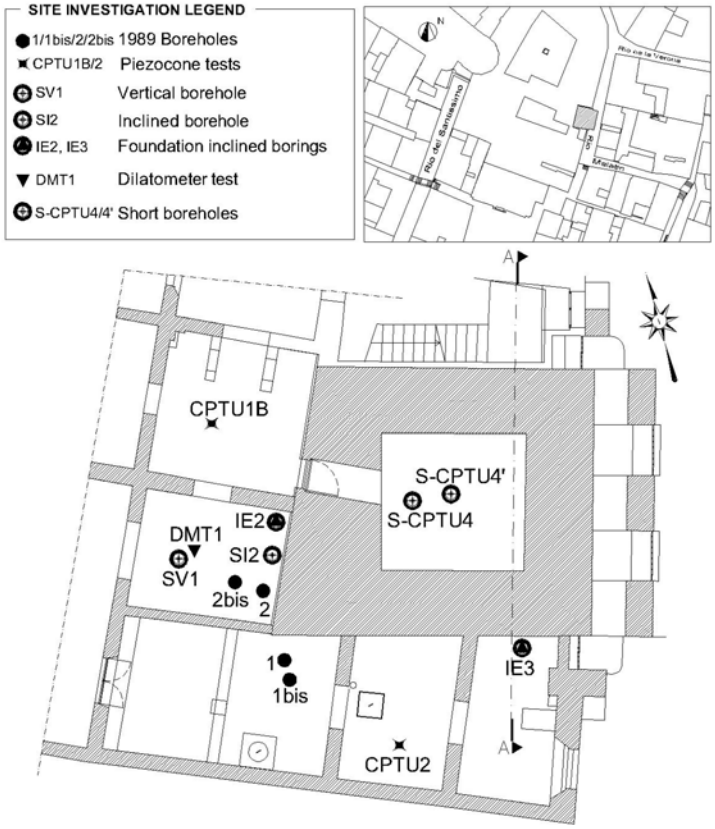

Figure 1.12. Plan of the geotechnical investigations.

- between 13 m and the maximum investigated depth: continuous alternating layers of silty clay, clayey silt and fine silty sand.

A strong non-symmetric element has always been the canal on the east side of the bell tower. The average ground water table is 1 m below local ground level.

The investigations carried out on the foundation, in addition to the 1903 report12, enabled the reconstruction of its geometry and the identification of the relevant materials. The foundation has a trapezoidal shape, both in section and in plan (Figure 1.13). Below the foundation block, mostly composed of Istrian limestone, the compaction piles (possibly in alder) have been driven at a spacing of about 30 cm and are 2.50 m long: consequently they stop in the silty-clay layer. Direct observations and related testing show a remarkable state of preservation of the wood. Unlike all others cases, here there is no wooden boarding between the stone block and the piles.

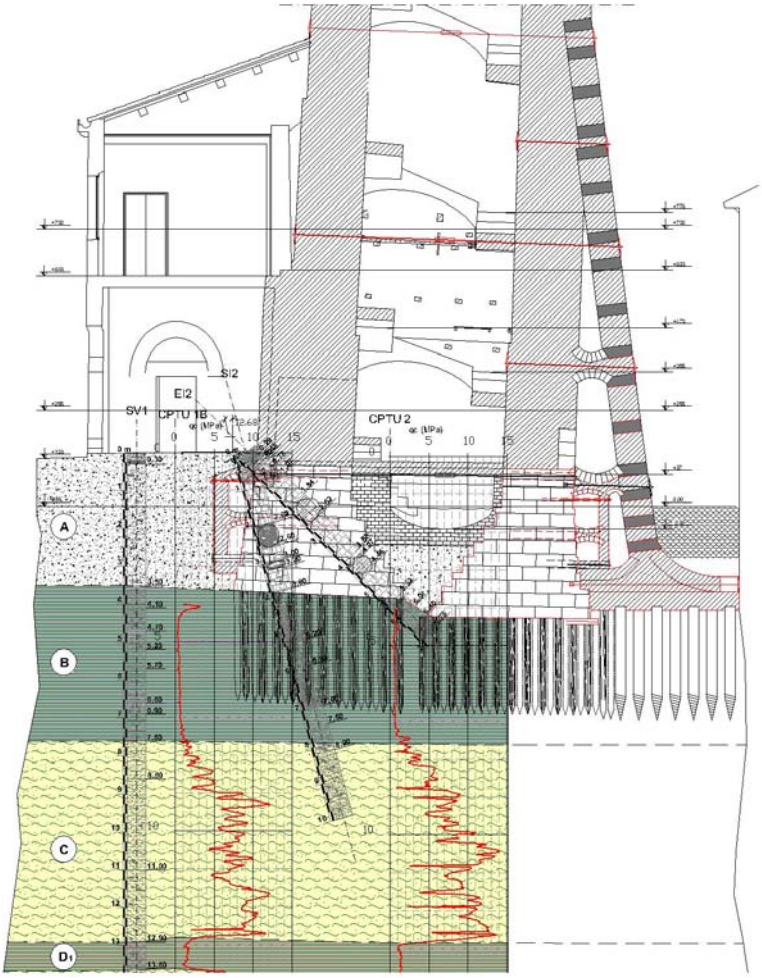

Figure 1.13. Schematic section of the tower foundation and of the relevant subsoil (AA in Figure 1.12).

CHAPTER **2**

Collapse mechanisms -*current* design tools-

Fragile Equilibrium, detail from “Le Domaine Enchante”. Renè Magritte.

“Ingenuity and lateral thinking are essential parts of engineering since it is often easier to find a way of avoiding a problem than to work out the real meaning of a problem and solve it"

E. C. Hambly, 1985

Introduction

—This chapter reviews literature relevant to the analysis of collapse mechanisms of towers. Two distinct mechanisms have been identified and analyzed for the foundations: (1) *bearing capacity* failure, due to lack of strength of the soil and (2) *instability* of equilibrium, due to lack of stiffness. A different aspect, which does not involve foundation and soil, is the stability of masonry walls [Heyman (1992)]. This material failure is not discuss in the thesis as it lies completely outside the geotechnical field. Nevertheless, ancient and old towers, in the presence of weak and disconnected masonry, can suffer sudden catastrophic failures, as attested by the collapse of the "San Marco bell tower", in Venice in 1902. The bearing capacity of foundations is discussed in the first section of this chapter, where, in addition to the classical bearing capacity review, there is also a description of incremental work hardening plasticity models for surface pads. Results coming from these models establish a link between the two simple collapse mechanisms. This is one of the key points of the work and will be study in depth in Chapters 3 and 4. The second section, in addition, includes a review of literature related to the buckling of the soil-structure interaction of tall structures. There are many examples of leaning towers around the world, probably one of the most famous being the leaning Tower of Pisa. For all these towers the bearing capacity problem is generally solved at the design stage. Initial imperfections or inadequate foundations can cause differential settlements which added to low stiffness of the soil can lead to the instability of the tower. Of course, progressive increases of tilting can also produce high compressive stresses in the masonry and consequent failures of the tower structure. All these problems are interrelated and one of the aims of this work is to give more cohesion to their treatment.

2.1 Bearing capacity failure - “foundation not *strong* enough"

This bearing capacity literature review is restricted to the analysis of shallow foundations, since most of the foundations of ancient towers can be modelled as shallow foundations, only a few metres deep.

Tower foundations are subjected to prevailing vertical self-weight loads, combined with moment loads due to their inclination, environmental wind and seismic forces impose additional horizontal and moment loads on the foundations, as well as altering the vertical load.

Traditional bearing capacity methods have been commonly used to calculate the ultimate capacity of towers footings under combined loading, with failure evaluated from inclined and eccentric load conditions. Recently a number of experimentally based studies have led to the development of an alternative to bearing capacity methods for foundations subjected to combined loads. These studies started with idea of interaction diagrams to replace bearing capacity factors that have then led to the development of full plasticity models which enable displacements to be predicted.

Most of the recent research in this direction has been driven by the off-shore industry and a number of improvements have been made. Even if combined loads acting on on-shore structures are not so severe as those acting off-shore (Comparison: Figure 2.1 and Figure 2.2), results of recent research is equally applicable to both cases.

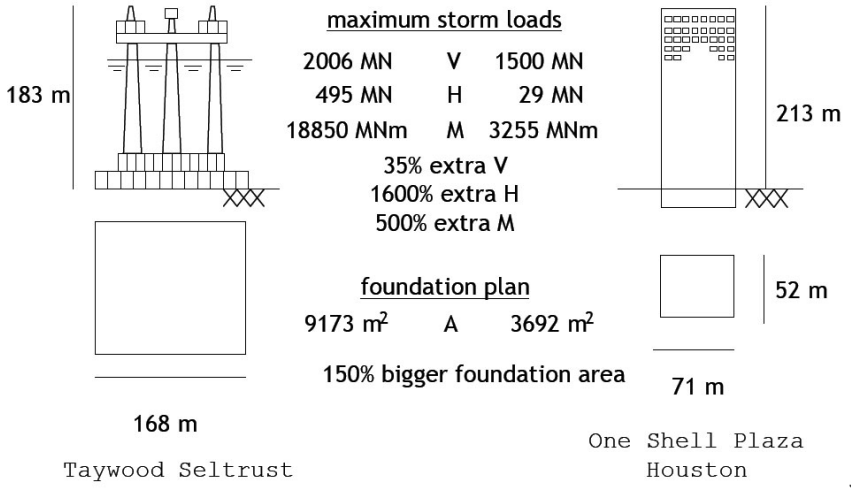

Figure 2.1. Comparison off-shore structure load condition with on shore [Gourvenec (2004)].

Figure 2.2. Permanent loads acting on Pisa Tower.

2.1.1 Traditional Bearing Capacity Theories

The most widespread formula used to estimate the bearing capacity of a surface footing was originally developed by Terzaghi [Terzaghi (1943)]. The formulation (Equation 2.1), was deduced from well-known limit equilibrium solutions. It refers to the ideal condition of strip footing (Figure 2.3) subjected to vertical central load, on homogeneous soil, with an horizontal base and ground surface. In addition the soil above the foundation level is supposed to have negligible shear strength and the contact between soil and foundation is rough.

$$q_{ult} = c\,N_c + q\,N_q + \frac{1}{2}\,B\,\gamma\,N_\gamma \tag{2.1}$$

c = operative cohesion of the soil;
γ = unit weight of the soil;
q = pressure of the overburden (γd);
d = footing depth;
B = width of the foundation;
N_c, N_q, N_γ = bearing capacity factors;

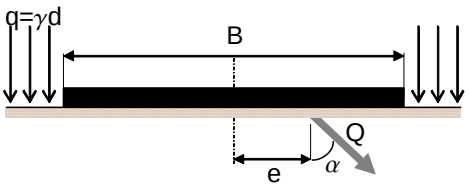

Figure 2.3. Scheme of a footing under an eccentric and inclined load

Since this formulation refers to an extremely simple case, not so common in practice, it was modified later to incorporate general conditions, such as inclination of the load, different shapes, inclination of the base and of the ground level. Brinch Hansen [Brinch-Hansen (1970)], proposed a number of correction factors to encompass all previous cases.

The final equation, which expanded the linear superposition assumption already made in equation 2.1, describes more general conditions:

$$q_{ult} = c\,N_c\,s_c\,d_c\,i_c\,b_c + q\,N_q\,s_q\,d_q\,i_q\,b_q + \frac{1}{2}\,B\,\gamma\,N_\gamma\,s_\gamma\,i_\gamma\,b_\gamma \qquad (2.2)$$

s_c, s_q, s_γ = shape factors;
d_c, d_q = depth factors;
i_c, i_q, i_γ = correction factors for the inclination of the load;
b_c, b_q, b_γ = correction factors for the inclination of the base of the foundation;
g_c, g_q, g_γ = correction factors for the inclination of the ground level;

Many different expressions for these factors have been obtained both analytically and experimentally ([Meyerhof (1963)], [Meyerhof (1953)]; [DeBeer (1970)]; Pracash and Hansen, 1971; Lebègue, 1972; Muhs and Weiss, 1973; Hanna and Meyerhof, 1981); Correction factor expressions are not detailed in this work, for a critical review refer to Gottardi's PhD Thesis [Gottardi (1992)].

For eccentric loading, Meyerhof [Meyerhof (1953)] suggested that for calculating bearing capacities an "effective area" concept should be used. The load carrying contact area, and thus the bearing capacity, is reduced such that the centroid of the effective area coincides with the applied vertical load. For a strip footing Meyerhof defined the effective width as B' = B - 2e, where e is the eccentricity of the applied load as depicted in Figure 2.3. Equation 2.2 is augmented as follows:

$$q_{ult} = c\,N_c\,s_c\,d_c\,i_c\,b_c + q\,N_q\,s_q\,d_q\,i_q\,b_q + \frac{1}{2}\,B'\,\gamma\,N_\gamma\,s_\gamma\,i_\gamma\,b_\gamma \qquad (2.3)$$

Since, in most cases, satisfactory estimations of load capacity can be achieved, this design procedure has become generally accepted. However, even in the case of a surface footing resting on granular material, the prediction provided by Equation 2.3 depends on many empirical coefficients which do not give the designer any indication of the validity of the prediction. Furthermore, all such expressions apply linear superposition to a problem that is highly non linear (Butterfield and Gottardi, 1993). All these considerations prompted researchers in the eighties to develop a more reliable approach, as described in following sections.

2.1.2 Alternative Yield Surface Loci

Butterfield (1978), Figure 2.4, suggested overcoming the traditional approach by introducing interaction diagrams for the bearing capacity of surface pads subjected to general load conditions; a concept already familiar to structural engineers.

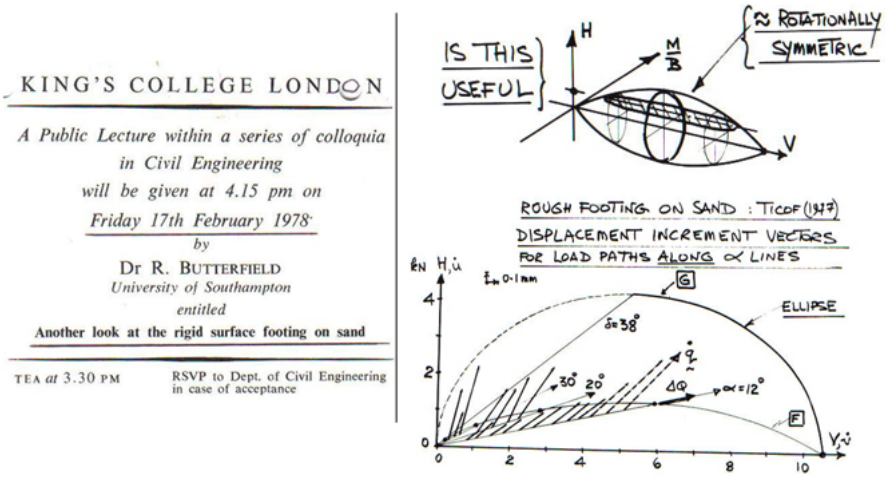

Figure 2.4. Lecture at King's College London - Butterfield, 1978

The interaction diagrams are curves which relate the different loading components at failure, defining a region inside which all allowable load combinations must lie.

These alternative failure envelopes, defined in the V:M:H plane, was described by Butterfield and Ticof (1979), for strip footings on sand, as a parabolic yield surface along the V axis, and elliptical in the direction perpendicular to it (similar to the 3D-surface drawn in Figure 2.4), which they called a "cigar-shaped". The surface was based solely on the interpretation of a large number of load controlled tests, not relying on any empirical bearing capacity formula. Butterfield and Ticof recommended that the size of the yield surface be determined by fixed dimensionless peak loads:

$$\frac{M}{BV_0} \approx 0.1 \text{ and } \frac{H}{V_0} \approx 0.12$$

where V_0 is the maximum vertical load experienced. Peak values of H and $\frac{M}{B}$ occur when :

$$\frac{V}{V_0} = 0.5$$

Recent interest in this area has let to more systematic work direct towards establishing the necessary components of plasticity models. The shape of the interaction diagrams has been intensively investigated through a large number of tests: Nova and Montrasio (1991) reported tests on strip footings on loose sand. Gottardi (1992) studied strip footing on dense sand. Dean et al. (1993), describe tests on conical and spudcan footings on sand, performed at Cambridge University. Martin (1994) investigated circular footings (model spudcans) on clay, using test ring with displacement control tests. Gottardi [Gottardi, Houlsby and Butterfield (1999)] confirms previous results and remark that a similarly shaped envelope applies to foundations of differing geometries on such very different soils. Butterfield and Gottardi (1993) describe the shape of the failure envelope in (V, M/2R, H) plane as a parabolic ellipsoid with elliptical cross-section. The ellipse is centred on the origin, and the principal axes are slightly rotated anticlockwise from the coordinate axes (Figure 2.5).

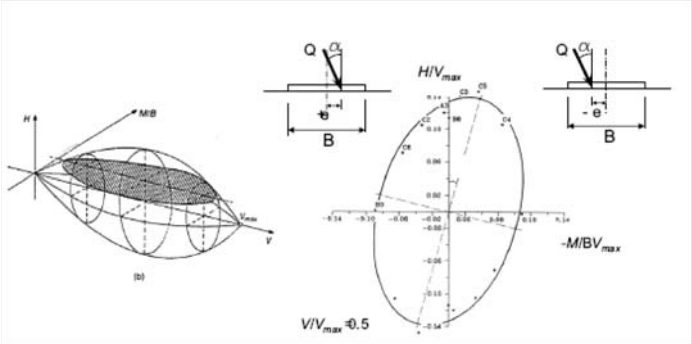

Figure 2.5. Three dimensional interaction diagrams and sections with a plane at constant V/Vmax = 0.5 (after Butterfield and Gottardi, 1993).

It is interesting to observe also that traditional correction factors can be combined to define a locus of limiting behavior in V:M:H space, i.e. vertical, eccentric and inclined loading. If the maximum vertical load is defined as the vertical bearing capacity:

$$V_{\max} = q_{\text{ult}} A$$

Where A is footing area and, since the moment load M = Ve, the failure interaction surfaces can be derived and compared. Using Brinch-Hansen [Brinch-Hansen (1970)], the correction factor is:

$$i_\gamma = \left(1 - 0,7 \frac{H}{V}\right)^5 \tag{2.4}$$

In the $(\frac{V}{V_{\max}}, \frac{H}{V_{\max}})$ plane a failure locus can be defined and expressed by the following equation:

$$\frac{H}{V_{\max}} = \frac{10}{7} \frac{V}{V_{\max}} \left[\left(1 - \frac{V}{V_{\max}}\right)^{\frac{1}{5}}\right] \tag{2.5}$$

The same can be done in the other planes but with different formulations: Figure 2.6 shows the results obtained for Mayerhof and Brinch-Hansen (Cassidy, 1999; where $V_{peak} = V_{max}$).

There are a number of evident advantages in adopting this approach, one is that it is a direct method, which unables us to deal with deviatoric load components (M and H) in a unique way, even so, the interpretation of traditional correction factors described in Figure 2.6 underlines that there is some continuity between it and the classical approach. In addition, interaction diagrams enable us to evaluate overall margin of safety in a systematic way. Another fundamental and consistant aspect is that such interaction diagrams provided a framework for developing complete models for the analysis of surface pads; these are described in detail in Section 2.1.3.

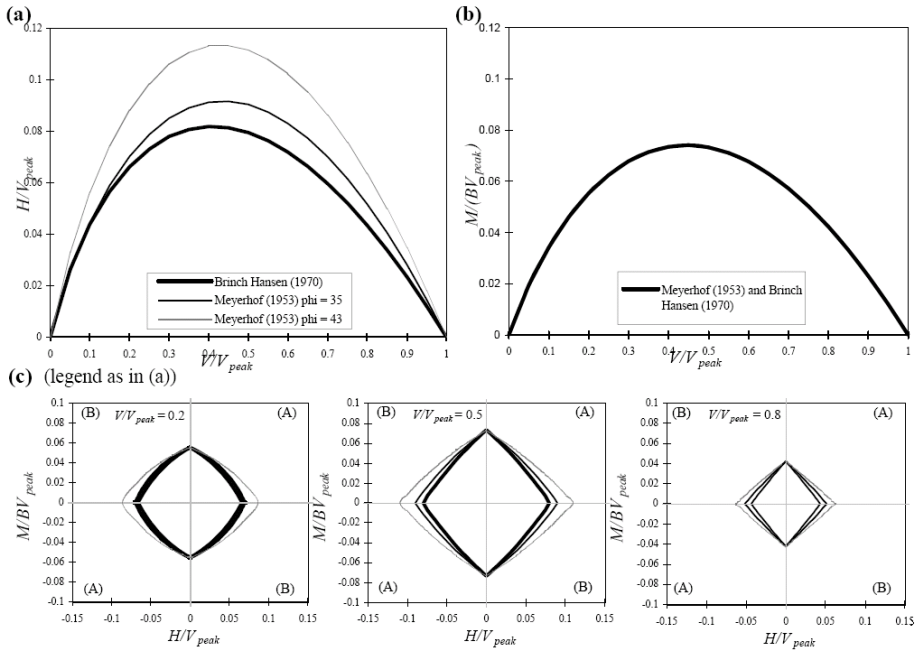

Figure 2.6. Bearing capacity interaction surfaces derived from Meyerhof (1953) and Brinch Hansen (1970). Cassidy, 1999.

2.1.3 Use of Plasticity Theory for Combined Loading of Foundations

The design of shallow foundations deals with two main problems: the evaluation of bearing capacity and the prediction of displacements which frequently control the final dimensions of the footing. Traditionally the ultimate bering capacity and the prediction of displacement have been investigated as distinct problems. Estimation of bearing capacity is usually based on Brinch-Hansen's formula (1970), essentially a limit equilibrium solution (Section 2.1.1), whereas predictions of displacements are even less well-founded and refer either to linear-elastic solutions such as those provided in Milovic et al. (1970) or Poulos and Davis (1974), even though soils responds non-linearly and irreversibly to applied loads. These approaches are still handicapped by the lack of reliable models, in particular when loads are inclined and eccentric.

In last thirty years the spread of numerical analyses and the growing off-shore industry gave a strong motivation to develop plasticity-based analysis, constructed in terms of the force resultants acting on the footings and the corresponding footing displacements.

Such an approach seems to have been first suggested by Roscoe & Schofield (1956) and later on developed indipendently by Butterfield (1980, 1981). Recently there have been major contributions to the development of the experimental work necessary to support this approach (e.g. Schotmann, 1989; Nova & Montrasio, 1991, 1997; Gottardi, 1992; Gottardi & Butterfield, 1993, 1995; Houlsby & Martin, 1992; Martin, 1994; Gottardi & Houlsby, 1995; [Gottardi, Houlsby and Butterfield (1999)]). Complete theoretical models, all expressed in terms of work-hardening plasticity theory, have been developed for specific tests. These models make use of the force resultants and the corresponding displacements of the footing, and enable predictions of responce to be made for any applied load or displacement combination.

Complete strain hardening models developed to date are:

• The model by Nova and Montrasio (1991) for the behavior strip footing on loose sand;

• The "Model B" by Martin (1994), presented by Martin and Houlsby (2001) for the behavior of spudcan on speswhite kaolin clay;

• The "Model C" by Cassidy (1999) and [Gottardi, Houlsby and Butterfield (1999)] and presented by Houlsby and Cassidy (2001) for the behavior of rigid circular footing on sand extended for loose carbonate (Cassidy et. al., 2002) sand and for 6 d.o.f. on silica sand (Bienen et al., 2006);

Their general common outline and specific details of them are described in following sections.

Outline of the models

Each of the models starts from the concept that at any penetration of a foundation into the soil, a yield surface in (V, M, H) space will be established. Load paths which move within this surface will produce only elastic deformation in *elastic-plastic* models, or will not produce any displacement in *rigid-plastic* models, whereas load points that touch the surface can also produce plastic deformation. *Hardening* is supposed to be *isotropic* and *kinematic*, consequently the shape of this surface is assumed constant, whilst its size and position may change. The expansion of the yield surface, when the footing is pushed further into the soil, is taken as a function of the plastic component of deformations, which is why these models are called *strain-hardening* plasticity models. The hardening parameter are the plastic displacements. All models agree that the ratio between the plastic strains is governed by an associated flow rule in the (M/B-H) plane, and by a non associated flow rule in (V-M/B) and (V-H) planes.

To sum up, the main ingredients of the model are:

• Yield surfaces: a family of curves, established from an experimental database;

• A set of plastic potentials: which define a non associated flow rule in (V-M/B) and (V-H) planes and an associated flow rule in the (M/B-H) plane;

• A hardening law: an empirically formulated relationship which links vertical yield load (V_0) to the plastic displacement;

And, if the behavior within the surface is supposed to be elastic (Dean et. al., 1997; Cassidy 1999):

• a set of elastic moduli.

Details of the models

The main features of all existing complete models can be described in a schematic way as follows.

- *Nova and Montrasio (1991)*

Nova and Montrasio (1991) were the first to present a rigorous mathematical model aimed at the prediction of settlements of a strip footing resting granular material. It is a rigid-plastic strain-hardening model with a non-associated flow rule, expressed as:

$$d\boldsymbol{q} = \boldsymbol{C}\, d\boldsymbol{Q} \tag{2.6}$$

Where $\boldsymbol{C}$ is the compliance matrix.

The vector $\mathbf{Q}$ of the generalized non-dimensional stress variables, and the vector $\mathbf{q}$ of generalized strain variables are defined as:

$$\boldsymbol{Q} \equiv \begin{pmatrix} \zeta \\ h \\ m \end{pmatrix} \equiv \frac{1}{V_M} \begin{pmatrix} V \\ H/\mu \\ M/(\psi \mathrm{B}) \end{pmatrix}; \quad \boldsymbol{q} \equiv \begin{pmatrix} \eta \\ \varepsilon \\ \zeta \end{pmatrix} \equiv V_M \begin{pmatrix} v \\ \mu \mathrm{u} \\ \psi \mathrm{B} \theta \end{pmatrix} \tag{2.7}$$

Where:

V_M : Maximum value of the vertical central load at failure (≡*V*max)

ψ : non-dimensional constitutive parameter, ψ=0.33.

μ: parameter that gives the slope of the tangent of the failure locus at the origin (analogous to the traditional soil-foundation friction coefficient), μ = tan δ (=0.48).

Equations which comprise the model are detailed in Table 2.1.

Table 2.1. *Nova and Montrasio (1991)*

	Equations	*Parameters*
Elastic behaviour†	-	-
Yield function	$f(\mathbf{Q}, \rho_c)=h^2+m^2-\left[\zeta^2\left(1-\frac{\zeta}{\rho_c}\right)\right]^{2\beta}=0$	β=0.95, μ=0.48, ψ=0.33
Hardening law	$\rho_c(\lvert\mathbf{q}\rvert)=1-\exp\{-\frac{R_0}{V_M^2}\left[\eta^2+\left(\frac{\alpha\lvert\varepsilon\rvert}{\mu}\right)^2+\left(\frac{\gamma\lvert\zeta\rvert}{\psi}\right)^2\right]^{1/2}\}$	R_0 , α, γ
Plastic potential	$g(\mathbf{Q})=\left(\frac{\mu}{\mu_g}\right)^2 h^2+\left(\frac{\psi}{\psi_g}\right)^2 m^2-\left[\zeta^2\left(1-\frac{\zeta}{\rho_g}\right)\right]^{2\beta}=0$	μ_g , ψ_g, ρ_g

† This model is rigid in unloading

The value and meaning of parameters are the following: β controls the position of the maximum horizontal load and produces a vertical tangent to the yield locus at $V=V_M$; μ gives the slope of the tangent of the failure locus at the origin and resembles the traditional soil-foundation friction coefficient; R_0 is the slope of the initial tangent to the vertical central load curve; ψ, α and γ are non dimensional constitutive parameters; ψ_g, and μ_g, are non dimensional constitutive parameters which can be determined experimentally; ρ_g is a scaling factor.

Further developments have recently been added to the model to incorporate cyclic loading (Nova and Di Prisco, 2003).

- *MODEL B (Martin 1994; Martin and Houlsby, 2001)*

MODEL B was developed to predict the load-displacement response of a spudcan foundation on clay and mostly is based mostly on results from an extensive experimental campaign on spudcan footings bearing on speswhite kaolin clay.

The model is described in terms of work-hardening plasticity theory with three degrees of freedom (vertical, rotational, horizontal). The *yield surface* is experimentally derived; the 3-dimensional surfaces are cigar-shaped and similar to that proposed by Ticof (1979).

The *hardening law* defines the vertical bearing capacity as a function of plastic spudcan penetration, and is based on a set of theoretical lower bound bearing capacity factors for embedded conical footings.

The *flow rule* is experimentally derived (behavior inside the yield surface was found to be elastic) and is defined by a set of elastic stiffness factors for embedded conical footings, determined from three-dimensional finite element analysis accounting for elastic cross-coupling effect between the rotational and horizontal degrees of freedom. The flow was found to be approximately associated in the (M, H) plane from laboratory tests results reported by Martin and Houlsby (2000) but since the vertical displacements, δw_p, were found to be consistently

smaller than those predicted by an associated flow rule an empirical association parameter ζ was assumed.

Equations of this model are not listed in order to leave more space for details of the more recent *MODEL C.*

- *MODEL C (Cassidy, 1999; Houlsby and Cassidy, 2002)*

MODEL C was developed by (Cassidy, 1999) and Houlsby and Cassidy (2002) to predict the load-displacement response of a rigid circular footing on sand and mostly based on results from a small scale testing programme ([Gottardi (1992)]; [Gottardi and Houlsby (1995)]; [Gottardi, Houlsby and Butterfield (1999)]). The model follows the development of *MODEL B.* The proposed equations are listed in Table 2.2. The model is expressed in terms of dimensionless variables:

$h = \frac{H}{V_0}$, $m = \frac{M}{2RV_0}$, $v = \frac{V}{V_0}$; where V_0 defines the size of the yield surface.

Table 2.2. The MODEL C (Cassidy, 1999; Houlsby and Cassidy, 2002)

	Equations	*Parameters*
Elastic behaviour	$\begin{pmatrix} \mathrm{dV} \\ \mathrm{dM}/2R \\ \mathrm{dH} \end{pmatrix} = 2\mathrm{RG} \begin{pmatrix} k_v & 0 & 0 \\ 0 & k_m & k_c \\ 0 & k_c & k_h \end{pmatrix} \begin{pmatrix} \mathrm{dw}_e \\ 2\,\mathrm{Rd}\theta_e \\ \mathrm{du}_e \end{pmatrix}$	R, G, k_v, k_m, k_c, k_h
Yield function	$f = \left(\frac{h}{h_0}\right)^2 + \left(\frac{m}{m_0}\right)^2 - 2a\,\frac{h}{h_0}\,\frac{m}{m_0} - \beta_{12}(v)^{2\beta_1}(1-v)^{2\beta_2} = 0$ $\beta_{12} = \left(\frac{(\beta_1+\beta_2)^{\beta_1+\beta_2}}{(\beta_1)^{\beta_1}(\beta_2)^{\beta_2}}\right)^2$	β_1, β_2, h_0, m_0, a
Hardening law	$\mathrm{V}_0 = \frac{\mathrm{kw}_p + \left(\frac{f_p}{1-f_p}\right)\left(\frac{w_p}{w_{\mathrm{pm}}}\right)^2 V_{0m}}{1 + \left(\frac{\mathrm{kw}_{\mathrm{pm}}}{V_{0m}} - 2\right)\left(\frac{w_p}{w_{\mathrm{pm}}}\right) + \left(\frac{1}{1-f_p}\right)\left(\frac{w_p}{w_{\mathrm{pm}}}\right)^2}$	f_p, V_{0m}, w_{pm}, k
Plastic potential‡	$g = \left(\frac{h'}{h_0}\right)^2 + \left(\frac{m'}{m_0}\right)^2 - 2a\,\frac{h'}{h_0}\,\frac{m'}{m_0} - \alpha_v^2\,\beta_{34}(v')^{2\beta_3}(1-v')^{2\beta_4} = 0$ $\beta_{34} = \left(\frac{(\beta_3+\beta_4)^{\beta_3+\beta_4}}{(\beta_3)^{\beta_3}(\beta_4)^{\beta_4}}\right)^2$	β_3, β_4, α_v, h_0, m_0, a

‡ α_v is an association factor: associated flow is given by $\alpha_v = 1$

The *yield surface* has the form of a parabolic ellipsoid (Butterfirld, 1981), with elliptical sections on planes at constant V. The shape is governed by 3 parameters:

- a which defines the rotation of the surface about the uniaxial load axis $\frac{V}{V_0}$.

- m_0 and h_0 which determine the ratios of $\frac{H}{V}$ and $\frac{M}{2RV}$ at the widest section of the surface, which occurs at $\frac{V}{V_0} = 0{,}5$ if parameters β_1 and β_2 are equal to 1.

Parameters β_1 and β_2 are introduced to allow for the control of the location of the maximum size of the elliptic section, from $\frac{V}{V_0} = 0{,}5$ to $\frac{V}{V_0} = \frac{\beta_2}{(\beta_1+\beta_2)}$. In addition, by choosing $\beta_1 < 1$ and $\beta_2 < 1$ the singularity points on the surface at V=0 and V=V_0 can be avoided.

The size of the surface is defined by the maximum V value: V_0, which is the intercept between the yield surface and the V-axis at V≠0.

The *hardening law* is described by an empirical equation based on the experimental load-displacement curve. The main assumption underpinning the choice of the hardening rule is that the hardening is solely governed by the vertical plastic displacement, w_p, and $V_0 = f(w_p)$. The suggested hardening law (Table 2.2), capable of fitting post-peak behavior, is quite complicated, but, the precise form of this equation is not central to the model, and a simpler one which fits observed data may be adopted.

Behavior inside the yield surface was found to be *elastic* and is defined by a set of elastic stiffness factors.

The *flow rule* is experimentally derived: the flow was found to be approximately associated in plane ($\frac{M}{2RV}$, $\frac{H}{V}$) but not in the deviatoric planes. A convenient expression for the plastic potential (Table 2.2), very similar to that used for the yield surface, was adopted.

Work in progress

Interest in the development and application of models based on the interaction diagrams is quite widespread and recently analyses are being extended in different directions:

- introduction of the hypoplasticity for the formulation of new models capable of reproducing the results of cyclic loadings (Di Prisco et al., 2003);
- 6 degree of freedom model (Bienen et al., 2006);
- embedment effects due either to the initial burial depth of the foundation (*d*) or to the footing penetration (*w*) (Govoni, 2007);

2.2 Buckling - “foundation not *stiff* enough"

Structural instability, of which the buckling of a column is the best known example, is usually associated with slender flexible structures of stiff materials, such as steel or reinforced concrete. To illustrate buckling consider a column under an axial compressive load, if the column is sufficiently slender it fails due to deflection to the side rather than crushing of the material. This phenomenon is the simplest prototype of structural stability problem that was historically the first to be solved (Timoshenko, 1953). Many authors have shown that structural instability can occur, also, in foundation engineering and soil mechanics, when stiffness of the soil is low and, consequently, deformations are large. Hambly in 1985 described soil-structure interaction instability of tall, or top-heavy, structures on compressible foundations, the punch-through failure of off-shore jack-up platforms, and the premature failure of soil samples in different testing machines. It should be noted that this instability is not due to lack of strength of the ground but to the insufficient stiffness, i.e. excessive settlement under load. Since all foundations are compressible to some extent, such instability can occur in a column on a stiff stratum if the column is very tall. In the following sections some classical stability concepts are recalled (Section 2.1, Section 2.2 and Section 2.3) and applied in the soil-structure interaction field (Section 2.4). The analysis is, then, centred on the specific topic of towers, analysed as rigid bodies, resting on compressible ground.

2.2.1 An Outline: elastic and inelastic theories

A structure can fail either due to material failure or to instability. If structure become unstable (in the sense described above) long before the strength and stiffness criteria are violated, than the material can be treated as elastic. It could also happen that a structure fails due to a combination of both, material failure and instability. Indeed material failure is normally preceded by inelastic phenomena, which generally have a destabilizing influence on structures. Inelastic behavior comprises not only plasticity (or elastoplasticity), but also creep (viscoelastic as well viscoplastic). Linear elastic bifurcation buckling of structural members is the most elementary form of instability, and its study is an essential step towards understanding the buckling behavior of complex structures, including structures incorporating inelastic behavior, initial imperfections, etc.

The stability of *elastic* structures is a classical problem first solved by Leonhard Euler [1707–1783], who used the theory of calculus of variations to obtain the equilibrium equation and buckling load of a compressed elastic column. This work was published in the appendix “De curvis elasticis” of his book titled Methodus inveniendi lineas curvas maximi minimive proprietate gaudentes, Lausanne and Geneva, 1744.

Joseph-Louis Lagrange [1736– 1813] developed the energy approach that is more general than Newton’s vector approach for the study of mechanics problems.

This led naturally to the fundamental energy theorem of minimum total potential energy being sufficient for stability. Jules Henry Poincar´e [1854–1912] is known as the founder of bifurcation theory and the classification of singularities.

On the other hand, Aleksandr Mikhailovich Liapunov [1857–1918] gave the basic definitions of stability and introduced the generalized energy functions that bear his name, Liapunov functions. Furthermore, Lev Semenovich Pontryagin [1908–1988] introduced, with A. A. Andronov, the important topological concept of structural stability.

This work has led to the well known classification theory presented in a treatise, Stabilite structurelle et morphogenese: Essai d'une theorie generale des modeles (Structural Stability and Morphogenesis: An Outline of General Theory of Models) by R. Thom.

Theodore von K´arm´an [1881–1963] began the work on *inelastic* buckling of columns. He devised a model to explain hysteresis loops and conducted research on plastic deformation of beams. Warner Tjardus Koiter [1914–1997] initiated the classical nonlinear bifurcation theory in his dissertation, "Over de Stabiliteit van het Elastisch Evenwicht", at Delft. Budiansky and his colleagues (1946, 1948) gave a modern account of the nonlinear branching of continuous elastic structures under conservative loads.

Furthermore, Hutchinson (1973a, b) made an important contribution to the nonlinear branching theory of structures loaded in the plastic range. Pioneering research on inelastic buckling of columns by A. Considere, F. Engesser and F. R. Shanley is also significant for this thesis.

2.2.2 Elastic Theories

Definition of stability

A general definition of stability has to be given in a dynamic sense. The one used in all fields, engineering, economics, biology, etc., is due to Liapunow (1982) and can be simply stated as follows: *a structure (or any system) is stable if a small change in the initial conditions (input) leads to a small change in the solution (output responce)*.

Since the instability of equilibrium is a *dynamic* process (failure in general is a dynamic process), obviously the most realistic way to approach buckling and stability is the dynamic point of view. However, *dynamic stability analysis* is essential for structures subjected to *nonconservative* loads, such as wind or pulsating forces, while in many other cases equivalent results for stability can be achieved by *static* analysis or *energy* methods, which are generally much simpler ([Bazant and Cedolin (1991)]).

In the *static* approach, Newton's second law is used to obtain the governing equations, whereas in the *energy* approach the total energy (which is the sum of internal energy and potential energy due to the loads) is minimized to obtain the governing equations. They correspond to the different strategies used in satisfying the state of equilibrium for the deformed member (*second-order theory*) and applicable under specific hypothesis described in following sections.

The governing equations are in the form of an eigenvalue problem in which the eigenvalue represents the buckling load and eigenvector the buckling mode. The smallest buckling load is termed the *critical buckling load*. Note that the critical buckling load is associated with the state of neutral equilibrium, i.e., characterized by the stationarity condition of the load with respect to the displacement.

In order to ascertain whether the equilibrium position is stable or unstable, we use the perturbation technique (*si rimuove l'ipotesi di piccoli spostsamenti*) for the static approach or by examining the second derivative of the total potential energy in the energy method. In one dimension, q_1, the condition of stability is illustrated in Figure 2.7.

Static and energy analysis are better explained in the following sections, and applied to a simple case of a rigid-bar column with linear elastic rotational spring, relevant for the topic of the thesis. In this peculiar case the fact that the system is *discrete* (1 degree of freedom) simplify the solution. An example of *continuous* system is given by the Euler column, which has, in this case a pure historical meaning.

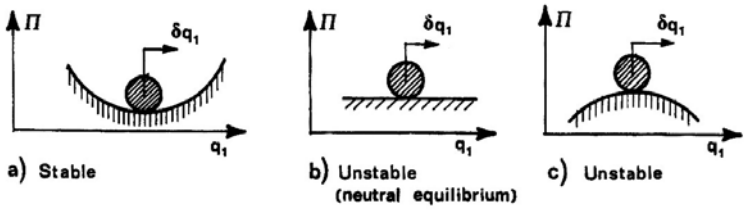

Figure 2.7. Ball in a gravity field with single degree of freedom: different conditions of stability of equilibrium position. ([BazantBook] page 209)

Static analysis

Static analysis can be applied to well known "*Eulerian problems*", these problems involve conservative systems with pre-critical linear elastic behavior.

Perfect rigid-bar column with linear elastic rotational spring - small deflections

An example of Eulerian problem is the simple case of a perfect rigid-bar column of length *l* with linear elastic rotational spring of stiffness *k* (Figure 2.8).

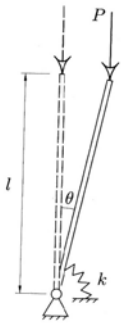

Figure 2.8. Perfect rigid-bar column with linear elastic rotational spring. ([Ferretti et al. (2002)] page 16)

The column is loaded by axial load *P*, considered positive when it causes compression. We assume the column to be perfect, which means that it is perfectly straight before the load is applied, and the load is perfectly centric. In the vertical position the column is obviously in equilibrium for any load P. For large enough load, however, the equilibrium is unstable, that is, it cannot last. We now seek conditions under which the column can deflect and still remain in equilibrium. If the load keeps constant direction during deflection, as is true of gravity loads, the equilibrium condition in the deformed configuration requires that:

$$M_{stab} = M_{dest} \Rightarrow Pl\sin\theta = k\theta \tag{2.8}$$

Assuming that the rotation is small we may use the linearized approximation

$$\sin\theta \simeq \theta \tag{2.9}$$

From which the equilibrium equation become

$$Pl\theta = k\theta \Rightarrow \theta(Pl - k) = 0 \tag{2.10}$$

The previous equation allows a nonzero rotation (at P>0) if and only if

$$P_{cr} = \frac{k}{l} \tag{2.11}$$

The eigenvalue P_{cr}, called *critical load*, denotes the value of load P for which a nonzero rotation of the perfect column is possible. This value represents the failure load only for perfect column with elastic support. As we shall see later, *for real columns that are imperfect, the critical load is a load at which rotations become very large*. At critical load, the vertical stand of the column, which always represents an equilibrium state for any load, has adjacent equilibrium states, the deflected configurations, and the column is in neutral equilibrium. This means that it behaves the same way as a ball lying on a horizontal plane (Figure 2.7b). In reality, of course, the deflection cannot become arbitrarily large because we initially assumed small deflection. When finite deflections of the column are solved, it is found that the branch of the P-θ diagram emanating from the critical load point is curved upward and has a horizontal tangent at the critical load.

Euler column - small deflections

The Swiss mathematician Leonhard Euler was the first to obtain, in 1744, the critical load formula for a pin-ended elastic column (Figure 2.9) subjected to an axial load *P*.

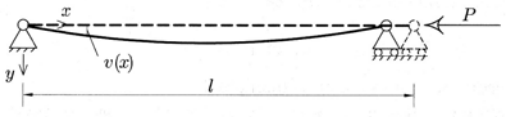

Figure 2.9. Euler column ([Ferretti et al. (2002)] page 21)

The equilibrium equation for the deflected column is

$$M_{stab} = P\,v(x),\ M_{dest} = -EIv''(x) \Rightarrow EIv''(x) + P\,v(x) = 0 \tag{2.12}$$

The *eigenvalues* of the previous ordinary differential equation, which can be solved applying the boundary condition, are

$$P_n = n^2\,\pi^2\,\frac{EI}{l^2},\ (n = 1, 2, \ \ldots\ \ldots, \infty) \tag{2.13}$$

The deflection shapes at critical loads, representing the eigenmodes, are given by

$$v_n(x) = c_n \sin\frac{n\pi x}{l} \tag{2.14}$$

With c_n arbitrary constants.

The critical design load, in this case, is the lowest eigenvalue, called *Euler load*

$$P_E = EI\,\frac{\pi^2}{l^2} \tag{2.15}$$

Dividing the Euler load by the cross-section of the beam we obtain the critical stress

$$\sigma_E = \frac{\pi^2}{(l/r)^2}\,E,\ r = \sqrt{I/A}\ :\ \text{radius of inertia} \tag{2.16}$$

The ratio l/r is called the *slenderness* ratio and represents the basic nondimensional parameter for the buckling behaviour of columns. The plot in Figure 2.10 a horizontal line plus *Euler's hyperbola,* represent, for a perfect column (continuous line), the transition from material failure

to structural instability when slenderness changes. For real columns, due to inelastic effects and imperfections the plot exhibits a gradual transition (sketched line).

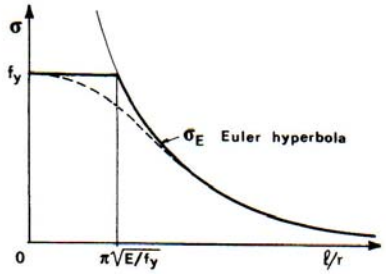

Figure 2.10. Buckling stress as a function of slenderness ([BazantBook] page 8)

Imperfect rigid-bar column with linear elastic rotational spring - small deflections

The perfect column we have studied so far is an idealized model. In reality, several kinds of inevitable imperfections must be considered. For example, columns may be initially rotated rather than perfectly vertical; or the axial load may be slightly eccentric. As we will demonstrate, columns are quite sensitive to imperfections, indeed, even if they are extremely small, they still cause failure since they produce very large destructive deflections when the critical load is approached. We further discuss the case of a rigid-bar column with a linear elastic rotational spring, subjected to eccentric load P (Figure 2.11).

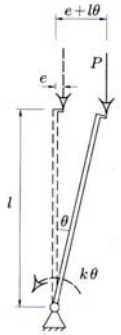

Figure 2.11. Imperfect rigid-bar column with linear elastic rotational spring. ([Ferretti et al. (2002)] page 29)

Applying static analysis the equilibrium between external and internal moment is

$$M_{stab} = M_{dest} \Rightarrow P(l \cdot sin\theta + e \cdot cos\theta) = k\theta \tag{2.17}$$

Assuming that the rotation is small we may use the linearized approximation

$$P(l\theta + e) = k\theta \Rightarrow P = \frac{k}{l} \frac{\theta}{\theta + \frac{e}{l}} \tag{2.18}$$

The previous equation describe the path of equilibrated conditions, plotted in Figure 2.12 (dashed line).

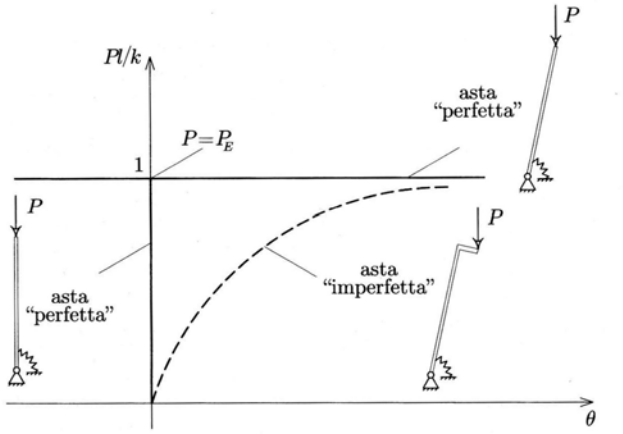

Figure 2.12. P-θ diagram for the perferfect (continuous line) and imperfect (sketched line) rigid column ([Ferretti et al. (2002)] page 29)

If we plot curves changing the value of the initial imperfection, we see that as the initial imperfection tends to zero the load-deflection curve asymptotically approaches that of a perfect column with the bifurcation point at critical load. In addition the deflection tends to infinity at $P \rightarrow P_{cr}$, no matter how small the initial imperfection is, infact

$$\lim_{\theta \to \infty} \frac{k\theta}{l\theta + e} = \frac{k}{l} \tag{2.19}$$

Another type of imperfection is the initial rotation θ_0. This case may be treated as a special case of initial eccentricity, indeed, if θ is the rotation from the vertical configuration, the equilibrium equation is

$$M_{stab} = M_{dest} \Rightarrow Pl\sin\theta = k(\theta - \theta_0) \tag{2.20}$$

Assuming that the rotation is small we may use the linearized approximation

$$Pl\theta = k(\theta - \theta_0) \Rightarrow P = \frac{k(\theta - \theta_0)}{l\theta} \tag{2.21}$$

Which shows the same asymptotic behavior as Equation 2.19, since

$$\lim_{\theta \to \infty} \frac{k(\theta - \theta_0)}{l\theta} = \frac{k}{l}$$

While the undeformed condition correspond to $\theta=\theta_0$, at which P=0.

However, it should not be concluded that the imperfection analysis always yields the same maximum load as the bifurcation analysis (critical state). Note also that if loads are large, the column material will fail before the critical load is reached. These notes are, of course, limited to the *small-deflection theory.* If a non-linear, *finite-deflection theory* is used the deflection does not approach infinity at $P \rightarrow P_{cr}$. Rather it simply become large, and from a practical viewpoint, usually unacceptably large.

Every column has an initial imperfection which is difficult to measure, but unavoidable imperfections must be taken into account in evaluating the results of buckling tests. The *Southwell plot* is a method which allows to determine the critical load independently of initial imperfections. For details see [Bazant and Cedolin (1991)], pages 24-26.

Large deflections

All considerations so far have been limited to the linearized, small-deflection theory (second-order theory), which applies for infinitely small deformations or rotations. This is sufficient for many practical purposes in structural engineering; nevertheless, a full understanding of the column behavior calls for a nonlinear finite-deflection theory. Although the initial nonlinear behavior is more easily determined by an approximate energy approach, an exact equilibrium solution is possible for some columns, as we will demonstrate for the rigid bar in Figure 2.9 and Figure 2.11. In both cases we remove the hypothesis of small deflection and the relation between load and rotation become, respectively:

$$P = \frac{k}{l}\frac{\theta}{sin\theta} \qquad \textit{for the perfect column} \tag{2.22}$$

And

$$P = \frac{k}{l}\frac{\theta}{sin\theta + \frac{e}{l}cos\theta} \qquad \textit{for the imperfect column} \tag{2.23}$$

The diagram of load versus rotation for perfect and imperfect columns, according to Equation 2.22 and Equation 2.23 is plotted in Figure 2.13.

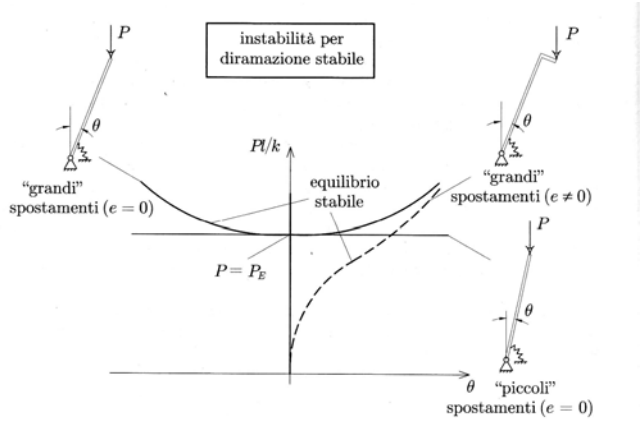

Figure 2.13. P-θ diagram for small and large deflections for the perferfect (continuous line) and imperfect (sketched line) rigid column ([Ferretti et al. (2002)] page 32)

Our analysis leads to several important observations:

- In contrast to the linearized small-deflection theory, the deflection does not tend to infinity at P_{cr} but remain bounded at any load.
- After the critical state, the load increases as the deflection increases. Thus column possess a postcritical reserve. This contrasts with buckling of some other structures for which the load decreases after the critical state.
- The deviations from the linearized small-deflection theory do not become significant until the deflections become quite large.

The generalization of the solution of initial postcritical behavior to imperfect columns is discuss in the energetic framework.

Energy methods

Static analysis represents a part of energy approach, however a part that cannot answer the question of stability. Statics, infact, can only yield equilibrium states, which may be stable or unstable. In addition the energy method can be consider as "a bridge" between static and dynamic features of the stability problem [Ferretti et al. (2002)].

According to the Lagrange-Dirichlet theorem, stability of conservative structural systems can be determined by energy methods.

> Lagrange-Dirichlet Theorem – Assuming the total energy to be continuous, the equilibrium of a system containing only conservative and dissipative forces is stable if the potential energy of the system has a strict minimum (*i.e.* positive definite)

Potential energy for discrete elastic system

The potential energy Π consist of the (elastic) strain energy U, and the work of loads W. According to the principle of conservation of energy, if we consider that an equilibrium state of the structure is changed to another, adjacent equilibrium state in response to a change in the given loads, then we must have:

ΔU=ΔW, or ΔU-ΔW=0

It follows that if the loads are not changed, then the net change of energy of the structure load system is ΔU-ΔW. Therefore, the potential energy is defined as

$$\Pi = U - W \tag{2.24}$$

Where we write Π, U, W instead of ΔΠ, ΔU, ΔW, because Π, U, W is considered to be zero in the initial state.

For the case of constant loads we have:

$$W = \Sigma_k P_k q_k \tag{2.25}$$

Where P_k : load associated with q_k (k = 1, 2, ..., n),
generalized displacements (kinematic variables) and n, degrees of freedom of the discrete system.

For variable loads, $W = \Sigma_k \int P_k(q_k)\, d\, q_k$.

The fact that positive definiteness of ΔΠ guarantees stability can also be proven (independently from Lagrange-Dirichlet theorem) on the basis of the second law of thermodynamics. If the change of state is isothermal, ΔΠ represents the Helmholtz free energy of the structure-load system.

The loading may in general be considered to change as a function of some control parameter λ, which may represent the load (λ=P).

Let $\delta q_{1,....}$, δq_n be a small variation of the generalized displacements from the equilibrium state assumed to occur at constant λ. Assuming Π a smooth function (i. e., continuous and with continuous derivatives up to a sufficient order), function Π may be expanded into a Taylor series about the equilibrium state; this provides

$$\Delta\Pi = \Pi(q_1 + \delta q_1,\ ....,\ q_n + \delta q_n;\ \lambda) - \Pi(q_1,\ ....,\ q_n;\ \lambda) = \delta\Pi + \delta\Pi^2 + \delta\Pi^3 + ... \tag{2.26}$$

In which

$$\delta\Pi = \frac{1}{1!} \sum_{i=1}^{n} \frac{\partial \Pi(q_1,\ ....,\ q_n;\ \lambda)}{\partial q_i}\, \delta q_i$$

$$\delta\Pi^2 = \frac{1}{2!}\sum_{i=1}^{n}\sum_{j=1}^{n}\frac{\partial^2\,\Pi(q_1,\ ....,\ q_n;\ \lambda)}{\partial q_i\,\partial q_j}\,\delta q_i\,\delta q_j$$

$$\delta\Pi^3 = \frac{1}{3!}\sum_{i=1}^{n}\sum_{j=1}^{n}\sum_{k=1}^{n}\frac{\partial^3\,\Pi(q_1,\ ....,\ q_n;\ \lambda)}{\partial q_i\,\partial q_j\,\partial q_k}\,\delta q_i\,\delta q_j\,\delta q_k$$

$\delta\Pi,\ \delta\Pi^2,\ \delta\Pi^3,$ are called the first, the second and the third variation of the potential energy.

The *condition of equilibrium* are

$$\boxed{\delta\Pi = 0,\ \text{for any}\ \delta q_i} \tag{2.27}$$

According to the Lagrange-Dirichlet theorem, the *equilibrium state is stable* for those values of the control parameter λ for which

$$\boxed{\delta\Pi^2 > 0,\ \text{for any}\ \delta q_i,\ \delta q_j} \tag{2.28}$$

When, for some λ value, $\delta\Pi^2 = 0,$ for some $\delta q_i\,,\ \delta q_j$ but not for some other, or $\delta\Pi^2 = 0$ identically for all, the analysis must be carried on following Liapunov's stability theorem (for details see [Bazant and Cedolin (1991)], Section 3.6 and 4.2).

Overturning instability of a block

The preceding stability conditions apply only if function $\Pi(q_1,\ ....,\ q_n)$ is continuous and has continuous derivatives. This is true for most elastic structures, but not for systems of bodies in contact that can separate (lose contact). For example consider stability of a rigid block (a retaining wall or a building) of weight P that rests on a rigid base and is loaded by a constant horizontal force H (e. g., dead load exerted by earth pressure or water pressure) applied at height *a* as shown in Figure 2.14. We assume that the block cannot slip; but it can lift from the base and thus it can lose stability by overturning. The work done on the block during overturning is W=Mq where M=Ha-Pb and q=dq=small rotation about the corner O. So the potential energy for the block is

$$\Pi = \begin{cases} -Mq = (Pb - Ha)\,q & \text{for } q \geqslant 0 \\ \infty & \text{for } q < 0 \end{cases}$$

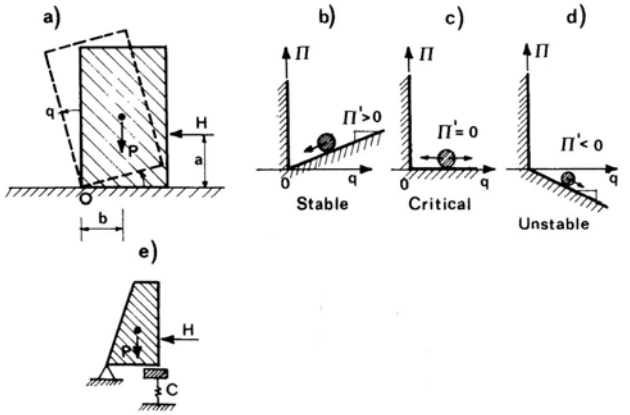

Figure 2.14. (a-d) Stability of a rigid block; (e) rigid block on elestic base. ([BazantBook] page 214)

According to the Lagrange-Dirichlet theorem the block is stable if $\Pi>0$ for any possible $\delta q \neq 0$. This means that the block is stable if $(Pb - Ha)>0$, critical if $(Pb - Ha)=0$, and unstable if $(Pb - Ha)<0$. The system behaves the same way as a ball rolling on the potential surfaces shown in Figure 2.14 b, c and d.

Conceptually it is interesting to note that (1) equilibrium exists without $\delta\Pi=0$; (2) the condition of stability is $\delta\Pi>0$ for dq>0, but not $\delta^2\Pi>0$; and (3) Π, Π', and $\delta^2\Pi$ are discontinuous at q=0, and the derivatives Π' and $\delta^2\Pi$ are one-sided, defined only for $q \longrightarrow 0^+$.

Perfect rigid-bar column with linear elastic rotational spring - small deflections

Consider now the simple example of the rigid bar in Figure 2.8. The angle θ may be taken as generalized displacement, and if for $\theta=0$ the spring is free of stress, $\theta=0$ is an equilibrium position, which we want to investigate for stability. If $\Pi=0$ for the position $\theta=0$, then the potential energy in the deformed configuration is

$$\Pi = \frac{1}{2} k\theta^2 - P\eta = \frac{1}{2} k\theta^2 - Pl(1 - \cos\theta) \tag{2.29}$$

With η vertical displacement of the load. Expanding in a Taylor series:

$$\eta = l(1 - \cos\theta) = l\left(\frac{1}{2}\theta^2 - \frac{1}{24}\theta^4 + ...\right)$$

Than, neglecting terms with order greater than second, we have the following equilibrium condition

$\delta\Pi = 0 \rightarrow (k - Pl)\,\theta\delta\theta = 0$ for any $\delta\theta$, which gives

- $\theta=0$ - equilibrium position $\forall$ P
- $P_{cr}=\frac{k}{l}$ - critical load

The condition of stability is

$$\delta\Pi^2 > 0 \rightarrow (k - Pl)\,\delta\theta^2 > 0 \tag{2.30}$$

- if $P < \frac{k}{l}$ than $\theta=0$ is a stable equilibrium position,
- if $P \geqslant \frac{k}{l}$ than $\theta=0$ is a unstable.

Imperfect rigid-bar column with linear elastic rotational spring - small deflections

With reference to Figure 2.11, the potential energy for the deformed system can be write as

$$\Pi = \frac{1}{2} k\theta^2 - P\eta = \frac{1}{2} k\theta^2 - Pl(1-\cos\theta) - Pe\cdot\sin\theta \tag{2.31}$$

$$\eta = l(1-\cos\theta) - e\cdot\sin\theta = l\left(\frac{1}{2}\theta^2 - \frac{1}{24}\theta^4 + ...\right) - e\left(\theta - \frac{1}{6}\theta^3 + ...\right)$$

$\delta\Pi = 0 \rightarrow [(k - Pl)\theta - Pe]\,\delta\theta = 0$ for any $\delta\theta$, which gives

- $P_{cr} = \frac{k}{l}\,\frac{\theta}{\theta + \frac{e}{l}}$ - critical load

The condition of stability is

$$\delta\Pi^2 > 0 \rightarrow (k - Pl)\,\delta\theta^2 > 0 \tag{2.32}$$

It should be noted that under the simplification of small deflection (i. e. simplified linearized formulation), the stable regions of the perfect and imperfect systems are the same because the second variations $\delta\Pi^2$ for both systems are given by identical expressions. In reality, of course, the deflection cannot become arbitrarily large because we initially assumed small deflections and the stable regions of the imperfect and perfect systems then need not be the same. When deflection are large the nonlinear, finite-deflection theory must be applied.

Large-deflection postcritical behavior and types of bifurcation

Postcritical behavior deals with the study of stability of equilibrium states of the structure after the first critical state is passed. The existence of diverse type of postcritical behavior leads to an important classification of conservative stability problems. Buckling may be classified into two categories: (1) *bifurcations* and (2) *limit load buckling*.

In *bifurcation* buckling, the deflection under compressive load changes from one direction to a different direction. The load at which the bifurcation occurs in the load-deflection space is the critical buckling load. The deflection path that exists prior to bifurcation is known as the primary path, and the deflection path after bifurcation is called the secondary or postbuckling path. Depending on the structure and loading, the secondary path may be symmetric or asymmetric, and it may rise or fall below the critical buckling load. The previous aspects will be detailed in the following examples, since bifurcation buckling is not only relevant for the topic of this thesis, but also the most elementary form of buckling, and its study is an essential step towards understanding the buckling behavior of complex structures, including structures incorporating initial imperfections, inelastic behavior,etc.

For completeness it must be define also the second type of buckling. In *limit load buckling*, the structure attains a maximum load without any previous bifurcation, i.e., with only a single mode of deflection. The snap-through (observed in shallow arches and spherical caps) and finite-disturbance buckling (only unique to shells) are examples of limit load buckling.

Some examples will be use to define different types of bifurcation buckling.

- **Symmetric Stable Bifurcation**

Consider the column shown in Figure 2.15a. Let q=inclination angle of the bar, and α=initia small inclination (for α=0 the column is perfect).

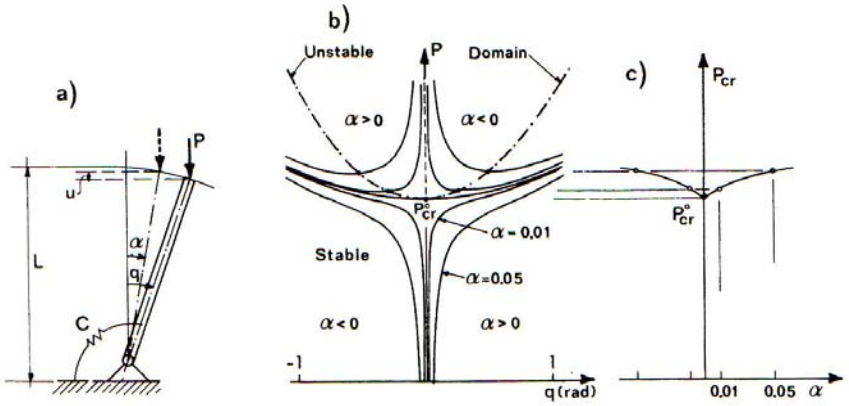

Figure 2.15. (a) Rigid bar column with rotational spring at base, (b) equilibrium path, (c) imperfection sensitivity diagram. ([BazantBook] page 239)

The potential energy is

$$\Pi = U - W = \frac{1}{2} C(q-\alpha)^2 - PL(\cos\alpha - \cos q) \tag{2.33}$$

Its derivatives are

$$\frac{\partial \Pi}{\partial q} = C(q-\alpha) - PL\cdot\sin q \qquad \frac{\partial^2 \Pi}{\partial q^2} = C - PL\cdot\cos q \tag{2.34}$$

Setting $\frac{\partial \Pi}{\partial q} = 0$, we have the equilibrium condition

$$P = \frac{C}{L}\left(\frac{q-\alpha}{\sin q}\right) \tag{2.35}$$

The equilibrium diagrams P(θ) are plotted (as the solid and dashed curves) in Figure 2.25b fo various values of the initial imperfection, α.

Setting $\frac{\partial^2 \Pi}{\partial^2 q} = 0$, we find that the critical state lie on the curve (dash-dot curve in Figure 2.25b):

$$P_{cr} = \frac{C}{L\cdot\cos q} \tag{2.36}$$

Examine now stability of the equilibrium states. Substituting the equilibrium value of P (Equation 2.35) into Equation 2.34, we get

$$\frac{\partial^2 \Pi}{\partial q^2} = C[1 - (q-\alpha)\cdot cotg\, q] \tag{2.37}$$

The column is stable if $\frac{\partial^2 \Pi}{\partial^2 q} > 0$. So the stability condition is tan q > q-α if α < q < $\frac{\pi}{2}$ and tan q < q-α if -$\frac{\pi}{2}$ < q < -α.

This may be related to the slope of the equilibrium diagram, which is given by

$$\frac{\partial P}{\partial q} = \frac{C}{L}\left(\frac{1}{\sin q}\right)[1 - (q-\alpha)\cot q] \tag{2.38}$$

Consider now that $\alpha > 0$. The equilibrium curves are then the curve families at bottom right and top left in Figure 2.15b. From Equation 2.38 we conclude that, for q > α, the equilibriu curves for $\alpha > 0$ in Figure 2.15b are stable when their slope is positive, while for q < 0 they are stable when their slope is negative. The point at zero slope on each curve represents the critical state (Equation 2.36). According to Equation 2.37 the value of q at the critical state is related to by the trascendental equation q - tan $q = \alpha$. Note that this column can be stable for load higher than the critical load P_{cr}^0 of the perfect column. Also, critical states exist for P > P_{cr}^0 even if the system is imperfect (see the dash-dot curve connecting the critical states in Figure 2.15b). Repeating the same derivation for $\alpha < 0$ one gets symmetrical results (the curve families at bottom left and top right in Figure 2.15b). It may be concluded that for q > 0 stability is always associated with positive slopes, and for q < 0 with negative ones.

Although, for this column, the critical states other than the one for the perfect structure cannot be reached under load control, it is interesting to determine the dependence of the critical load on the initial imperfection α (Figure 2.15c). The diagram for this dependence is generally called the *imperfection sensitivity diagram.* According to the condition $\frac{\partial^2 \Pi}{\partial^2 q} = 0$ and Equation 2.37, the critical states are characterized by q - tan $q = \alpha$. For small values of q (and α), we have tan $q \simeq q + \frac{1}{3} q^3$, cos $q \simeq 1 - \frac{1}{2} q^2$, and substituting these expressions into Equation 2.36 we obtain

$$P_{cr} = \frac{C}{L}\left[1 + \frac{3^{2/3}}{2}\alpha^{2/3}\right] \qquad \text{(for small } \alpha\text{)}$$

The perfect column has a point of bifurcation at P = P_{cr}^0, and for P > P_{cr}^0 it follows a rising postbuckling path. Therefor this type of bifurcation is called *stable,* It is also *symmetric,* because the postbuckling path is symmetric with q. The critical state for the perfect column is in this case stable since for P = $\frac{C}{L} = P_{cr}^0$ and α=0 we have $\Pi = C(\frac{1}{2} q^2 - 1 + cosq) \simeq \frac{q^4}{4!} C$>0. That illustrate that stability at the critical state is decided by fourth-order terms in the expansion of Π.

To obtain the behaviour near the bifurcation point, the potential energy in Equation 2.33 may be approximated by a polynomial. It is interesting to note that it does not suffice to substitute in Equation 2.33 cos $q \simeq 1 - \frac{1}{2} q^2$, cos $\alpha \simeq 1 - \frac{1}{2} \alpha^2$; one could check that this simplification yields only the critical load $P_{cr}^0 = \frac{C}{L}$, of the perfect system but nothing about the approximation of Π, that is, set cos $q \simeq 1 - \frac{1}{2} q^2 + \frac{1}{24} q^4$, cos $\alpha \simeq 1 - \frac{1}{2} \alpha^2 + \frac{1}{24} \alpha^4$ in Equation 2.33, and then

$$\Pi = \frac{1}{2} C(q - \alpha)^2 + \frac{1}{24} PL(q^4 - 12 q^2 - \alpha^4 + 12 \alpha^2)$$

One may now follow the same procedure as before to obtain the asymptotic approximations for equilibrium paths P(q, α) and critical states $P_{cr}(\alpha)$. A salient property of the stable symmetric bifurcation is that the polynomial expansion of Π contains no cubic term and has a positive quadratic term.

- **Symmetric Unstable Bifurcation**

The fact that the critical states of the imperfect column occur at loads higher than P_{cr}^0 for the perfect system has not a general validity. Consider now a slightly different column (Figure 2.16) in which the rotational spring at the base is replaced by a horizontal, vertically sliding spring of stiffness C.

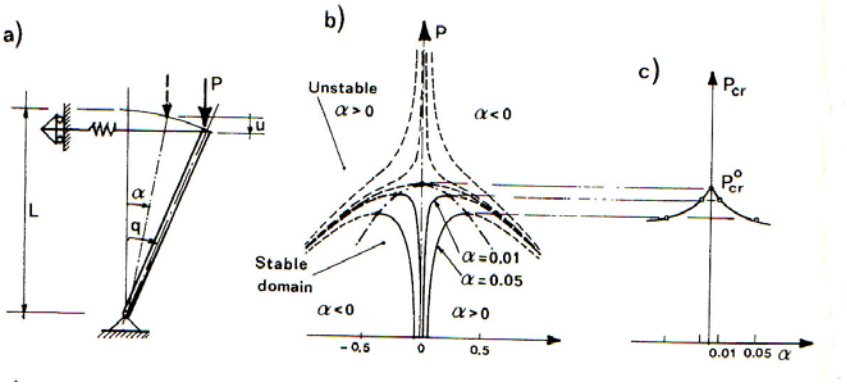

Figure 2.16. (a) Rigid-bar column with horizontal spring at top, (b) equilibrium path, (c) imperfection sensitivity diagram. ([BazantBook] page 242)

Unlike before, the resisting moment of the spring force about the hinge at the base is not proportional to the rotation at the base, because the force harm of the spring decreases as the column deflects. In this case:

$$\Pi = \frac{1}{2} CL^2(\sin\alpha - \sin q)^2 - PL(\cos\alpha - \cos q)$$

$$\frac{\partial \Pi}{\partial q} = CL^2(\sin q - \sin\alpha)\cos q - PL \cdot \sin q$$

$$\frac{\partial^2 \Pi}{\partial q^2} = CL^2(\cos 2q + \sin\alpha \sin q) - PL \cdot \cos q \qquad (2.39)$$

The equilibrium condition

$$\frac{\partial \Pi}{\partial q} = 0 \rightarrow P = \mathrm{CL}\left(1 - \frac{\sin\alpha}{\sin q}\right)\cos q \qquad (2.40)$$

defines equilibrium diagrams P(θ) for various value of the initial imperfection α, plotted in Figure 2.16.

The curve which defines the critical states (dashed-dot curve in Figure 2.16) is

$$\frac{\partial^2 \Pi}{\partial^2 q} = 0 \rightarrow P_{\mathrm{cr}} = \mathrm{CL}\,\frac{\cos(2q) + \sin\alpha \sin q}{\cos q}$$

The critical load for the perfect column (α=0) is

$$P^0_{\mathrm{cr}} = \lim_{q \to 0} P_{\mathrm{cr}}(\alpha = 0) = \lim_{q \to 0} P(\alpha = 0) = \mathrm{CL}$$

For the analysis of stability of the equilibrium state substitute Equation 2.40 in 2.40

$$\frac{\partial^2 \Pi}{\partial^2 q} = \frac{\mathrm{CL}^2}{\sin q}(\sin\alpha - \sin^3 q) \qquad (2.41)$$

Note that the condition of positiveness of this expression is identical (for $0 \leqslant q \leqslant 90°$) to the condition $\frac{\partial P}{\partial q} > 0$. Thus, as is generally true, the rising portion of the equilibrium curves in Figure 2.16 are stable, the declining portions are unstable, and the critical states occur at the limit points, that is the points with a horizontal tangent. From Equation 2.41, the critical states are characterized by the condition $\sin q_{\mathrm{cr}} = (\sin\alpha)^{\frac{1}{3}}$.

The critical states of the imperfect system occur at load less than the critical load of the perfect one. The larger the imperfection is the lower is the critical load. For such systems, it's important to quantify the dependence of the critical load P_{cr} of the imperfect system on the magnitude of the imperfection. Substituting: $\sin q = \sin q_{cr} = (\sin \alpha)^{\frac{1}{3}}$ and $\cos q = \cos q_{cr} = [1-(\sin \alpha)^{\frac{2}{3}}]^{\frac{1}{2}}$ into equation 2.41, for sufficiently small α we obtain

$$P_{cr} \simeq CL\left(1 - \frac{3}{2}\alpha^{\frac{2}{3}}\right)$$

Note that the critical load decrease is proportional to the $\frac{2}{3}$ power of the imperfection, a behaviour typical of many systems. Therefore, the tangent of the imperfection sensitivity diagram $P_{cr}(\alpha)$ (Figure 2.16c) has a vertical downward slope at α=0. This means that the critica load decreases very rapidly with only a very small imperfection.

Structures for which the critical load decreases at increasing imperfection are called *imperfection sensitive,* while those with the opposite behavior are called *imperfection insensitive.* It could be demonstrate that the imperfection sensitivity diagram $P_{cr}(\alpha)$ always begin with a vertical downward slope. If the drop of P_{cr} is large for typical imperfection values in practise, the structure is said to be *strongly imperfection sensitive.* For columns, the drop of P_{cr} due to actual imperfections is usually quite small, even though the imperfection sensitivity diagram may be starting with a vertical tangent.

The equilibrium curve emanating from the bifurcation decreases with displacement symmetrically and for this reason the bifurcation is termed *unstable symmetric.* Unlike the previous example, the bifurcation state itself is unstable.

To determine only the behavior near the bifurcation, Π can be approximated by a polynomial. As before we must take into account terms of higher order than the quadratic

$$\Pi = \frac{CL^2}{2}\left[\left(q - \frac{q^3}{6}\right) - \left(\alpha - \frac{\alpha^3}{6}\right)\right]^2 - PL\left[\left(1 - \frac{\alpha^2}{2} + \frac{\alpha^4}{24}\right) - \left(1 - \frac{q^2}{2} + \frac{q^4}{24}\right)\right] \simeq$$

$$\frac{CL^2}{6}[3(q-\alpha^2) + \alpha q(\alpha^2 + q^2) - \alpha^4 - q^4] + \frac{PL}{24}(q^4 - 12q^2 - \alpha^4 + 12\alpha^2)$$

Asymptotically, this is the same type of behavior as is obtained by the preceding procedure. For obtaining unstable symmetric bifurcation, it is essential that the cubic term (q^3) vanishes when α=0, and than the quadratic term (q^4) is negative near the critical load.

- **Asymmetric Bifurcation**

In the preceding examples the equilibrium curves were symmetric with regard to the undeflected equilibrium state at which bifurcation take place. This do not happens in the following example, in which a rigid bar (Figure 2.17) supported by a hinge is held upright by a laterally sliding spring of stiffness C and constant inclination angle 45°.

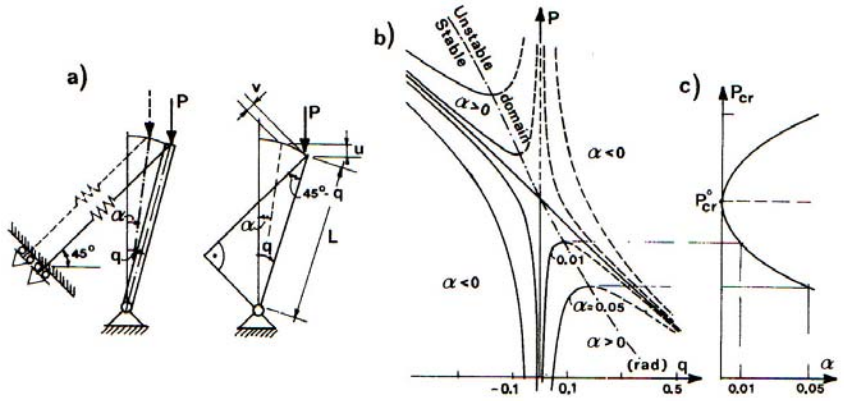

Figure 2.17. (a) Rigid-bar column with inclined spring, (b) equilibrium path, (c) imperfection sensitivity diagram. ([BazantBook] page 245)

The column is generally imperfect, with initial inclination α. The extension of the spring is v = L cos (45° - q)-L cos (45° - α), and so the potential energy expression and his derivatives are:

$$\Pi = \frac{1}{2} CL^2[\cos(45° - q) - \cos(45° - \alpha)]^2 - PL(\cos\alpha - \cos q)$$

$$\frac{\partial \Pi}{\partial q} = CL^2\left[\frac{1}{2}\cos 2q - \sin(45° - q)\cos(45° - \alpha)\right] - PL \cdot \sin q$$

$$\frac{\partial^2 \Pi}{\partial q^2} = CL^2[\cos(45° - \alpha)\cos(45° - q) - \sin 2q] - PL \cdot \cos q$$

The equilibrium condition defines equilibrium diagrams Figure 2.17

$$\frac{\partial \Pi}{\partial q} = 0 \rightarrow P = \frac{CL}{\sin q}\left[\frac{1}{2}\cos 2q - \sin(45° - q)\cos(45° - \alpha)\right] \tag{2.42}$$

The curve which defines the critical states (dashed-dot curve in Figure 2.17) is

$$\frac{\partial^2 \Pi}{\partial^2 q} = 0 \rightarrow P_{cr} = CL\left[\frac{\cos(45° - \alpha)\cos(45° - q)}{\cos q} - 2\sin q\right]$$

The critical load for the perfect column (α=0) is

$$P_{cr}^0 = \lim_{q \to 0} P_{cr}(\alpha = 0) = \lim_{q \to 0} P(\alpha = 0) = \frac{CL}{2}$$

Stability is characterized by the condition

$$\frac{\partial^2 \Pi}{\partial^2 q} = CL^2[\cos(45° - q)\cos(45° - \alpha) - \sin 2q] - PL\cos q > 0$$

And substituting here for P (Equation 2.42) we can check the sigh of $\frac{\partial^2 \Pi}{\partial^2 q}$ for positive q. This is equivalent to check the condition $\frac{\partial P}{\partial q} > 0$.

Thus, as is generally true, the rising portion of the equilibrium curves in Figure 2.17 are stable, the declining portions are unstable, and the critical states occur at the limit points, that is the points with a horizontal tangent.

Note that an initial inclination of the column to the right causes a decrease in the critical load, while to the left it causes an increase in the critical load. This type of behavior is celled asymmetric bifurcation. While symmetric bifurcation are divided into imperfection sensitive and insensitive, asymmetric bifurcation is obviously always imperfection sensitive. The reason for the asymmetry of this bifurcation is the fact that the arm of the spring reaction force increases as the column deflect to the left and decrease as it deflect to the right.

The imperfection sensitivity can be studied for small angle q and α, and in this case it is described by curve in Figure 2.17c which has equation:

$$P_{cr} = P_{cr}^{0} - P_1\,\alpha^{1/2}$$

Note that again the tangent of the imperfection sensitivity diagram $P_{cr}(\alpha)$ (Figure 2.17c) has a vertical downward slope at α=0, but in this case the fact that the previous equation involves a $\frac{1}{2}$ - power law rather than a $\frac{2}{3}$ - power law, which we found before, reveals that the *imperfection sensitivity* of the of this asymmetric bifurcation is *stronger* than in the previous symmetric unstable bifurcation.

To determine only the behavior near the bifurcation, Π can be approximated by a polynomial of the fourth order

$$\Pi = \frac{CL^2}{4}\left[\left(1 - \frac{q^2}{2} + \frac{q^4}{24}\right) - \left(1 - \frac{\alpha^2}{2} + \frac{\alpha^4}{24}\right) + \left(q - \frac{q^3}{6}\right) - \left(\alpha - \frac{\alpha^3}{6}\right)\right]^2 -$$

$$PL\left[\left(1 - \frac{\alpha^2}{2} + \frac{\alpha^4}{24}\right) - \left(1 - \frac{q^2}{2} + \frac{q^4}{24}\right)\right] \simeq$$

$$\frac{CL^2}{4}\,(q^2 + \alpha^2 - q^3 + \alpha q^2 + \alpha^2 q - 2\,q\alpha - 3\,\alpha^3) + \frac{PL}{24}\,(\alpha^2 - q^2)$$

The essential property of this polynomial approximation that causes the bifurcation to be asymmetric is that it contains the cubic term q^3. All terms of degree higher than cubic are not essential.

- **Nonlinear springs and polynomial approximation of potential energy**

The physical property that causes asymmetric bifurcation in the previous example is the fact that the linear elastic extensional spring installed nonhorizzontaly behaves, relative to the buckling mode, as a nonlinear rotational spring. Indeed, the elastic restraint against rotation of the rigid column about the base can be characterized by

$$dM = \tilde{C}\,dq$$

Where M is the moment of the spring force about the pivot and $\tilde{C}$ is the incremental rotational spring stiffness.

From the geometry in Figure 2.18a we have

$$M = CL^2[\cos(\gamma - q) - \cos\gamma]\sin(\gamma - q)$$

$$\frac{\partial M}{\partial q} = \tilde{C} = \frac{CL^2}{2}[2\cos^2\gamma\cos q - 2\cos 2\gamma\cos 2q + \sin 2\gamma\,(\sin q - 2\sin 2q)]$$

For small rotation

$$\frac{\partial M}{\partial q} = \tilde{C} = [CL^2\,(\cos^2\gamma - \cos 2\gamma)] - \left[\frac{3\,CL^2}{2}\sin 2\gamma\right]q = C_1 - C_2\,q$$

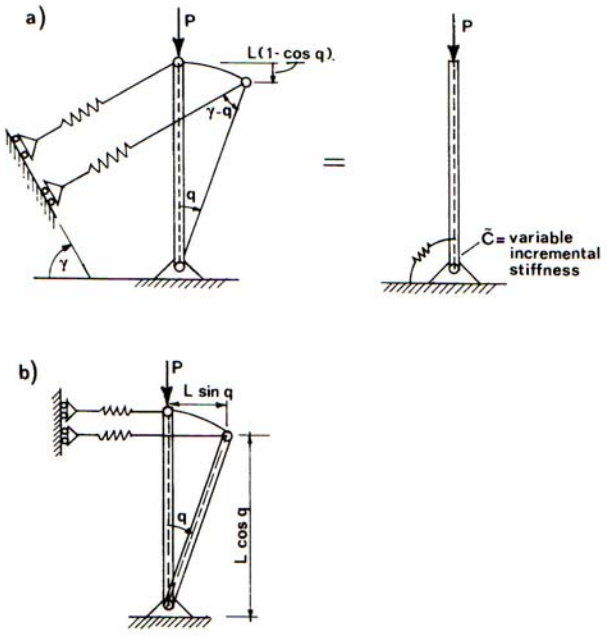

Figure 2.18. Equivalence between linear extensional spring and non-linear rotational spring. ([Bazant-Book] page 251)

Note that C_1 and C_2 are constant for fixed γ. For the imagined nonlinear rotational spring, we have, by integration, $M=\int \tilde{C}\, dq$ or

$$M = C_1 q - \frac{1}{2} C_2 q^2$$

The potential energy for the system is

$$\Pi = \int M\, dq - \mathrm{PL}(1-\cos q) = \frac{1}{2}\left(1 - \frac{P}{P_{\mathrm{cr}}}\right) C_1 q^2 - \frac{1}{6} C_2 q^3 \qquad P_{\mathrm{cr}} = \frac{C_1}{L}$$

The salient property of this polynomial expression for potential energy is that, unlike linear systems, it is not quadratic but cubic in the deflection parameter q.

The cubic form of the potential-energy expression always leads to *asymmetric bifurcation* and the associated *strong imperfection sensitivity*.

The fact that $\frac{\partial^2 \Pi}{\partial^2 q} = \left(1 - \frac{P}{P_{\mathrm{cr}}}\right) C_1 - C_2 q = 0$ at the bifurcation point, mean that one has neutral equilibrium at q=0, and the existence of neutral equilibrium means that an arbitrarily small applied moment m causes a finite rotation q.

For the special case when the linear spring is horizontal Figure 2.18b we have for the equiva lent rotational spring C_2=0.

$$M = \mathrm{CL}^2 \cos q \sin q$$

$$\frac{\partial M}{\partial q} = \tilde{C} = \mathrm{CL}^2 \cos 2q$$

For small rotation

$$\frac{\partial M}{\partial q} = \tilde{C} = [\mathrm{CL}^2] - [2\,\mathrm{CL}^2]\,q^2 = C_1 - C_3\,q^2$$

By integration

$$M = C_1\,q - \frac{1}{3}\,C_3\,q^3$$

and by further integration

$$\Pi = \frac{1}{2}\,(C_1 - \mathrm{PL})\,q^2 - \frac{1}{12}\,C_3\,q^4$$

The lack of the cubic term in Π, and the fact that the leading term, which causes nonlinear postcritical behavior, is quadratic, is typical of the *symmetric bifurcations.*

If the quadratic term is negative ($C_3 < 0$), the symmetric bifurcation is imperfection sensitive, as is true for this examples. If it is positive, the symmetric bifurcation is imperfection insensitive and exhibit a postcritical reserve. These proprieties are applicable generally.

Koiter's theory and imperfection sensitivity

As we have seen, structures exhibit various type of bifurcation and imperfection sensitivity. Elementary types of instabilities of elastic structure may be classified as follows:

1. Dynamic (energy approach is insufficient)
2. Static (Π exists, energy approach is sufficient)
   - **(a)** Snapthrough (limit point)
   - **(b)** Bifurcation
     - **i.** Stable (imperfection insensitive)
     - **ii.** Unstable (imperfection sensitive)

A completely general theory of the initial (linearized) postbuckling behavior in bifurcation-type problems was formulated by Koiter (1945) in Holland during the second world war. By examine all possible forms of the potential-energy surface near a bifurcation point, and exploiting the physically required smoothness properties, Koiter generally proved that

1. The equilibrium at the critical state is stable if load P for the adjacent postcritical equilibrium states is higher than the bifurcation load P_{cr}. The postcritical states are stable and the structure is imperfection insensitive (Figure 2.15).
2. The equilibrium at the critical state of the perfect structure is unstable if there exist adjacent postcritical equilibrium states for which load P is lower than the bifurcation load P_{cr} of the perfect structure. Imperfection cause the load at which the structure becomes unstable to be smaller than P_{cr} (Figure 2.16b and Figure 2.17b).

Koiter also proved that, among the unstable bifurcations, the asymmetric ones have much higher imperfection sensitivity than the unstable symmetric ones.

2.2.3 Inelastic theories

As pointed out in the introduction, structures can fail due to material failure, instability or to a combination of both. The material failure is normally preceded by inelastic phenomena, which generally have a destabilizing effect on structure, and must therefore be taken into account. In the previous section of this chapter, the buckling loads were determined using the elastic behaviour.

The Lagrange-Dirichlet theorem permits only dissipative forces (i.e. nonelastic phenomena) that do not destroy the existence of the potential energy function (i. e. conservative forces) from

which all conservative forces are derived by differentiation. Dissipative phenomena such as material creep (time-dependent inelastic behavior), plasticity, etc, generally make potential energy nonexistent, and thus the Lagrange-Dirichlet theorem is not applicable. However static analysis (equilibrium condition will be applied as in Section 2.2.2.2) can be conducted and the stability analysis must be based on general thermodynamic criteria.

Elastoplastic Buckling

In the structural engineering framework inelastic behaviour becomes important for columns or structures that are not too slender. Inelastic behavior can be divided into: elastic-perfectly plastic materials and hardening elasto-plastic material. As a simplification of the last one, one may consider the stress-strain diagram to be bilinear, as shown in Figure 2.19b, where: E is the initial elastic modulus, E_t is the tangent modulus and E_u is the unloading modulus.

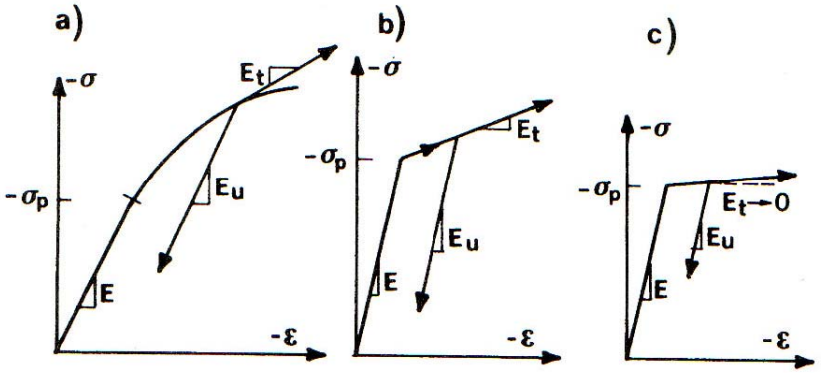

Figure 2.19. Idealized stress-strain curves of hardening plastic, bilinear, and almost perfectly plastic materials. ([BazantBook] page 487)

Reduced modulus load

Consider the perfect pin-ended column of a rectangular cross section (Figure 2.20). We now assume that the column buckles at constant axial force P. Prior to buckling (w=0), the stress distribution is uniform: $\sigma^0 = -\frac{P}{A}$ (Figure 2.20c). If the column is not too short we may assume that plane cross section remain plain and normal to the deflected centre line of the column. At the start of buckling, the concave face of the column undergoes further shortening, that is, loading and the convex face undergoes extension, that is, unloading. The neutral axis is somewhere within the cross section. Since the incremental moduli for loading and unloading are different, buckling causes a bilinear stress distribution within the cross section, as shown in Figure 2.22(d).

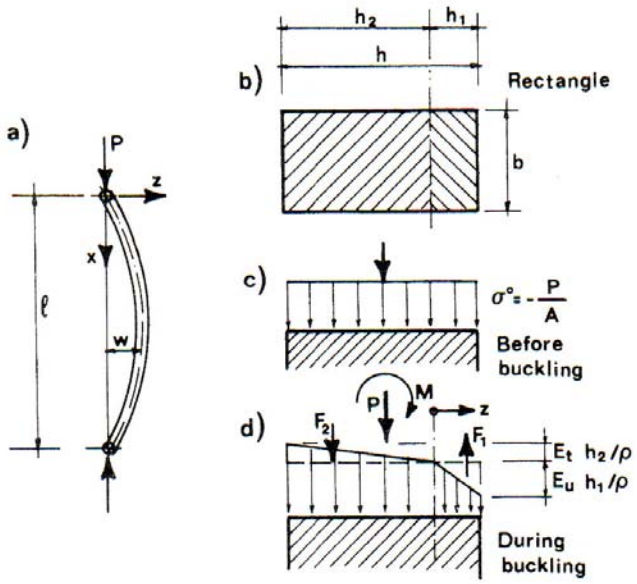

Figure 2.20. (a) Pin-ended column, (b) rectangular cross section, and stress distribution (c) before and (d) during buckling. ([BazantBook] page 488)

The condition of axial load constant that we imposed requires that the resultants F_1, and F_2, (Figure 2.20d), of the incremental normal stresses be of opposite signs and equal magnitudes, and applying equilibrium of axial forces and moment loads we can arrive at the following result

$$M = \frac{E_r I}{\rho}, \qquad E_r = \left[\frac{1}{2}\left(E_u^{-\frac{1}{2}} + E_u^{-\frac{1}{2}}\right)\right]^{-2}$$

E_r is called reduced modulus.

Applying the equilibrium condition for a pin-ended column, the first critical load is:

$$P_{cr} = P_r = \frac{\pi^2}{l^2} E_r I$$

The same analysis can be carried out for different type of sections.

The reduced modulus theory was in principle proposed by Considère (1891) and later developed by Engesser (1895) as his second theory of elastic-plastic buckling. It was further substantiated theoretically and experimentally by von Kàrmàn (1910).

Tangent modulus load

Some experimental studies conducted after the publication of von Kàrmàn's work (1910) revealed that columns can fail by buckling at load lower than the reduced modulus critical load.

The reason for this discrepancy with Engesser's second theory was explained by Shanley (1947). He showed that in a normal practical situation the column does not buckle at constant load, as assumed in the previous calculation. Rather, a perfect column, must start to deflect at a load that may lie significantly below the reduced modulus critical load.

The buckling deflections occur simultaneously with a further increase of the axial load P. In this manner, it is possible that the tensile strain increment caused by the deflection may be compensated for by the axial shortening increment due to the increase of the axial load, so that there is no unloading anywhere in the cross section (Figure 2.21).

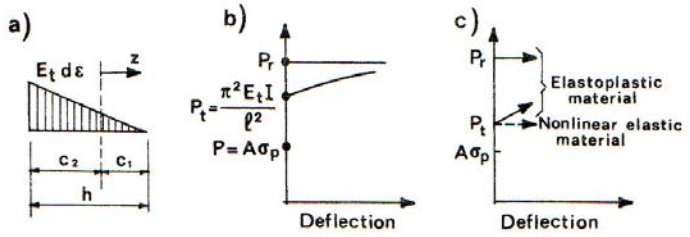

Figure 2.21. Buckling at increasing axial load: (a) stress distribution with no unloading; (b, c) load deflection curves. ([BazantBook] page 491)

This is true for both the actual curved stress-strain diagram and the idealized bilinear stress-strain diagram (Figure 2.21). Thus it appears that, at an increasing axial load, a pin-ended column of length l starts to buckle at the tangent modulus load:

$$P_t = \frac{\pi^2}{l^2} E_t I$$

This is called tangent modulus theory of Shanley, and it coincides with Engesser's first theory, which Engesser introduced in 1889 but later discarded. Note that $P_t<P_r$, except when $E=E_t=E_r$ (elastic behavior), in which case $P_t=P_r>0$, or when $E_t \to 0$, in which case the yield limit governs the start of deflection.

In the literature the experimental observed $P_{\max}$ are much closer to P_t and satisfies the bounds:

$$P_t < P_{\max} < P_r$$

Thus P_t is not only a safe lower bound for design but often also a good estimate of the carrying capacity of a column.

Postbifurcation load-deflection diagram

The analytical solution of the postbifurcation behaviour other than the initial slope is complicated. The main reason is that the boundary between loading and unloading in the cross section moves during buckling and its locations are not the same for various cross sections of the column. To avoid these difficulties, we will study from now on the idealized pin-ended column considered by Shanley (1947); see (Figure 2.22). It consist of two rigid bars of length $l/2$ connected at midspan by a very short elasto-plastic link (point hinge) of length h<<l. Let q_1 be the midspan deflection and q_2 the axial displacement on top of the column (positive for shortening). The system has two degrees of freedom. The initial equilibrium of the undeflected column at some $P=P_0$, is disturbed by applying at midheight a small lateral disturbing load f_1, while the axial load is raised by a small increment f_2, to $P=P_0+f_2$. On the concave side, the deformable segment follows the tangent modulus, while on the convex side it follows modulus ξE_t where ξ =1 if there is loading and $\xi=\frac{E_u}{E_t}>1$ if there is unloading.

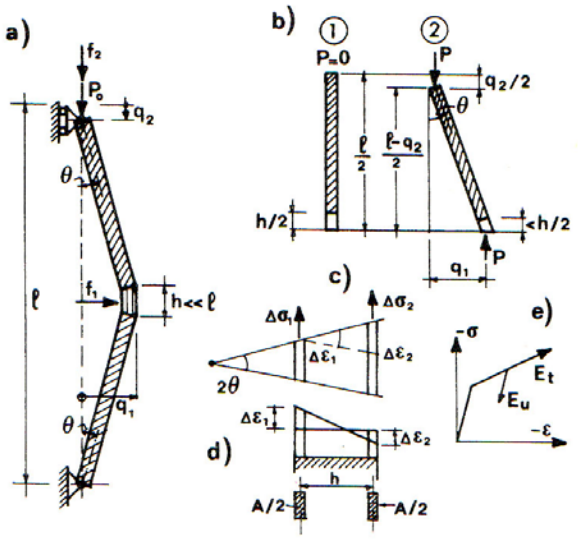

Figure 2.22. (a) Rigid-bar column with elasto-plastic link (Shanley's column). (b) geometry of deformation, (c, d) strain and stress increments in link, and (e) loading and unloading moduli ([Bazant-Book] page 495)

The compatibility of strains $\Delta\varepsilon_1$ and $\Delta\varepsilon_2$ at the concave and convex sides of a column with the displacements q_1 and q_2 provides

$$\Delta\varepsilon_1 = \frac{l}{h}(1-\cos\theta) - \frac{q_2}{h} + \frac{2\,q_1}{l-q_2}$$

$$\Delta\varepsilon_2 = \frac{l}{h}(1-\cos\theta) - \frac{q_2}{h} + \frac{2\,q_1}{l-q_2}$$

Where

$$\cos\theta = \left[1+\left(\frac{2\,q_1}{l-q_2}\right)^2\right]^{-1/2}$$

The forces and moment equilibrium are

$$P - P_0 = f_2 = -\frac{1}{2}A(E_t\,\Delta\varepsilon_1 + \xi\,E_t\,\Delta\varepsilon_2)$$

$$Pq_1 + \frac{f_1\,(l-q_2)}{4} = \frac{1}{4}\,\mathrm{Ah}(\xi\,E_t\,\Delta\varepsilon_2 - E_t\,\Delta\varepsilon_1)$$

Combining previous equation and after some rearrangements ($\cos\theta \simeq 1$, and $l - q_2 \simeq l$, which are valid for small deflections) we obtain Shanley's formula:

$$P = \frac{P_0\,(\xi-1)\,h + 4\,P_t\,\xi\,q_1}{(\xi-1)\,h + 2\,(\xi+1)\,q_1} \qquad (\text{for } f_1 = 0,\ \ q_1 \geq 0,\ \ q_1 >> q_2)$$

where $P_t = AE_t\ h/l$ = tangent modulus load.

If ξ is constant, which happens for the idealized case of bilinear stress-strain diagram, and if the stress state gets over the elastic limit, the curve $P(q_1)$ can be explicitly calculated from the previous equation.

Now an important fact to note is that, for each individual value $P_0 \geq P_t$, there exists a distinct equilibrium path $P(q_1)$. These paths are plotted as dashed lines (approximate solution for small q_1) in Figure 2.23. The vertical line $q_1 = 0$ is the main equilibrium path. Thus we see that, beyond the point P_t, the main path consists of a continuous sequence of bifurcation points. This is a phenomenal not found in elastic stability theory.

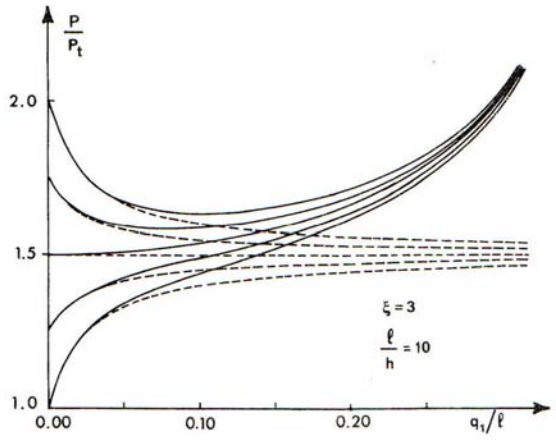

Figure 2.23. Load-deflections curves for Shanley's column: Shanley's approximate solution (dashed) and exact solution (solid) ([BazantBook] page 497)

It should be noted that the hypothesis of small q_1 can be removed and exact curves (solid curves in Figure 2.23) lie higher than the approximate solution for high value of q_1.

Imperfect Shanley rigid-bar

The imperfection analysis shows that the columns must follow the path that bifurcates to the side at P_t and cannot reach any point above this path. Load-deflection curves for the imperfect structure are shown in Figure 2.24.

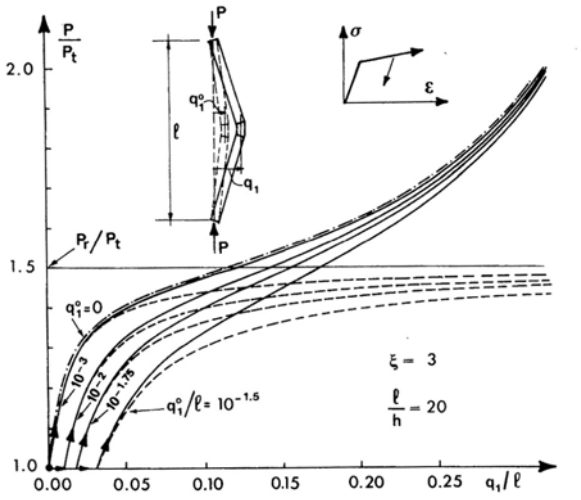

Figure 2.24. Load-deflection curves for an imperfect Shanley column (bilinear material): exact solution (solid curves) and approximate solution (dashed curves) ([BazantBook] page 507).

Most of the above arguement is developed almost identically in Bazant (1991).

2.2.4 Instability of tall structures on compressible ground

Physical understanding of the phenomenon

Why slender structures cannot be built on compressible ground above a certain height without leaning over has been effectively explained by Hambly [Hambly (1984)] in his Discourse to Royal Institution on February 8th 1985 and subsequently in his well known article [Hambly (1985)] with an experiment which could be simply reproduced [Butterfield (1997)].

Consider to built a column of bricks as vertically as possible on a compressible layer. Figure 2.25 (a), (b) and (c) illustrate a column of bricks being built on a springy foam pad.

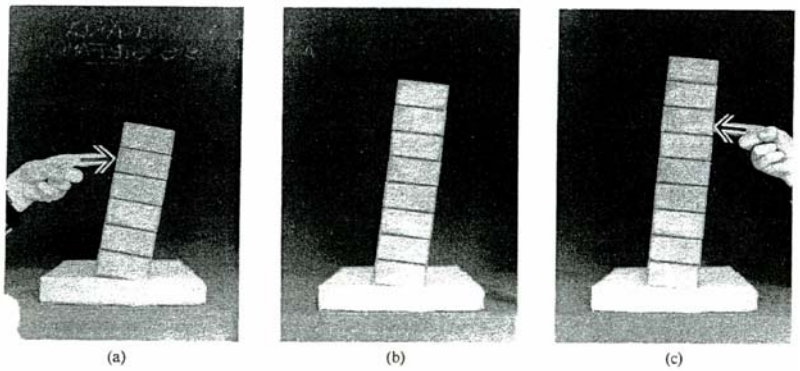

Figure 2.25. Column of bricks on a compressible stratum, in (a) stable; (b) neutral; (c) unstable equilibrium, [Hambly (1985)].

In (a) the column is short and stable, so that an horizontal force is needed to give it lean, and the column returns quickly to the vertical when the force is removed. When the column is made taller and again give a small lean it again returns to the vertical but more slowly. The building process can continue until we reach a *critical height* (b) at which it will not return to the vertical after being given a small lean, and it stays where it is left in a state of neutral equilibrium. The additional of any further weight causes it to lean over as shown in (c) and a propping force must be applied to stop it toppling. Even if the tower is built as vertically as possible it will become unstable and start to lean over as soon as the height exceeds the critical value in (b). Since all material are compressible to some extent a column on a firm foundation will start to lean if the column is tall enough.

The critical height at which a structure starts to lean can be determined from Figure 2.2(which shows the column of bricks standing on springs with the same compressibility as the foam pad. It is in a state of neutral equilibrium, as in (b). As the lean is increased the right spring compresses and the left spring relaxes. The average compression remains constant and the tower rotates about the point B midway between the springs, while the centre of gravity G moves horizontally. In Figure 2.26 the tower has tilted to the position where the centre of gravity is directly above the right spring C. In this case equilibrium of moments and forces implies that all the weight must act through the right spring, while the left spring is not loaded and its top A is at the level of zero compression. In reality the ground does not rebound as a spring. It could have slow response (clay subsoil) and stiffness could change with the time, that makes the problems much more complicated.

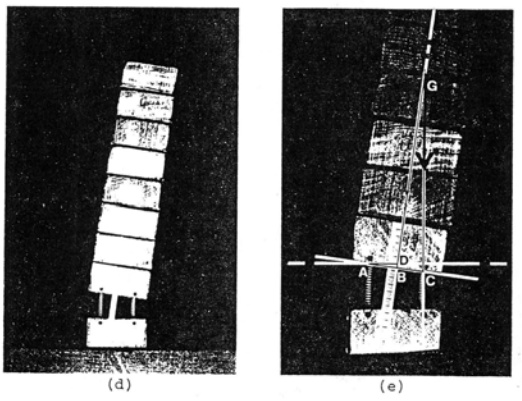

Figure 2.26. Column on springs in state of neutral equilibrium, [Hambly (1984)].

The condition of stable, neutral and unstable equilibrium of the structures on compressible foundations can be compared with the traditional definitions relevant to rigid bodies. Consider the example of the body in Figure 2.27. The body is stable if the centre of gravity (B) moves upwards when it is tilted around the hanging point A (case a)), and unstable if the centre of gravity moves downwards when it is tilted (case b)). The body has neutral stability if the centre of gravity moves horizontally or doesn't move when it is pushed or rotated (case c)). Stability analyses can be performed applying the laws of statics and dynamics, as explained in Section 2.2.2 and Section 2.3.

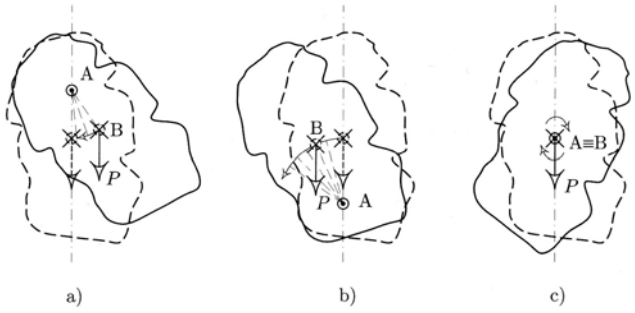

Figure 2.27. One degree of freedom rigid body, in a) stable; b) unstable; c) unstable (neutral equilibrium). ([Ferretti et al. (2002)] page 14)

The stability of a tower is a soil-structure interaction problem which has been analyzed in different ways by Habib & Puyo (1970), Habib (1982), Hambly (1985), Cheney *et al.* (1991), Lancellotta (1993), Desideri & Viggiani (1994), Como (1994), Nova & Montrasio (1995). The following sections are dedicated to their treatment.

Soil-structure interaction models

Elastic isotropic half-space

[Habib and Puyo (1970)] deduced their method for predicting instability of towers on the base of moment-rotation relationships for rigid foundations on an elastic isotropic half-space.

For the arbitrarily tilted tower of Figure 2.28 the equilibrium between externa ($M_e = W\, L_{CG}\, \sin\Delta\theta$) and resistant ($M_r = K_\theta\, \Delta\theta$) moments, for small rotation ($\sin\theta \simeq \theta$) is

$$K_\theta \Delta\theta = W L_{CG} \Delta\theta \Longrightarrow (K_\theta - W L_{CG}) \Delta\theta = 0 \tag{2.43}$$

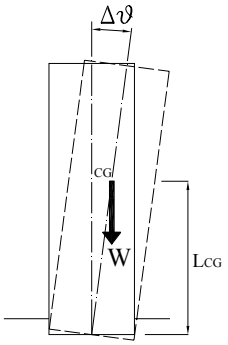

Figure 2.28. Tall structure

Wherein L_{CG} = height to center of gravity; K_θ =rotational stiffness of the foundation; W = weight of tower.

From Equation 2.43 the condition of neutral equilibrium is

$$(K_\theta - W L_{CG}) = 0 \Longrightarrow L_{CG} = \frac{K_\theta}{W} \tag{2.44}$$

Using Borowicka's equation for rotational stiffness of circular footing on an elastic half-space, $K_\theta = Ed^3 / 6(1 - \upsilon^2)$, and Equation 2.44, Habib & Pujo (1970) obtained

$$L_{CG} = \frac{Ed^3}{6W(1 - \upsilon^2)} \tag{2.45}$$

Wherein E = Young's modulus; ν = Poisson's ratio of the elastic half-space; d = diameter of plate. By taking the Boussinesq equation for settlement of a rigid circular plate $\overline{x} = \frac{W(1-\nu^2)}{E\,d}$, one obtains from Equation 2.45

$$L_{CG} = \frac{d^2}{6\overline{x}} \tag{2.46}$$

Winkler type soil model

Hambly (1985) evaluated the load at which an initially vertical tower starts to lean, assuming the soil to be represented by a layer of closely spaced, independent linear springs, equally compressible (Winkler type spring theory - Figure 2.29).

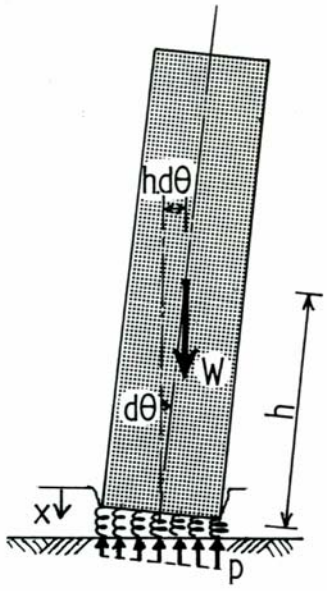

Figure 2.29. Hambly's model of tall structure on compressible stratum

The coefficient of subgrade reaction of the springs is

$$K_s = \frac{\mathrm{dp}}{\mathrm{dx}} \tag{2.47}$$

where x = displacement due to average vertical normal stress p.

If the structure leans by an angle $\mathrm{d}\theta$ as the weight is increased by ΔW, the eccentricity of the weight about the centre of the foundation causes an overturning external moment

$$\mathrm{dM}_e = (W + \Delta\mathrm{W})\, h\, \mathrm{d}\theta$$

The rotation of the foundation causes a variation in pressure, as shown in Figure 2.30a which causes a restoring moment

$$\mathrm{dM}_r = K_\theta\ \mathrm{d}\theta = I_e \frac{\mathrm{dp}}{\mathrm{dx}}\, \mathrm{d}\theta$$

wherein I = the second moment of area of the base cross-sectional area A.

Equilibrium of restoring and overturning external moments (equivalent to Equation 2.44) requires that

$$(W + \Delta\mathrm{W})\, h\, \mathrm{d}\theta = I_e \frac{\mathrm{dp}}{\mathrm{dx}}\, \mathrm{d}\theta \tag{2.48}$$

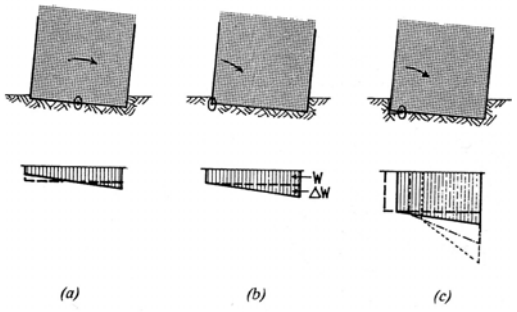

Figure 2.30. Bearing pressure diagrams under foundation during: (a) unstable lean on elastic ground; (b) stable lean on yielding ground with bearing resistance increasing with settlement (work hardening); (c) unstable lean on yielding ground of (b). [Hambly (1985)].

Since the ground, modelled as a bed of elastic springs, recovers during a decrease in pressure, then the pressure diagram would be as shown in Figure 2.30a, and the structure would fal over without needing an increase in load ($\Delta W=0$).

The elastic limit weight W_e and height h_e are, from Equation 2.48

$$W_e h_e = I_e \frac{\mathrm{dp}}{\mathrm{dx}} \tag{2.49}$$

If A = area of the foundation and r_e = radius of gyration of foundation about a horizontal axis through the centroid, than Equation 2.49 becomes

$$W_e h_e = r_e^2 A \frac{\mathrm{dp}}{\mathrm{dx}} \tag{2.50}$$

By taking the average vertical displacement ($\overline{x}$) proportional to average bearing pressure W/A, than at the start of the lean

$$\frac{\mathrm{dp}}{\mathrm{dx}} = \frac{W_e}{A\,\overline{x}_e}$$

This can be combined with Equation 2.50 to give the conditions at which the structure starts to lean:

$$\frac{h_e\,\overline{x}_e}{r_e^2} = 1 \tag{2.51}$$

For a circular plate, r_e^2=I/A = (d^2/16), which yields on substitution into Equation 2.51

$$h_e = L_{CG} = \frac{d^2}{16\,\overline{x}}$$

Comparing Habib's and Hambly's solutions one sees that elastic half-space theory gives a critical height 2,7 times greater than that of the Winkler-type spring theory. The differences between these two predictions comes from the difference in the stress distribution beneath the tower in the two cases.

Hambly pointed out that real ground work-hardens and does not recover when the pressure is reduced. As a result, structure do not fall over uncontrollably when the elastic limit weight is reached. However, W_e still represents the weight at which a centrally loaded structure on work-hardening ground ceases to settle uniformly and starts to lean (in a stable manner). The increment of weight ΔW then causes the change in pressure diagram in Figure 2.30b. On the settling side the lean doubles the increment of pressure due to ΔW, while on the non-settling

side the pressure remains temporarily constant as the lean cancel the effect of the ΔW. The increase in average pressure has no moment about the center of the foundation and consequently, while ΔW is small, all previous equations still apply. The structure starts to lean at the load of elastic formula, and than requires additional load to make the lean increase. *As Hambly demonstrated, in that way, this behaviour is essentially the same as the buckling of inelastic structures* (Section 2.2.3). *In inelastic structures the start of buckling arrives at the load predicted by the Eulero's elastic formula in which the tangent modulus of the material is applied*.

The structure cannot be loaded above a certain upper bound yield limit load W_y at height h_y at which it will fall over uncontrollably. Figure 2.30c shows the bearing pressure diagram for this situation as the lean starts to develop. The axis of rotation moves away from the non-settling edge as the volume under the pressure diagram remains constant. The overturning external moment is now given by

$$dM_e = W_y h_y d\theta$$

The rotation $d\theta$ causes an increase in the supporting pressure on the right with a triangular distribution. Since the total weight remains constant the ground at the left edge must unload as the centre of rotation moves to the right. At the initiation of the unstable lean, when the centre of rotation is closed to the non-settling edge, the triangular pressure increase on the right and the release at the left form a restoring moment

$$dM_r = I_y \frac{dp}{dx} d\theta$$

wherein I_y = the second moment of area of the foundation about horizontal axis of rotation at edge of foundation.

Equilibrium of overturning and restoring moments requires

$$W_y h_y = I_y \frac{dp}{dx} \tag{2.52}$$

This is the maximum weight and height that can stand vertically on the foundation, and it is analogous to the reduced modulus buckling load for an inelastic structure (Section 2.2.3). It is an upper bound since a lean causes a reduction in the weight that can be supported. It could be shown, by analogy with Equation 2.51, that, called $\overline{x}_y$ the settlement associated with the maximum height h_y, they are related to the radius of gyration r_y by the following equation

$$\frac{h_y \overline{x}_y}{r_y^2} = 1 \tag{2.53}$$

Hambly pointed out two aspects of his analysis related to the application to real soils: *non homogeneity* and *time dependent* behaviour. In the first case he suggest that, if the soil conditions are complex (i. e. interbedded layers), the rotational stiffness ($\frac{dM_r}{d\theta}$) of the ground must be defined using finite element or equivalent analysis. By equating the overturning and restraining moments at the start of the lean, as before:

$$dM_e = dM_r \Longrightarrow W h d\theta = \frac{dM_r}{d\theta} d\theta \tag{2.54}$$

Hence, at the start of lean

$$W h = \frac{dM_r}{d\theta}$$

The second aspect concerns time effects, which, up to now, have been ignored. This topic will be analyzed in a following section.

Physical models

Physical data are always very important in the verification of theoretical methods, but not many tests are available related to the stability of leaning towers. One of the most important investigations was carried out by Cheney *et al.* [Cheney, Abghari and Kutter (1991)]

They made centrifuge model tests on towers having small initial tilt to determine the critical height of tower that causes instability and presented two approaches that gave close correlation with experimental results. These approaches were based on: (1) experimental determination of rotational stiffness of the soil foundation system (the importance of its definition was pointed out previously by [Hambly (1985)]); (2) a method analogous to that proposed by Southwell for predicting the stability of imperfect columns (For details see [Bazant and Cedolin (1991)], pages 24-26).

Note that elastic solutions described above assume that the tower is vertical until bifurcation occurs at critical load, while, as Cheney *et al.*(1991) emphasised, in all real cases the towers rotate to a position of equilibrium from the beginning of construction, and stability must be determined by analysis of the tilted equilibrium position.

Let us concentrate on the first approach proposed, the one based on a moment-rotation plot. From the onset of construction, there will be a tilt θ_0 that is not associated with the resisting moment, so that the resisting moment from the ground is a non-linear function of $\theta - \theta_0$,

$$M_r = f(\theta - \theta_0)$$

For the arbitrarily tilted tower of Figure 2.31 the equilibrium between external overturning ($M_e = W L_{CG} \sin\theta$) and resistant ($M_r = f(\theta - \theta_0)$) moments, for small rotation ($\sin\theta \simeq \theta$) is

$$M_r = W L_{CG} \theta \tag{2.55}$$

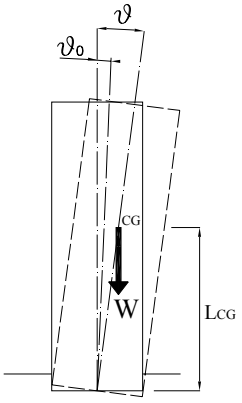

Figure 2.31. Tall structure with initial tilt

Equation 2.55 has a graphical solution shown in Figure 2.32. Equilibrium occurs either points B or C on the M_r curve, depending upon loading history. B is a stable equilibrium because for small increase in θ, M_r rises faster than M_0 ($\frac{dM_r}{d\theta} > \frac{dM_0}{d\theta}$). The solution at C is unstable owing to the condition that $\frac{dM_r}{d\theta} < \frac{dM_0}{d\theta}$. The critical condition occurs at B', when

$$\frac{dM_r}{d\theta} = W L_{CG} \tag{2.56}$$

Thus if θ_0 is known and the moment-rotation relation is known, the critical slope $(WL_{CG})_{cr}$ can be determined graphically.

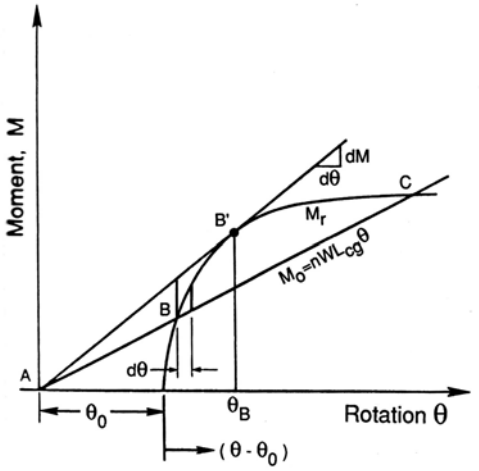

Figure 2.32. Graphical solution for tilt instability using a foundation moment-rotation relationship [Cheney, Abghari and Kutter (1991)].

This work emphasises the importance of the knowledge of the moment-rotation relationship and presents results of physical model tests.

The centrifuge modelling of tower stability was used in two ways: (1) to determine experimentally the moment-rotation curve; and (2) to determine experimentally the stability of model tall towers. Figure 2.33 shows superimposed plots obtained during the test for three normal loads P.

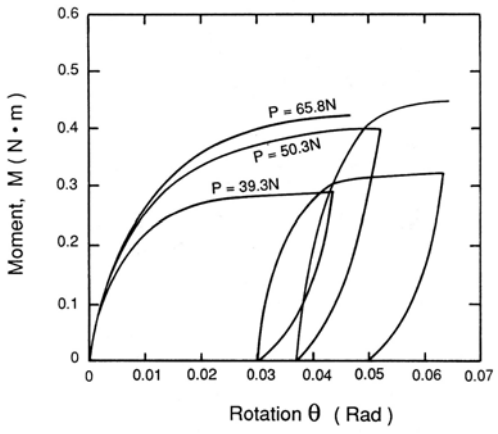

Figure 2.33. Moment versus rotation for a 38 mm diameter circular foundation on Kaolin clay [Cheney, Abghari and Kutter (1991)].

A comparison between Hambly's and Habib's methods and the tests results was carried out, even if they are not strictly appropriate because they considered an initially vertical tower, whereas tests were performed on towers with initial tilt. Nevertheless, it was clear that Habib & Puyo solution overpredicts the actual failure height, in some cases drastically, while Hambly's

method almost always underpredicts the critical height, and never overpredicts. Therefore the latter appears adequate.

Another important contribution rewards the interpretation of the effect of continued additional tilting. It was suggested that the θ_0 could be considered as changing in time due to creep behaviour, consequently the moment-rotation curve is unchanged owing to creep deformation. Therefore the effect of creep is to reduce the factor of safety with respect to critical initial angle $\theta_{0\,cr}$, where θ_0 corresponds to a tilt when the foundation reaction M = 0.

In this case, Equation 2.55 can be rewritten to be

$$M_{r(\theta-\theta_0-\theta_{creep})} = W\, L_{CG}\, \theta \tag{2.57}$$

where the added θ_{creep} may be treated as an additional shift in the M_r curve. With reference to Figure 2.34 a factor of safety with respect to the critical initial angle may be defined as

$$FS_\theta = \frac{\theta_{0\,cr}}{\theta_0} \tag{2.58}$$

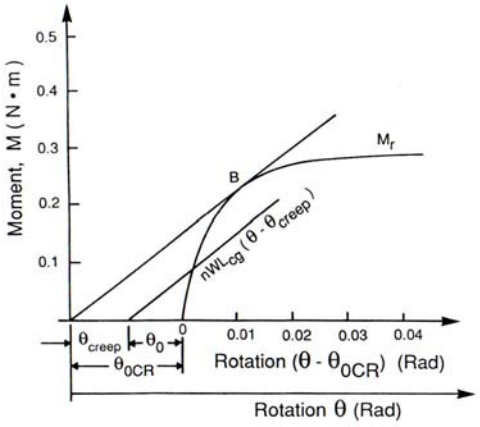

Figure 2.34. Graphical solution for critical angle for instability of tall towers [Cheney, Abghari and Kutter (1991)].

This is especially important if the tower's tilting is progressive. It is emphasized that, although creep behaviour may lead to a critical condition, the delay time may also provide some strengthening owing to consolidation that offsets the arrival at a critical condition. The M_r curve may grow in time as the curves in Figure 2.34 indicate.

Many aspects of tower behaviour were pointed out in Cheney *et al*. (1991) and afterwards quoted by different authors.

More recently further centrifuge tests on models have been carried out related to the Pisa Tower.

Non linear rotational spring

The non linear rotational spring (Figure 2.35) was adopted by Lancellotta [Lancellotta (1993)] in his stability analysis of Pisa Tower and in the interpretation of possible restoring measures.

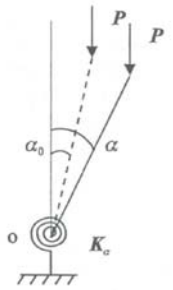

Figure 2.35. Column and spring in [Lancellotta (1993)].

The eccentricity of the weight from the centre of the foundation causes an overturning external moment

$$M_e = P\,h \sin\alpha$$

The response of the spring is expressed by the non-linear law

$$M_r = A[1 - e^{-B(\alpha-\alpha_0)}]$$

The load-rotation curve for Pisa Tower are shown in Figure 2.36. Parameters of the mode (A, B and α_0) were calibrated on the historical movements of the tower and on available data on soil properties.

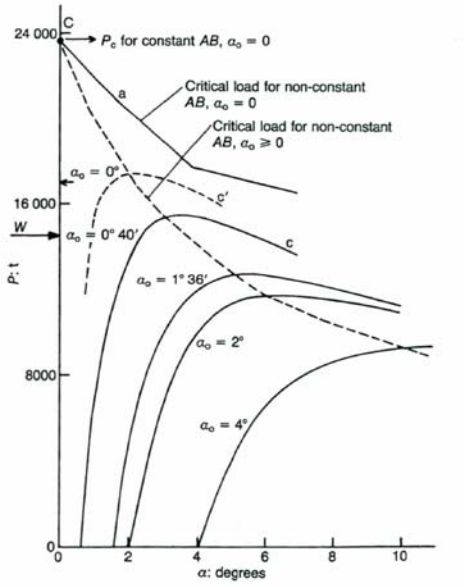

Figure 2.36. Load-rotation curve for Pisa tower, [Lancellotta (1993)].

The first important note, previously emphasized also by Cheney *et al.*(1991), is the decrease of critical load with the increase of initial tilt α_0, which can incorporate additional creep rotation. Lancellotta also shows how the factor of safety against instability could be increased by applying a tendon Figure 2.37 and the improvement can be simply displayed on the curves (dash-dot curve c' in Figure 2.36).

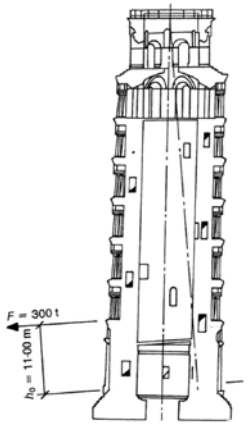

Figure 2.37. Leaning Tower of Pisa: possible safety measure [Lancellotta (1993)].

Two degree of freedom models

The inelastic and time dependent behaviour of soils are fundamental aspects of the stability of towers. Taking them into acccount explicitly is quite complex. Lancellotta (1993) and Cheney *et al.* (1991) suggested incorporating creep in the initially generally unknown tilt. An attempt to consider explicitly time was made by Hambly. Pepe (1995), carried out an elasto-plastic analysis of the safety margin of the Pisa tower. Both of them adopted an idealised two degree of freedom system as in Shanley's application (Section 2.2.3.1).

Hambly [Hambly (1985)] suggested considering the structure in Figure 2.38 in order to take into account the existence of viscous phenomena. In this case the tower is supported on two spring-damper systems, each of stiffness k/2 and damping c/2, at lever arms of *r* from the centreline.

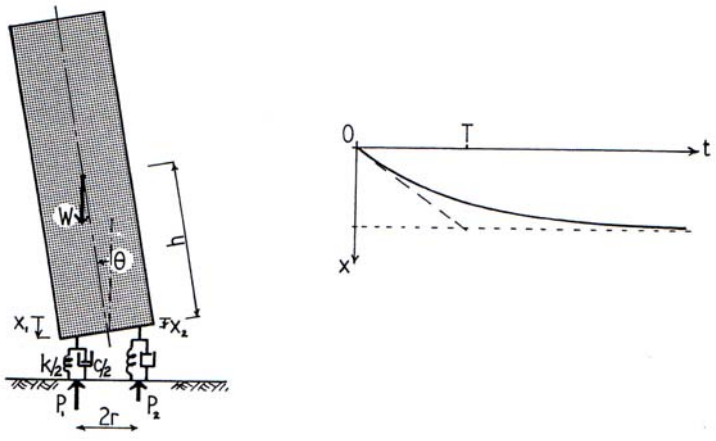

Figure 2.38. Leaning instability of time dependent foundation, [Hambly (1985)].

Solving vertical forces equilibrium, assuming an exponential time-settlement curve for the dashpot in Figure 2.38, and equilibrating moments about the middle of the foundation, it can be demonstrated that

$$\frac{x_1 - x_2}{2} = C \exp\left((\mathrm{Wh} - \mathrm{kr}^2)\frac{t}{cr^2}\right)$$

It can be seen that, if $\frac{\mathrm{Wh}}{r^2} < \mathrm{k}$, the exponent is negative and the inclination decreases with time. On the other hand, the lean will grow uncontrollably when Wh exceeds

$$\mathrm{Wh} = \mathrm{kr}^2$$

which can be simply equated to Equation 2.50.

Pepe [Pepe (1995)] reported and discussed results obtained from centrifuge model tests of the Tower of Pisa, carried out at ISMES. They gave further insight into the mechanisms of instability and confirmed the elastoplastic character of the restraint exerted by the foundation and subsoil on the motion of the tower. The theoretical interpretation was made using a Shanley's application.

Strain hardening models

The idea of appliyng complete theoretical models to the analysis of stability of towers was pioneered by Como [Como (1993)], and then developed by Desideri *et al.* [Desideri, Russo and Viggiani (1997)], Nova & Montrasio [Nova and Montrasio (1995)].

The great potentiality of these models is to combine, in the same analysis, stiffness and strength evaluations.

Complete theoretical models, all expressed in terms of work-hardening plasticity theory, have been developed for specific tests. Como (1994) outlined both the plastic respons of the foundation under increasing tilting and the delayed rotation due to soil creep.

In Desideri *et al.* (1997) the stability of equilibrium of towers on deformable ground is modelled with reference to an inverted pendulum resting on a strain hardening Winkler type elastoplastic material.

Nova & Montrasio (1995) applied their model [Nova and Montrasio (1991)] to the Tower of Pisa with an extension to time dependent phenomena, but without interpretation of the instability.

The interpretation of tall structure behavior using elasto-plasticity will be further investigated in the subsequent chapters.

PART II - *Theoretical contribution*

CHAPTER **3**

Improved Plastic Potentials & hardening rules for surface pads -*contribution* to design tools-

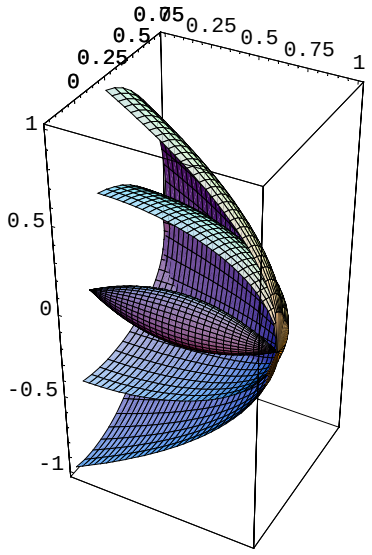

Figure 3.1. Plotting of the "cigar shaped" yield surface, elliptic radial and parabolic tangential plastic potentials.

"For the sake of …..persons of different type, scientific truth should be presented in different forms, and should be regarded as equally scientific, whether it appears in the robust form and vivid colouring of a physical illustration, or in the tenuity and paleness of a symbolic expression."

James Clerk Maxwell (1870)

Introduction

—This chapter explains the origin and development of “universal load-path” plastic potentials (Figure 3.1) for predicting the displacements of surface pads subjected to combined load. It also includes discussion of modified hardening rules and a new method of estimating a vertical stiffness curve from oedometer tests. A numerical model incorporating all these developments has been used to generate the M-θ curve used for the analysis developed in the following chapters.

3.1 Development of a strain hardening law from oedometer tests

The hardening law used in strain hardening models for surface pads is a vertical central load-vertical plastic displacement curve. Different equations have been to date suggested on the basis of fitting experimental data for each specific reference test (see Section 2.1.3).

This Section explains the origin of a vertical load-displacement curve in terms of the compression parameters defined in the “log v-log p’” plane, following the Butterfield compression model [Butterfield (1979)]and subsequent written communications.

3.1.1 The compression model in the “log v - log p’” plane

The following diagram (Figure 3.2) illustrates Butterfield’s augmented compression model.

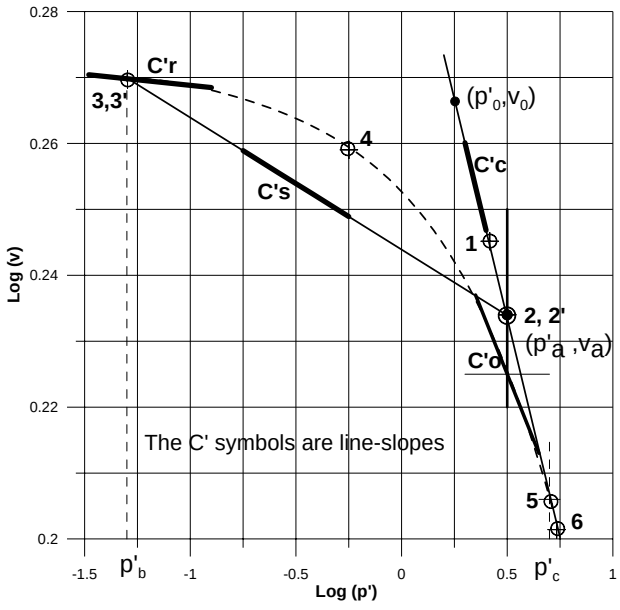

Figure 3.2. The compression model.

The compression parameters involved are: $C_r^{'}$, $C_0^{'}$, $C_s^{'}$, $C_c^{'}$ (Figure 3.2).

If the overconsolidation ratio is OCR then :

$$p_2' = \mathrm{OCR} \cdot p_3' \tag{3.1}$$

From which the derived parameter

$$\frac{1}{\eta} = \frac{\mathrm{Ln}(C_0'/C_r')}{\mathrm{Ln}(\mathrm{OCR})} \tag{3.2}$$

Although C_r' is the least well defined of the C' parameters, all of them are interrelated by an identity that enables a consistent value of C_r' to be determined iteratively.

Some typical parameter values for C_0' and C_0'/C_r' have been established from conventional oedometer tests (Table 3.1).

Table 3.1. Typical parameter values in the compression model

Soil	C_0'	C_0'/C_r'	w_L [%]	*PI*[%]
Boston-Cambridge Clay	0.0722	9	40	18
Remoulded Kaolin	0.0608	15	52	22
Venetian silty clay	0.0385	13	34	14
Venetian clay	0.080	22	62	28
Venetian fine sand	0.0216	24	-	-

They appear to correlate reasonably with plasticity indices.

The elaboration of an oedometer test using this model on the Pisa Tower subsoil using this model is shown in Figure 3.3.

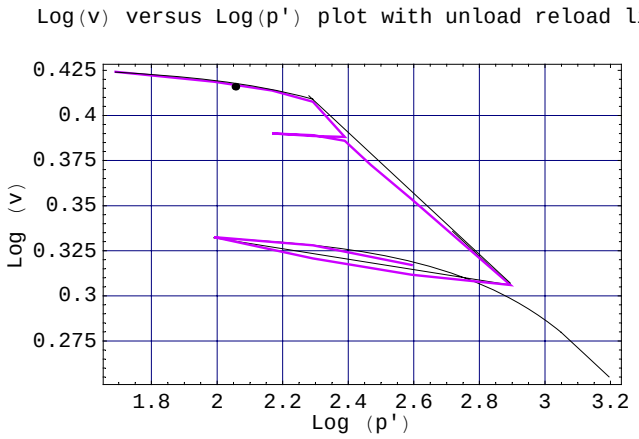

Figure 3.3. Example of the interpretation of an oedometer test on the Pisa Tower subsoil.

3.1.2 The hardening law from oedometer tests

Assume point 3 (Figure 3.2) to be the representative state of a soil element at depth z:

$$p'_3 = \gamma' \cdot z \tag{3.3}$$

where γ' is the effective unit weight of the soil (c. 10 kN/m^3).

A relationship between the thicknesses (h_3, h) of a soil layer and effective vertical stresses (p'_3, p') along a (3, 4, 5) load path (Figure 3.2) can be derived as follows.

Note that the "log v - log p'" development is fundamentally a finite deformation model.

From Butterfield (1979) paper

$$\text{Ln}\,\frac{h}{h_3} = \eta C'_r \left(1 - \frac{p'}{p'_3}\right)^{1/\eta} \tag{3.4}$$

and from Equation 3.2

$$\left(\frac{p'_2}{p'_3}\right)^{1/\eta} = \frac{C'_0}{C'_r} \tag{3.5}$$

Since $\frac{w}{h_3}$ is very small

$$\text{Ln}\,\frac{h}{h_3} = \text{Ln}\left(\frac{h_3 - w}{h_3}\right) = \text{Ln}\left(1 - \frac{w}{h_3}\right) = -\frac{w}{h_3} \tag{3.6}$$

In infinitesimal terms

$$\frac{w}{h_3} = \frac{\text{dw}}{\text{dz}} \tag{3.7}$$

Substituting Equation 3.6 in Equation 3.4

$$-\frac{\text{dw}}{\text{dz}} = \eta C'_r \left(1 - \frac{p'}{p'_3}\right)^{1/\eta} \Rightarrow w = h_3\, \eta C'_r \left(1 - \frac{p'}{p'_3}\right)^{1/\eta} \tag{3.8}$$

$$\text{dw} = \eta C'_r \left[\left(\frac{p'_3 + p'}{p'_3}\right)^{1/\eta} - 1\right] \frac{C'_0}{C'_r} \left(\frac{p'_2}{p'_3}\right)^{1/\eta} \text{dz} \tag{3.9}$$

$$\text{dw} = \eta C'_0 \left[\left(\frac{p'_3 + p'}{p'_2}\right)^{1/\eta} - \left(\frac{p'_3}{p'_2}\right)^{1/\eta}\right] \text{dz} \tag{3.10}$$

$$\text{dw} = \eta C'_0 \left[\left(\frac{p'_3 + p'}{p'_2}\right)^{1/\eta} - \left(\frac{p'_3}{p'_2}\right)^{1/\eta}\right] \text{dz} \tag{3.11}$$

$$\text{dw} = \frac{\eta C'_0}{\text{OCR}^{1/\eta}} \left[\left(1 + \frac{p'}{p'_3}\right)^{1/\eta} - 1\right] \text{dz} \tag{3.12}$$

If we substitute Equation 3.3 in Equation 3.12, then

$$\text{dw} = \frac{\eta C'_0}{\text{OCR}^{1/\eta}} \left[\left(1 + \frac{p'}{\gamma' \cdot z}\right)^{1/\eta} - 1\right] \text{dz} \tag{3.13}$$

Note that both OCR and p' can be expressed in terms of the depth z. OCR follows an hyperbolic trend

$$OCR = \left(1 + \frac{n}{z}\right) \tag{3.14}$$

The parameter *n* can be immediately defined from the value of OCR at a known depth. This is a very simple determination if there is the possibility of testing an undisturbed sample.

The increment of pressure at depth z, due to a $p_0^{'}$ pressure applied uniformly over a circular area on an elastic half-space at ground level, can be defined using the *Boussinesque* formula (Figure 3.4).

$$p' = 1 + p_0^{'}\left\{1 - \frac{1}{\left[1 + (\frac{r}{z})^2\right]^{1/2}}\right\} \tag{3.15}$$

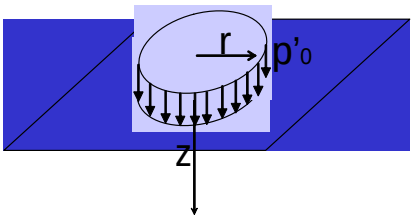

Figure 3.4. Schematic picture of the circular equivalent foundation on the elastic half-space.

where r is the equivalent radius of the foundation (2R/2 in the model applied in Section 3.3).

Substituting Equation 3.14 and Equation 3.15 in Equation 3.12

$$dw = \frac{\eta C_0^{'}}{(1 + \frac{n}{z})^{1/\eta}}\left[\left(1 + \frac{1 + p_0^{'}\left\{1 - \frac{1}{(1+(\frac{r}{z})^2)^{1/2}}\right\}}{\gamma' \cdot z}\right)^{1/\eta} - 1\right] dz \tag{3.16}$$

Equation 3.16 can be integrated between the surface of the soil (z=0) down to an arbitrary cut off depth ($z=z_{max}$), say,

$$z_{max} = 3\,(2\,r) \tag{3.17}$$

where (2*r*, 2R in the model applied in Section 3.3) is the effective breath of the foundation.

Values of *w*, calculated integrating Equation 3.16 for every value of $p_0^{'}$ between 0 and the maximum value of pressure applied to the soil (i. e. weight of the soil divided for the foundation area), constitute the hardening law. In this way the hardening law is defined point by point. This numerical solution can then be fitted by a convenient equation, possible functions are:

- a modified exponential

$$V_0 = A(1 - e^{-Bw}) \tag{3.18}$$

- or a hyperbolic expression

$$V_0 = \frac{A\,w}{B + w} \tag{3.19}$$

Two examples of hardening law have been developed in Chapter 5 for the Pisa Tower and the Santo Stefano bell tower. The Pisa Tower hardening law is also shown in Figure 3.5.

The reference input parameters in this case are:

W = 142 MN; B = 19 m; γ‘ = 9 KN/m^3 ; z_{max} = 3 B; $p_{o,max}^{'}$ = 2 W/B^2 ;

$C_0^{'}$=.08; $C_0^{'}/C_r^{'}$ = 8; n = 16;

Its equation is

$$Vo = 410\,(1 - e^{-0.2\,w_p}) \tag{3.20}$$

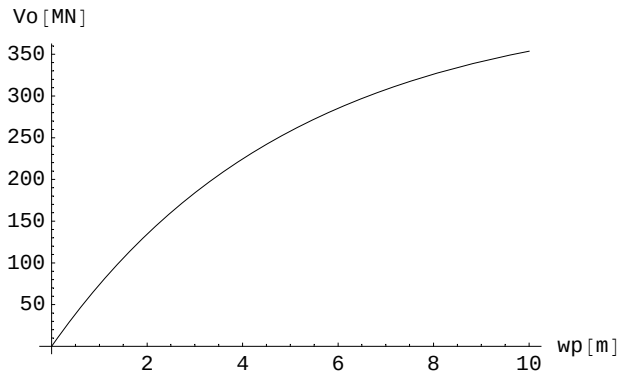

Figure 3.5. Pisa Tower hardening law

3.2 Scaled hardening law

From an inspection of tests performed in the Gottardi (1992) PhD Thesis it is evident that the application of the strain hardening law directly in terms of (V_0, w_0) is not adequate. By analogy with Critical State Soil Mechanics it underlines the fact that for the surface pads the value of the vertical displacement does not depend solely on the current value of the hardening parameter (*Vo* in the present case), but also on the value of the current load. Indeed, the application of the hardening suggest that all tests, characterized by the same V_{max} (i. e. the same failure envelope, see tests A5, B9, B8, A7, and D2 in Figure 3.6 and Figure 3.7) will have the same final value of $w_{p,max}$. This is clearly not supported by the experimental evidences. More satisfactorily the final value of $w_{p,max}$ can be deduced through a linear proportion (see red line in Figure 3.6) depending on the ratio between the current vertical load (V) and the hardening parameter (V_o). A possible formulation of this scaling, used in subsequent model, is

$$\boxed{w_{p,mod} = w_p \cdot \left[1 - s\left(1 - \frac{V}{V_o[w_p]}\right)\right]} \tag{3.21}$$

Where s is a factor which allows for control of the scaling impact. Note that $s=0.9$ is the assumed value, based on test data observation, s=1 is the maximum scaling while s=0 implies no scaling.

The suggested linear proportion is quite primitive but captures the essence of the problem, as shown by the results of the simulation in Section 3.3.

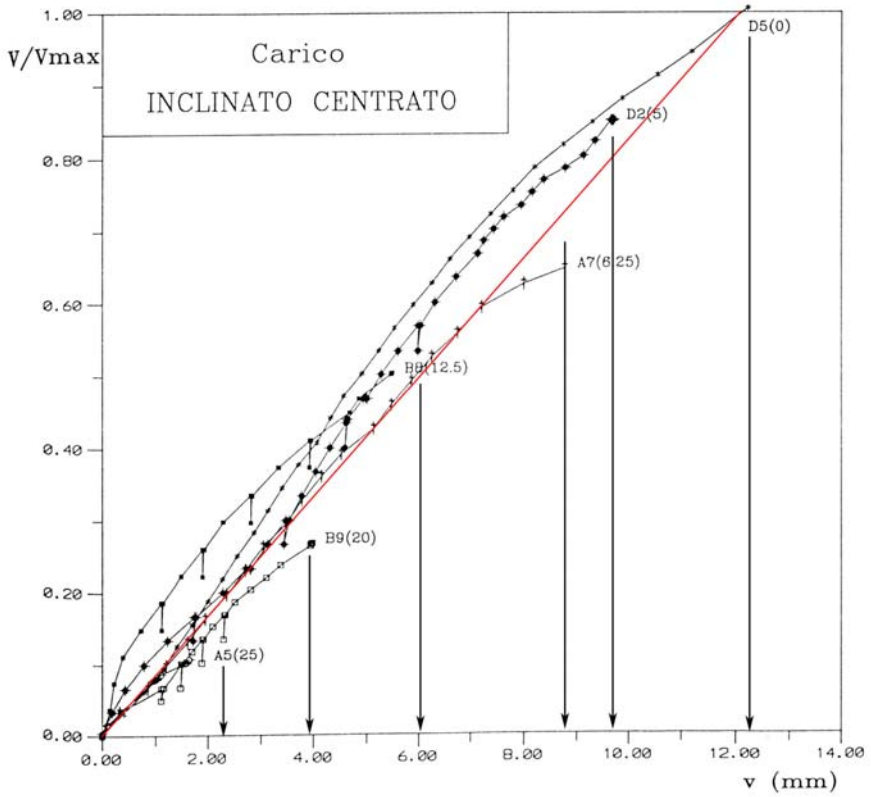

Figure 3.6. Load - settlement curves from central inclined load tests [Gottardi (1992)].

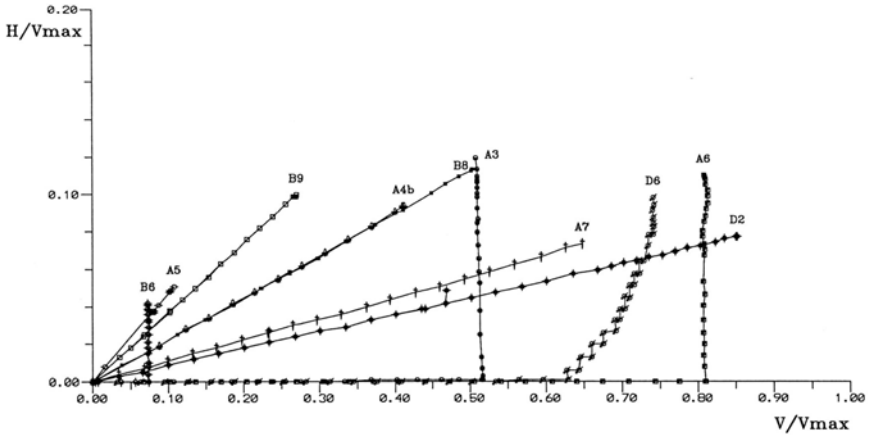

Figure 3.7. Load paths in the (V/V_{max} - H/V_{max}) plane [Gottardi (1992)].

3.3 Improved Plastic Potentials for surface pad foundations

The application of previous model based a on work-hardening plasticity framework (i.e. [Nova and Montrasio (1991)] and [Houlsby and Cassidy (2002)]) encounters difficulties when it is used to predict displacements of surface pads under general load paths. The problem is generally characterized by a non associated flow rule, but, up to now, the proposed formulations do not give satisfactory results.
This section, which describe the development of a new plastic potential system, is composed of two parts: the first is the theoretical analysis and the analytical formulation of plastic potentials [Butterfield (1981)] (Section 3.3.1 and Section 3.3.2), whereas the second part (Section 3.3.3) describes the comparison between experimental data and predicted displacements, with the aim of establishing the validity of the new formulation.

The intention is to develop "*universal load-path*" plastic potentials (*g*) for surface pad foundations based on simple geometric shapes (i.e. 3D rotated ellipsoid or functions has been investigated, in order to fit laboratory data. These forms will provide paraboloid) centred on the (*M/2R, H, V*) origin (0,0,0). The simplest possible useful form of theoretically adequate estimates of post-consolidation displacements due to applied (*M/2R, H, V*) loading, whereas slightly elaborated forms are necessary in order to interpret more precise data from laboratory experiments.

3.3.1 Theoretical elaboration

Introduction to experimental tests

The small scale "1g" footing tests, carried out by Gottardi in Padova [Gottardi (1992)], have been used. In this experimental work the soil used was a very dense sand and the shape of the footing rectangular (100x50 mm).

Note that (Figure 3.8) the term '*radial*' refers to those load paths which increase monotonically along paths passing through the load origin; the term '*tangential*' to those at right angles to the V axis emanating from any point along it (i.e. those that increase monotonically in any (*H, M/2R*) plane). Note that the V axis is clearly a radial path.

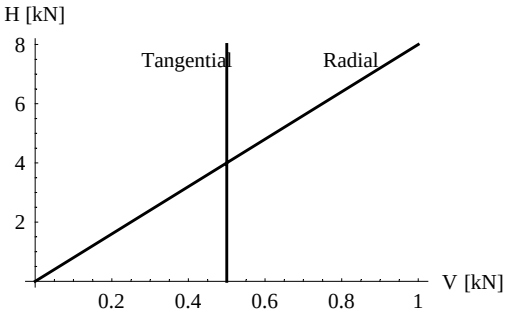

Figure 3.8. Example of radial and tangential load paths in the H-V plane.

Tests considered in this analysis are summarized in Table 3.2.

Table 3.2. Tests from Gottardi (1992)

Load path	*Tests*					
Radial (H-V)	A4	A5	A7	B8	B9	D2
Radial (M-V)	B2	B3	B7	-	-	-
Tangential (H-V)	A3	A6	B6	-	-	-
Tangential (M-V)	-	-	-	-	-	-
General (H-V)	D1	D3	-	-	-	-
General (M-V)	-	-	-	-	-	-

Test used to calibrate the plastic potential equations are: A7, B8, B9, D2 in the radial H-V plane; B2, B3, B7 in the radial M-V tests and A3, A6, B6 in the tangential H-V tests. D1 and D3 are general load path tests which have been used to verify the effectiveness of the proposed formulation.

Multiple plastic potentials

The observation of tests from Gottardi (1992) suggest the existence of a minimum of two different plastic potentials, associated, in some way, with specific load paths. In fact, the displacement increment vectors along tangential load paths are almost parallel, while in radial paths they bend. This creates an intriguing problem at the intersection of a radial path with a tangential ones since the vectors are certainly not coincident there. The direction of a displacement vector appears, in general, to be not only a function of the direction of the applied load increment but also of the direction of the load path followed prior to arriving at the point.

That this difficulty may be overcome using a single family of yield surfaces (*f*) and a minimum of two families of plastic potential surfaces (*g*) is the hypothesis now being investigated.

It is already accepted the notion of simultaneous isotropic and translational hardening for *f* (parabolic shape) and (following [Koiter (1953)]) multiple yield surfaces; we can consider a similar notion for *g*.

Tests support that the flow is approximately associated in the '*transversal' (H, M/2R)* plane (i.e. $g = f$ in this plane and therefore *g* has the form of a slightly rotated ellipse) [Gottardi, Houlsby and Butterfield (1999)].

In *'radial' (H, V)* and *(M/2R, V)* planes (i.e. planes in which the *V* axis is embedded) the flow is strongly non-associated and two geometrically simple forms of *g* are proposed:

1. For '*radial*' load paths *g* takes the form of a semi-ellipse, centred on the origin. In (*M/2R, H, V*) space this becomes a *semi-ellipsoid* with inclined ellipsoidal cross-sections that intersect the *V* axis orthogonally. In reality the shape of such an elliptic *g* changes slightly as the tip of the *f* parabola traverses the *V* axis, a simple scaling law involving the (V_o/V_{max}) ratio can accommodate this and produces the typical bending of the displacement paths generated by radial loading.
2. For '*tangential*' load paths the basic form of g is a simple *parabola,* with its apex on the V axis, located symmetrically with respect to this axis (it therefore intersects this

axis orthogonally but meets the (*H,M/2R*) plane at an angle). In reality such a parabolic *g* is not adequate and the simple (*1-V*) term has to be augmented to include $(1\text{-}V)^2$ and $(1\text{-}V)^3$ components to obtain an accurate fit to the data (i.e. a cubic parabola is necessary). This model has not yet been justified in the (*M/2R, V*) plane. In this case the displacement increment directions are all parallel along any tangential load path, as observed experimentally.

Both plastic potentials necessarily have geometrically similar, inclined elliptic cross-sections, perpendicular to the *V* axis, identical to *f*, in order to preserve associated flow in such planes.

Load-paths extension technique

Contrary to the usual practice, *g* will not necessarily be either "shifted" or "scaled" to pass through the current load point. Rather, *load-paths will be extended* to the point where they intersect *g*. Calculations defining the 'normal' to *g* will then use the coordinates of this point rather than those of the load point on the yield surface (*f*). In the case of radial load paths the two processes of "radially shifting *g*" and "load-path extension to pass through *g*" will clearly produce the same result, because *g* translates along the load path towards the coordinate origin; this is not so for the tangential plastic potential. It will be shown that the new procedure enables us to deal consistently with, for example, "tangential" load paths at right angles to the *V* axis emanating from any point along it.

3.3.2 Development of the plastic potential equations

Radial load path

For '*radial*' load paths *g* takes the form of a semi-ellipse, centred on the origin (Figure 3.9).

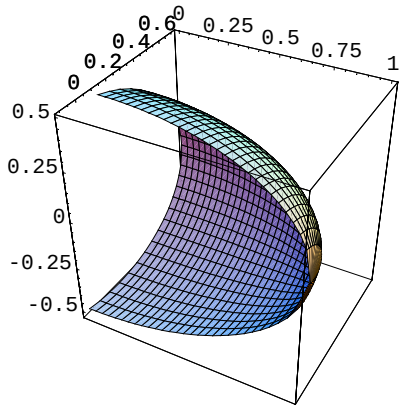

Figure 3.9. Section of the elliptic radial plastic potential (g_R).

Since we know that the (*u - w*) and ($2R\theta$ - *w*) plots obtained from radial load tests are not quite straight lines [Gottardi (1992)] we can cater for this by allowing the axis-ratio of the elliptic g (which will be defined by the parameter $\beta_h - \beta_m$) to vary as a function of *Vo/Vmax* (*f* already does so).

The equation of an 'elliptic g' would be:

$$g_R = \left(\frac{H}{\beta_h}\right)^2 + \left(\frac{M}{2\,R\,\beta_m}\right)^2 - 2\,a\,\frac{H\,M}{2\,R\,\beta_m\,\beta_h} - (V_{\max})^2 + V^2 = 0 \tag{3.22}$$

This has a form similar to that for the yield surface cigar f [Gottardi, Houlsby and Butterfield (1999)] :

$$f = \left(\frac{H}{h_o}\right)^2 + \left(\frac{M}{2\,R\,m_o}\right)^2 - 2\,a\,\frac{H\,M}{2\,R\,h_o\,m_o} - (V_{\max})^2 + V^2 = 0 \tag{3.23}$$

For all of which a=-0.22 is a well established parameter. Fortunately β changes only gradually with *Vo* and therefore it can be considered constant when taking derivatives of g with respect to *Vo*, e.g. in 'hardening' calculations.

Vmax plays a major role in the original pad-footing "model"; it now does so again as a reference datum for *g*. For this idea to be useful β will need to take the same value at points on all radial load paths which lie on the same f (i.e. each *f* will be associated with a specific g, both of them corresponding to a specific *Vo* value).

From analyses of Gottardi's Padova tests [Gottardi (1992)] using both his (*H-V*) and (*M/2R-V*) radial load-path data and a semi-elliptic form of g, we found an approximately linear relationship between β and (*Vo/Vmax*) of the form:

$$\beta = (\beta_h \text{ or } \beta_m) = n' - n''\left(\frac{V_o}{V_{\max}}\right), \text{ with } 0.45 < n' < 0.55 \text{ and } 0.14 < n'' < 0.17$$

Preliminary results for (central inclined) (*H-V*) "radial" loading (as has also been done for (vertical eccentric) (*M/2R-V*) "radial" loading) are shown in Figure 3.10.

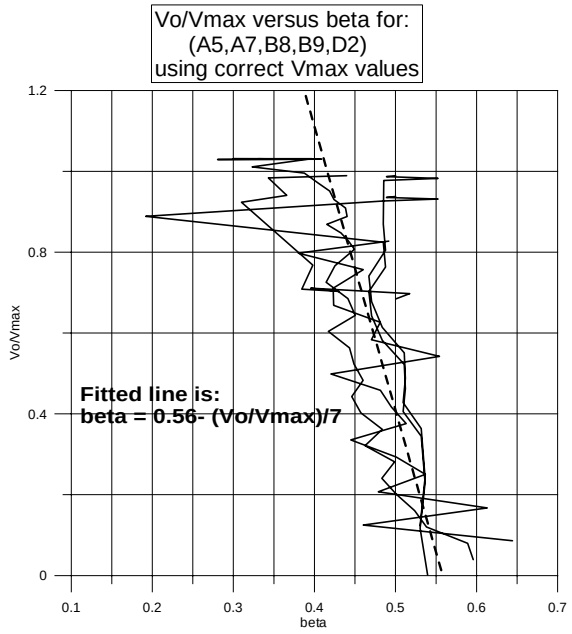

Figure 3.10. Data elaboration for tests A5, A7, B8, B9, D5.

The outcome of this investigation for the radial, central-inclined load tests (*H-V*) is to suggest that the data supports a second order linear variation of β_h with $(\frac{V_o}{V_{\max}})$ either:

$$\beta_h = 0.55 - \left(\frac{V_o}{V_{\max}}\right)\frac{1}{7} \tag{3.24}$$

For eccentric-vertical load tests (M/B-V) interpreted similarly

$$\beta_m = 0.50 - \left(\frac{V_o}{V_{\max}}\right)\frac{1}{7} \text{ or } \beta_m = 0.48 - \left(\frac{V_o}{V_{\max}}\right)\frac{1}{6.25} \tag{3.25}$$

Clearly we have not $\frac{\beta_h}{\beta_m} = \frac{h_o}{m_o} = 1.34$ other than in a very approximate sense. The value of $\frac{\beta_h}{\beta_m}$ appears to be around 1.1 to 1.2. Were this ratio to equal 1 then the g would have a circular cross-section which we do know to be incorrect. It is also known that the unavoidable mechanical restraint on free displacements in load controlled tests is more likely to reduce the value u in eccentric vertical load tests than any restraint on θ in inclined central load tests.

Therefore since the assumption that $\boxed{\frac{\beta_h}{\beta_m} = \frac{h_o}{m_o} = 1.34}$ is all of rational, elegant, convenient and reasonably valid when the scatter of the data is considered, the most convenient thing is to use this relationship to estimate β_m from β_h.

If we assume plastic flow to be 'associated' in (H - M/*2R*) planes, which is very well supported by data presented in [Gottardi, Houlsby and Butterfield (1999)] paper, then cross-sections of the '*g* cigar' will be rotated ellipses geometrically similar to those of *f*. Whence $(\beta_h/\beta_m) = (h_o/m_o) = 1.34$. Preliminary values of (β_h/β_m) suggest that this relationship can be satisfied approximately, although if β varies linearly as suggested the ratio of the two betas cannot be constant all along the V axis of the 'cigar'. The response of the model does not appear to be very sensitive to this. In fact, the results of Martin on Kaolin suggest that neither the shape nor the inclination of the elliptic *f* are constant along the length of the 'cigar'.

Tangential load path

As mentioned in Section 3.3.1, when load paths emanate orthogonally from points along the *V* axis ('*tangential*' load paths) the point at which the derivatives of *g* are to be taken is at the intersection of this load path with *g*. The basic form of *g* for such load paths is a simple *parabola* with its apex on the *V* axis located symmetrically with respect to this axis (Figure 3.11).

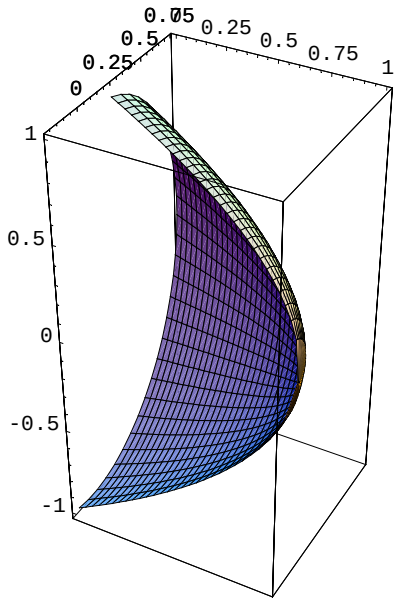

Figure 3.11. Section of parabolic tangential plastic potential (g_T).

Indeed, it is well established that, along any tangential load path the displacement increment vectors are very closely parallel until failure is approached, i.e. plots of u versus w, or $d\theta$ versus w, are straight lines. Consequently the shape of g will not vary along such a path.

The surface we want must intersect the V axis orthogonally, which it should do in order that any load increment near the failure point ($Vmax$, 0) will result in $du=0$ and $dw>>0$. This need of orthogonality requires a term in H squared. A possible general expression, for the section in the (H-V) plane, is:

$$g_H^T = \left(\frac{H}{V_{max}}\right)^2 - bb\left(1 - \frac{V}{Vmax}\right) - cc\left(1 - \frac{V}{Vmax}\right)^2 + dd\left(1 - \frac{V}{V_{max}}\right)^3 \tag{3.26}$$

Which becomes, from the best fitting with tests B6, A6, A3:

$$g_H^T = \left(\frac{H}{V_{max}}\right)^2 - 0.988381\left(1 - \frac{V}{Vmax}\right) - 0.357997\left(1 - \frac{V}{Vmax}\right)^2 + 0.476931\left(1 - \frac{V}{V_{max}}\right)^3 \tag{3.27}$$

The corresponding expression in the ($M/2R$-V) plane is:

$$g_M^T = \frac{3}{4}\left(\left(\frac{M}{V_{max}}\right)^2 - 0.988381\left(1 - \frac{V}{Vmax}\right) - 0.357997\left(1 - \frac{V}{Vmax}\right)^2 + 0.476931\left(1 - \frac{V}{V_{max}}\right)^3\right) \tag{3.28}$$

Multi load paths

A question now arises as to how load increments can be incorporated which do not simply extend either of these paths. There is important experimental data pertinent to this question in Gottardi's PhD thesis [Gottardi (1992)] which demonstrates that if, after following an arbitrary load path, a load increment parallel to the H axis is applied, the resulting displacement increment direction is approximately that predicted by the g relevant to such a path, and similarly for radial increments in (H -V) and ($M/2R$ - V) planes.

This leads to the conclusion that any general load increment, from a particular load point, in the (H-V) plane for example, might be considered as having two components: one along the radial direction through the point and the other in a tangential plane these then being added together [Butterfield (1981)]. In essence this uses the radial and tangential directions as skew coordinates and assumes that superposition of the results from the two 'mechanisms' will be valid. Note that in 3D the radial coordinate lines will lie on a cone and tangential ones in V= constant planes.

A validation of both plastic potential equations and superimposition of radial and tangential load paths has been demonstrated by reproducing some of Gottardi (1992) multi-load path results, as shown in the general load-paths sub-section of Section 3.3.3.

Some relevant algebra and geometry

In order to derive the β versus Vo relationship for radial load paths we need to do the following for each load point from every such test:

- determine Vo, from the known expression for f (equation 3.3)

$f = X - \{4\,V(1 - V/Vo)\}^2 = 0$

where:

$X = (H/h_o)^2 + (M/(B\,m_o))^2 - 2a\left(\frac{HM}{B\,m_o\,h_o}\right)$

which provides:

$$Vo = \{4\,V^2/(4\,V - X^{0.5})\} \tag{3.29}$$

The '*g*' equation provides the plastic displacement increment ratio. This is measured in the experiments for radial (*H*-*V*) loading

$$(du/dw) = (\partial g/\partial V)/(\partial g/\partial H) = V\,(\beta_H)^2/(H - a\,Mr/2\,R)$$
$$\text{where } r = \beta_H/\beta_{HM} \tag{3.30}$$

For radial load tests in the (*M/2R* - *V*) plane, with *H* formally zero, the equivalent expression is:

$$(dw/2\,R\,d\theta) = (\partial g/\partial V)/(\partial g/\partial M/B) = V\,(\beta_M)^2/(M/2\,R - a\,H/r) \tag{3.31}$$

In both cases the test data can be used to plot β_M against (V_o/V_{max}) to determine the 'unique' relationships between them (see Figure 3.10).

Corresponding calculations for a 'tangential (*H*-*V*)' test can be performed.

3.3.3 Comparison between observed and predicted displacements

In order to investigate the predictive capabilities of the new suggested formulations of the plastic potential and modified hardening law, a number of experimental tests were chosen for numerical simulation. The tests reproduced come from to the experimental work carried out by Gottardi in Padova [Gottardi (1992)] (Table 3.2). The reference model used for numerical simulations is based on the following equations:

■ **Yield function** [Gottardi, Houlsby and Butterfield (1999)]

$$f = \left(\frac{M}{m_o\,2\,R}\right)^2 + \left(\frac{H}{h_o}\right)^2 - 2\,a\,\frac{M\,H}{2\,R\,m_o\,h_o} - \left(4\,V\left(1 - \frac{V}{V_o}\right)\right)^2$$
$$\text{with: } a = -0.2225,\ mo = 0.090,\ ho = 0.1213 \tag{3.32}$$

■ **Radial Plastic potential**

$$g_R = \left(\frac{M}{\beta_m\,2\,R}\right)^2 + \left(\frac{H}{\beta_h}\right)^2 - 2\,a\,\frac{M\,H}{2\,R\,\beta_m\,\beta_h} - V_{max}{}^2 + V^2$$
$$\text{with: } \beta_h = 0.55 - \left(\frac{V_o}{V_{max}}\right)\frac{1}{7},\ \frac{\beta_h}{\beta_m} = \frac{h_o}{m_o} \simeq 1,34 \tag{3.33}$$

■ **Tangential Plastic potential**

$$g_H^T = \left(\frac{H}{V_{max}}\right)^2 - 0.988381\left(1 - \frac{V}{Vmax}\right) -$$
$$0.357997\left(1 - \frac{V}{Vmax}\right)^2 + 0.476931\left(1 - \frac{V}{V_{max}}\right)^3 \tag{3.34}$$

$$g_M^T = \frac{3}{4}\left(\left(\frac{\mathrm{M}}{V_{\max}}\right)^2 - 0.988381\left(1 - \frac{\mathrm{V}}{Vmax}\right) - 0.357997\left(1 - \frac{V}{Vmax}\right)^2 + 0.476931\left(1 - \frac{\mathrm{V}}{\mathrm{V}_{\max}}\right)^3\right) \tag{3.35}$$

■ **Hardening law** (Figure 3.12)

$$V_o = V_{\max}\left(1.38131\left(\frac{w_p}{w_{p,max}}\right) - 0.30651\left(\frac{w_p}{w_{p,max}}\right)^2 + 0.279123\left(\frac{w_p}{w_{p,max}}\right)^3 - 0.353923\left(\frac{w_p}{w_{p,max}}\right)^4\right) \tag{3.36}$$

This empirical polynomial formula defines the form of the strain hardening equation, where w_p is the plastic embedment. Since it has been fitted to the vertical central load-penetration curve for the specific conditions of tests performed by Gottardi (1992) this particular equation may not be applicable in other situations.

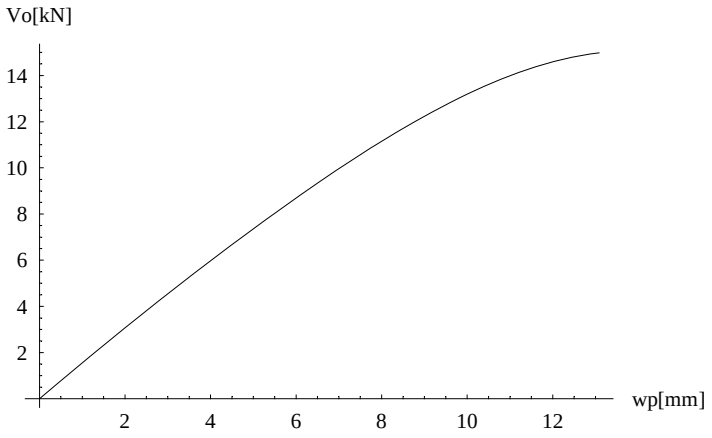

Figure 3.12. Hardening law plot

■ **Scaled Hardening law**

$$w_{p,mod} = w_p \cdot \left[1 - s\left(1 - \frac{V}{V_o[w_p]}\right)\right] \tag{3.37}$$

The scaling of the hardening law has been discussed in Section 3.2.

■ **Parameters**

The parameters involved and their meaning are the following:

a=-0.2225: inclined ellipse parameter [Gottardi, Houlsby and Butterfield (1999)];

m_o *=0.090*: length of the minor semiax of the elliptical section in the M-H plane [Gottardi, Houlsby and Butterfield (1999)];

h_o *=0.1213*: length of the major semiax of the elliptical section in the M-H plane [Gottardi, Houlsby and Butterfield (1999)];

2R: foundation width [Gottardi (1992)];
V_{max}: maximum vertical centred load (calculated from relative density D_R, of the sand bad) [Gottardi (1992)];

Due to the intrinsic error in test data, which is more significant at low levels of load and displacement, the initial value of the displacements in the data do not correspond to the value calculated in the simulation. There are two possible way of solving the problem: the first is to translate data in order to fit the initial vertical displacement under centred vertical load, the second is to change V_{max} in order to find the initial vertical displacement directly from the hardening law. Since the initial stiffness of the data is much less correct than the defined value of the bearing capacity and since the second procedure gives very low values of the V_{max}, the first possibility has been chosen, and the value of V_{max} used has been the one calculated from D_R and reported in [Gottardi (1992)].

In the following sections some examples of predictions of tests from Table 3.2 are reported. Note that the radial and tangential load path tests were also used to calibrate the plastic potential equations, therefore the general load paths establish the most important validation of the model. The model implementation has been realized using *'Mathematica 5.0'*. The procedure which generates the numerical solution is detailed and discussed in the Appendix to the Thesis.

Radial load path

- **Test A4, H-V plane**

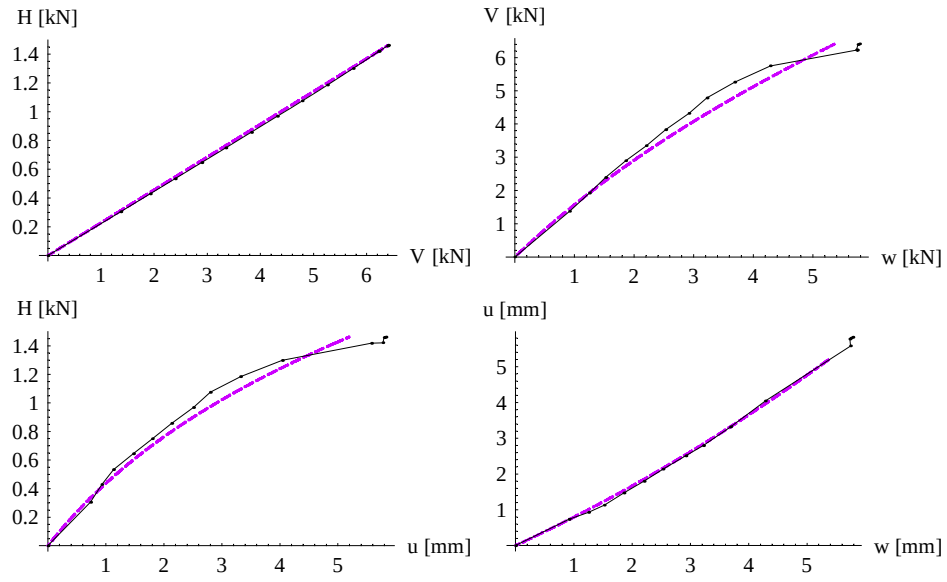

Figure 3.13. Load path and displacements for test A4.

- **Test A7, H-V plane**

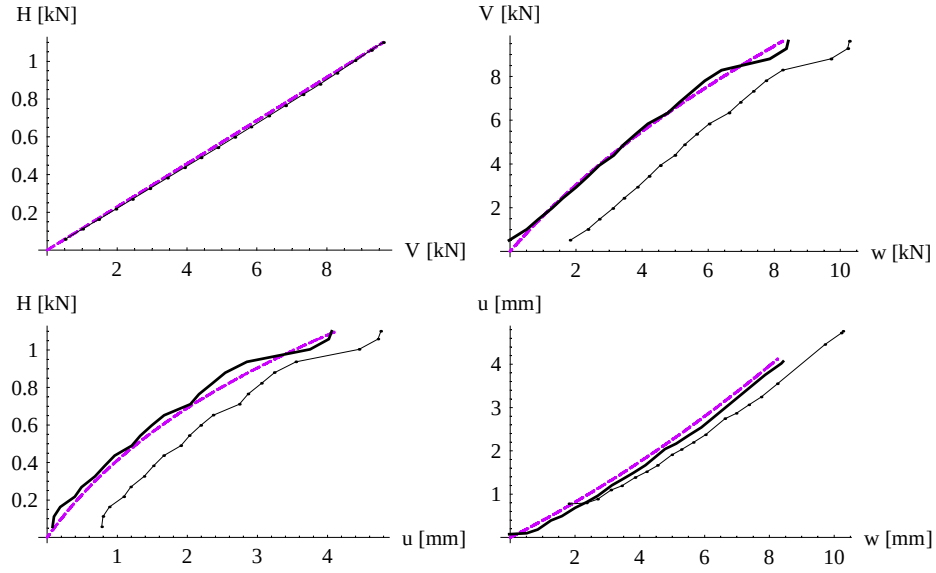

Figure 3.14. Load path and displacements for test A7.

- **Test B8, H-V plane**

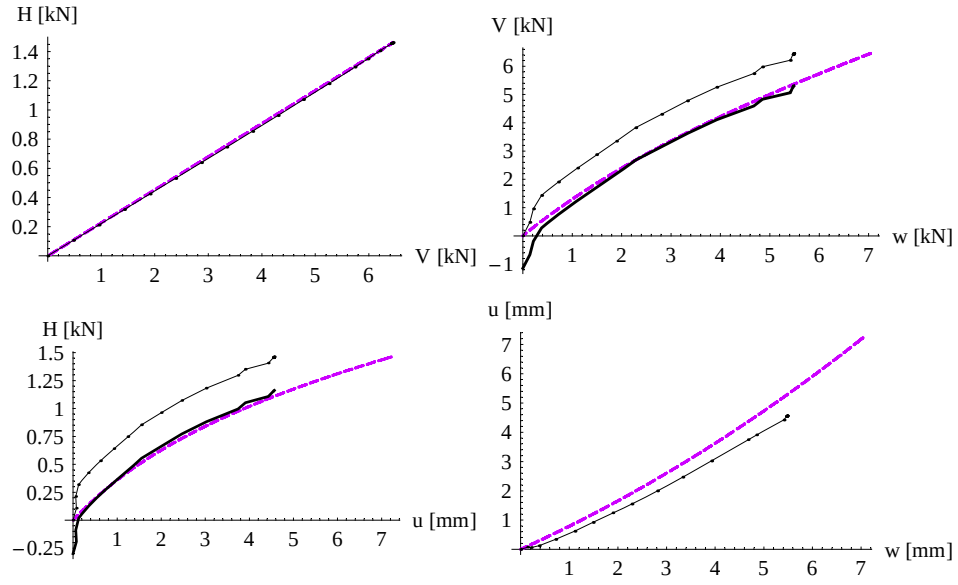

Figure 3.15. Load path and displacements for test B8.

- **Test B9, H-V plane**

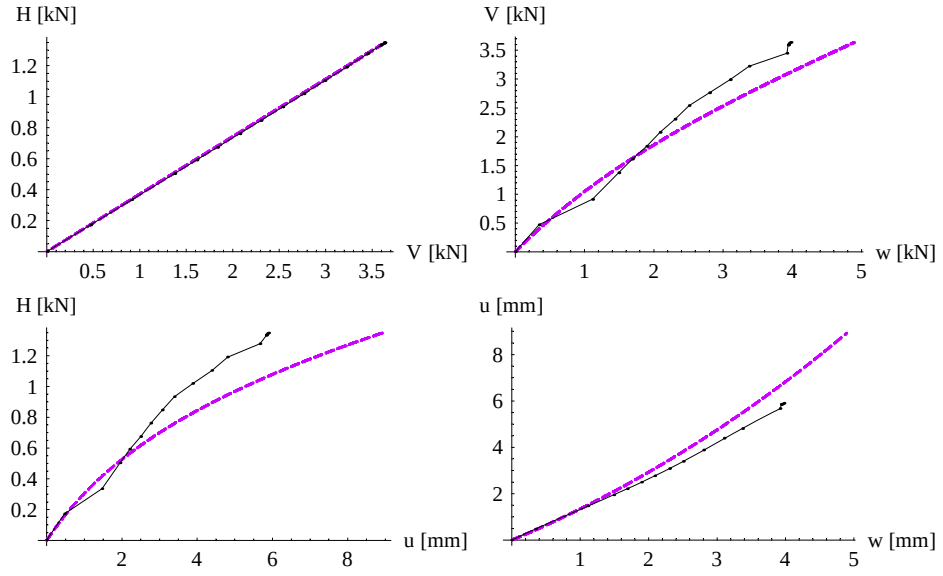

Figure 3.16. Load path and displacements for test B9.

- **Test D2, H-V plane**

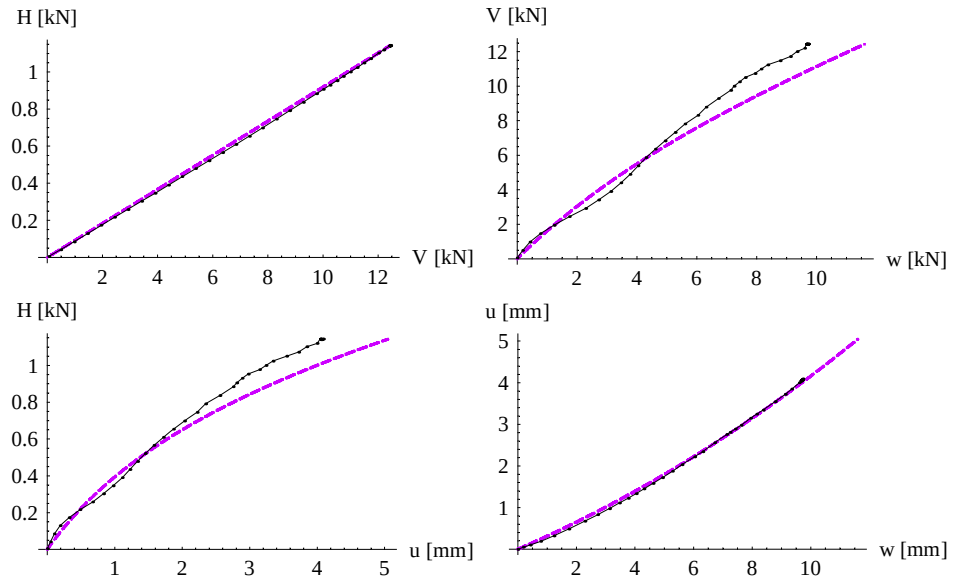

Figure 3.17. Load path and displacements for test D2.

Tangential load path

- **Test A3, H-V plane**

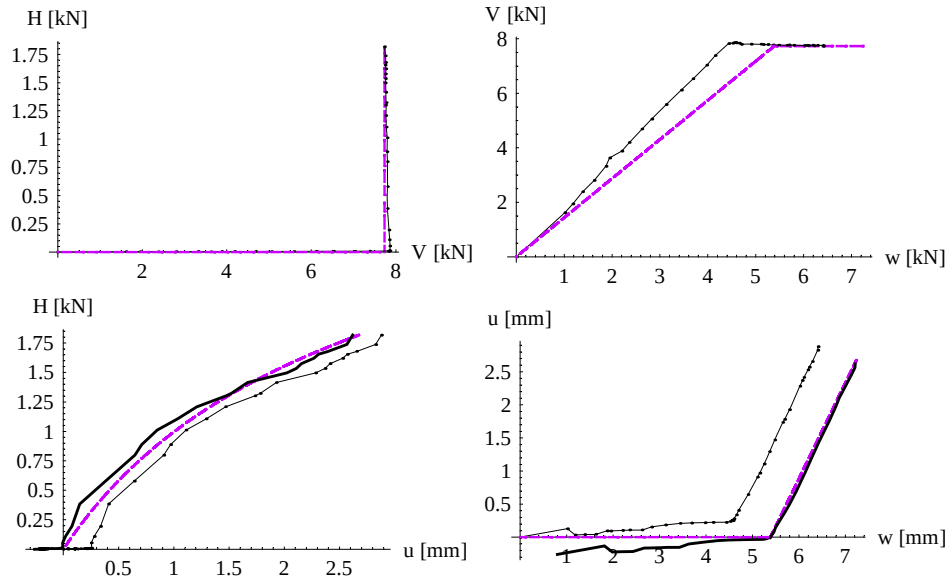

Figure 3.18. Load path and displacements for test A3.

- **Test A6, H-V plane**

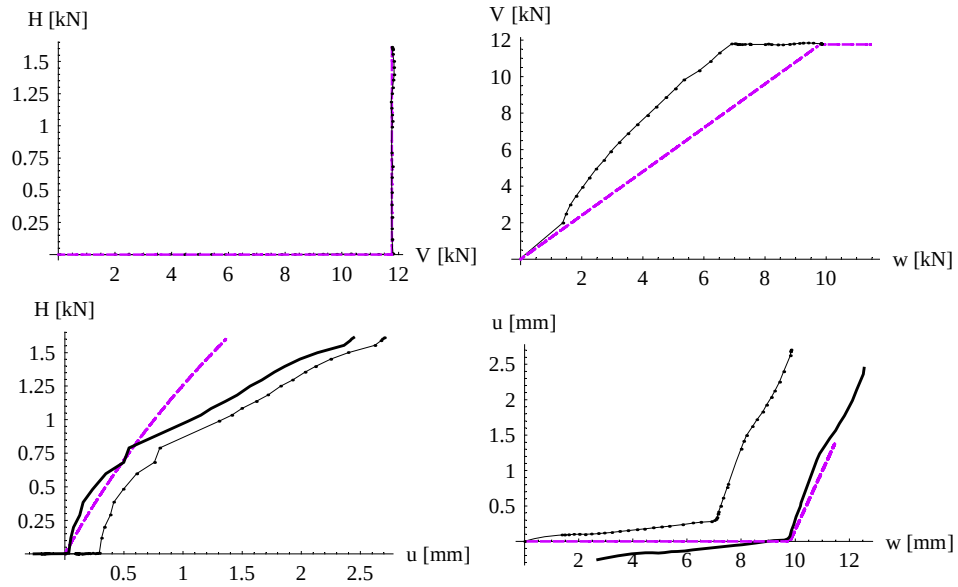

Figure 3.19. Load path and displacements for test A6.

General load path

- **Test D1, H-V plane**

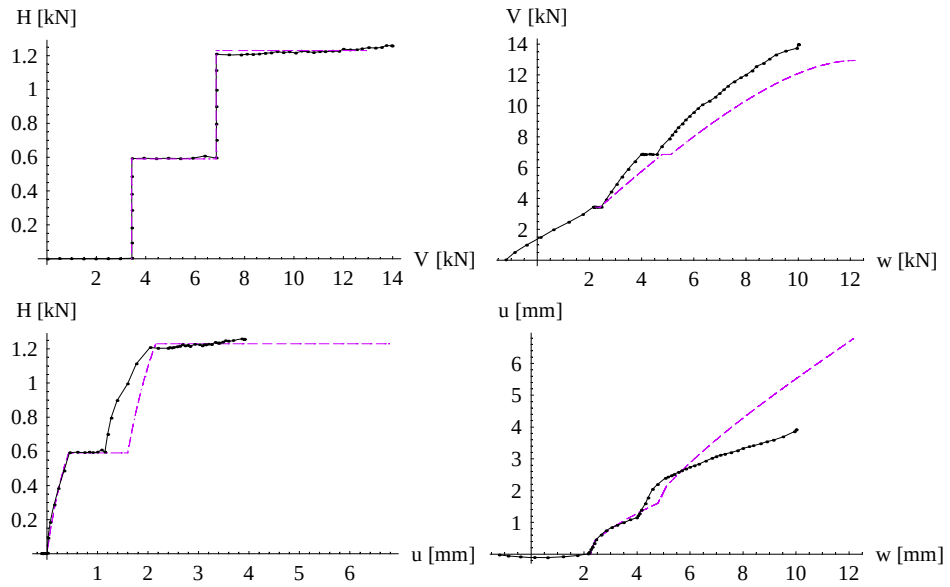

Figure 3.20. Load path and displacements for test D1.

- **Test D3, H-V plane**

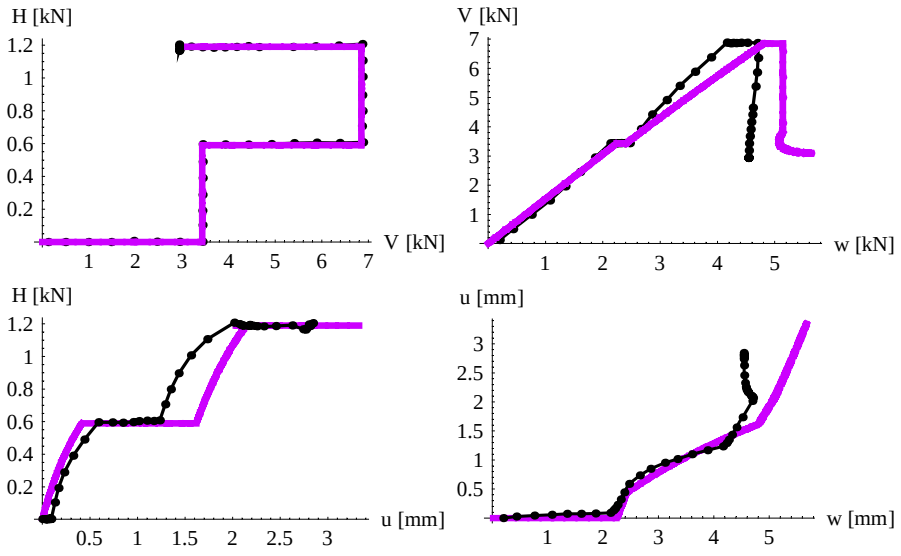

Figure 3.21. Load path and displacements for test D3.

3.4 From the V-w to the M-θ curve

The equations indicated in Section 2 for the plastic potential and yield function associated to the hardening law proposed in Section 1, provide a complete plasticity model for a surface pad. The output of models of this type gives important informations in terms of both stiffness and strength of the foundation. The aim of this section is to show how the model can be effectively applied to derive the rotational stiffness (i.e. the M-θ curve) of foundations, starting from an input of parameters that define only the vertical stiffness of the system (i.e. the hardening law of the model). Indeed, one of the main objectives of the work has been the achievement of a reliable M-θ curve, necessary to develop the stability of equilibrium analysis of towers. The stability problem is further investigated in Chapter 4.

The relevant load components in the specific case of leaning towers, in static conditions (i. e. no seismic actions are considered), are M and V, consequently the simplified reference equations of the model become,

- *Yield function* [Gottardi, Houlsby and Butterfield (1999)]

$$f = \left(\frac{M}{m_o\, 2R}\right)^2 + -\left(4V\left(1 - \frac{V}{V_o}\right)\right)^2 \quad \text{with: } a = -0.2225,\ mo = 0.090 \tag{3.38}$$

- *Tangential Plastic Potential*

$$g_{\mathrm{MT}} = \frac{3}{4}\left[\left(\frac{M}{2R\,\mathrm{Vmax}}\right)^2 - 0.988381\left(1 - \frac{V}{\mathrm{Vmax}}\right) - 0.357997\left(1 - \frac{V}{\mathrm{Vmax}}\right)^2 + 0.476931\left(1 - \frac{V}{\mathrm{Vmax}}\right)^3\right. \tag{3.39}$$

- *Hardening Law*

$$V_0 = A(1 - e^{-B\mathrm{w}}) \quad \text{with } A \text{ and } B \text{ fitted on the numerical solution described in Section 3.1.} \tag{3.40}$$

- *Scaled Hardening law*

$$w_{p,\mathrm{mod}} = w_p \cdot \left[1 - s\left(1 - \frac{V}{V_o[w_p]}\right)\right] \quad \text{with } s = 0.9 \tag{3.41}$$

The input parameters required for the definition of the hardening law are:
- $2R$: foundation width (equivalent diameter);
- γ': soil's unit weight [kN/m^3];
- C_0': slope of the virgin compression curve;

- $C_r^{'}$: slope of the reloading curve;
- *OCR*: overconsolidation ratio;
- *n*: overconsolidation ratio measured at a known depth;

In addition to $2R$ and γ', already introduced for the hardening law, more parameters are necessary to complete the model definition. In particular all parameters that allow for the calculation of $V_{\max}$ (maximum vertical centred load). Applying a traditional bearing capacity analysis (Section 2.1.1) required parameters are

- φ': angle of friction of the subsoil (uniform layer) [°];
- *d*: foundation embedment [*m*];
- *L*: length of the foundation ($L>2R$) [*m*];
- h_{ow}: depth of the water level (from the soil level) [*m*];

The whole model has been applied to and solved for the Pisa Tower and the Santo Stefano bell tower. Both development are presented in Chapter 5, each one inside a particular '*Mathematica Notebook'*, developed *ad hoc.*

Note that the model requires only simple parameters for the development of a reliable M-θ curve. The parameters are obviously tangible and have both a clear physical meaning and a simple definition. This is one of the most important achievements of the analysis.

3.5 Creep in strain hardening models for surface pads

The objective of the methodology is to incorporates a creep process (using the model developed by Bjerrum in the 7th Rankine Lecture [Bjerrum (1967)]) within the foregoing model, in order to obtain a useful and realistic representation of the response of campanile over time.

The key items in this section are:

1) a very simple creep model for V=W=constant loading (Section 3.5.1)
2) the extension to M=variable loading (Section 3.5.2)
3) the definition of creep rates (Section 3.5.3)

3.5.1 Vertical creep process under constant V

Usually the time taken to apply loads (e.g. to apply *W* during construction) will be very short compared with creep time scales of practical interest and therefore loads may be taken to be applied instantaneously producing an instantaneous settlement δw. All the following relates to creep under constant *V*:

$V(t)=V(t=0)= W$

The influence of delayed settlements (at $t>0$) under constant load can be introduced using an idea in Bjerrum's (1967) 7th Rankine Lecture. He makes an essential, very attractive assumption that the change in void ratio developed in creep (from e_o to e_0', say, under constant p_0') is entirely equivalent to the same (e_0', p_0') point having been arrived at by a virgin-loading-unloading process (Figure 3.21). It will be assumed that this argument holds in our model in relation to w_o becoming w_0' by creep under V_o = constant.

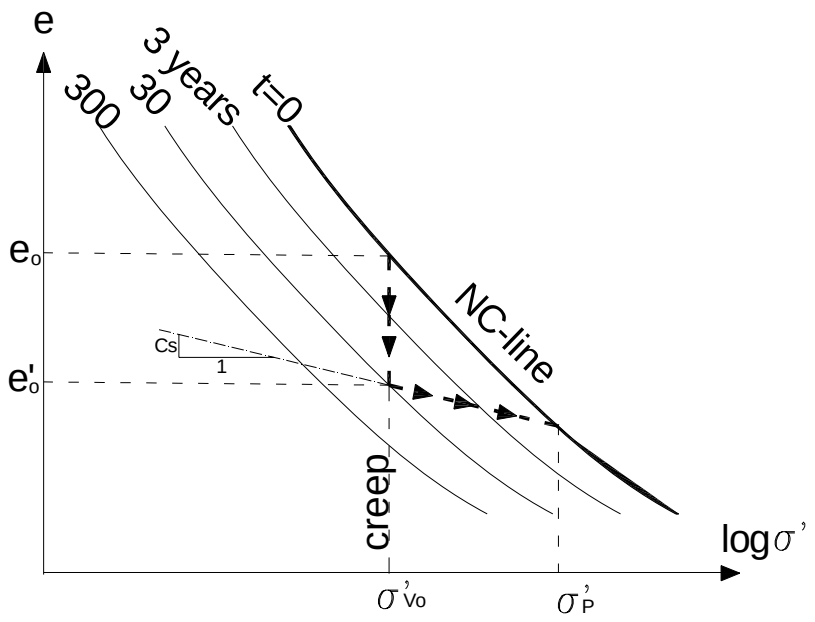

Figure 3.22. Idea in Bjerrum's (1967) 7th Rankine Lecture

Consider firstly the vertical w-creep process under constant V (because we are more familiar with it). All the following relates to Figure 3.23.

If $\xi_w(t)$ is a vertical creep function defined such that, at time t after a displacement w_0, and under constant applied loading, the displacement is

$$w(t) = w_0 (1 + \xi_w (t)) \tag{3.42}$$

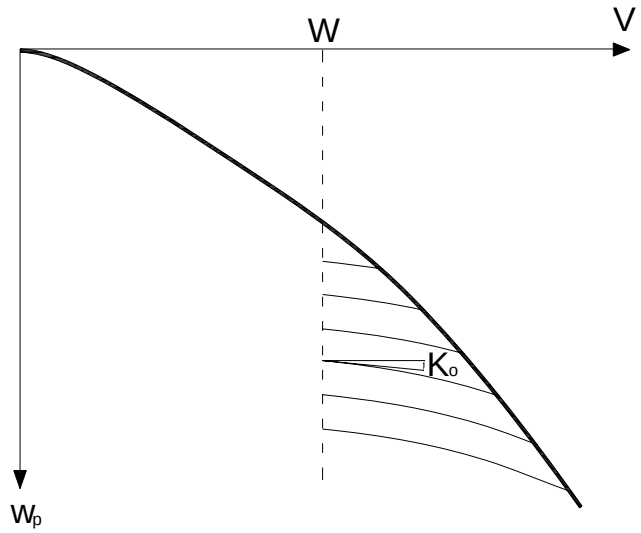

Figure 3.23. Vertical creep hardening

The changes that occur in (V,w) over a time increment Δt applied at time t during which V is constant, have the effect of a '*precompression*'. The 'reloading' vertical stiffness $K_{rv} \approx$Ko must be apply to load increments following a creep period, until the original vertical centreline load versus vertical displacement (Vo, w^p) at t=0 is reached again (Figure 3.23). Note that a constant value of K will be precise enough for our purpose although the model can easily be extended to incorporate a curve reloading path using the methodology in Section 3.1.

3.5.2 Rotational creep process

All the previous analysis can be transferred to rotational creep, but, unlike the vertical creep hardening case, in which the vertical load remains constant, the increase of rotation due to creep generates an increment of external moment acting on the foundation ($\Delta M_e = W \cdot h \cdot \Delta\theta_{creep}$). Consequently, the load state is not constant but increases with the rotational creep:

$M(t)=M(t=0)+W \cdot h \cdot \Delta\theta_{creep}$

All the following relates to Figure 3.24. Each pair of values (M_e, $\theta(t)$) must lie on the external moment line (with slope Wh).

If $\xi_\theta(t)$ is a rotational creep function defined, such that, at time t after a rotation θ_0, the rotation is:

$$\theta(t) = \theta_0 (1 + \xi_\theta (t)) \tag{3.43}$$

Every point on the external moment line will be a point from which a section of a creep-hardened (M-θ) is to be drawn (Figure 3.24). The 'reloading' rotational stiffness will be bigger than the initial until the original (M-θ) curve at t=0 is reached again (Figure 3.24).

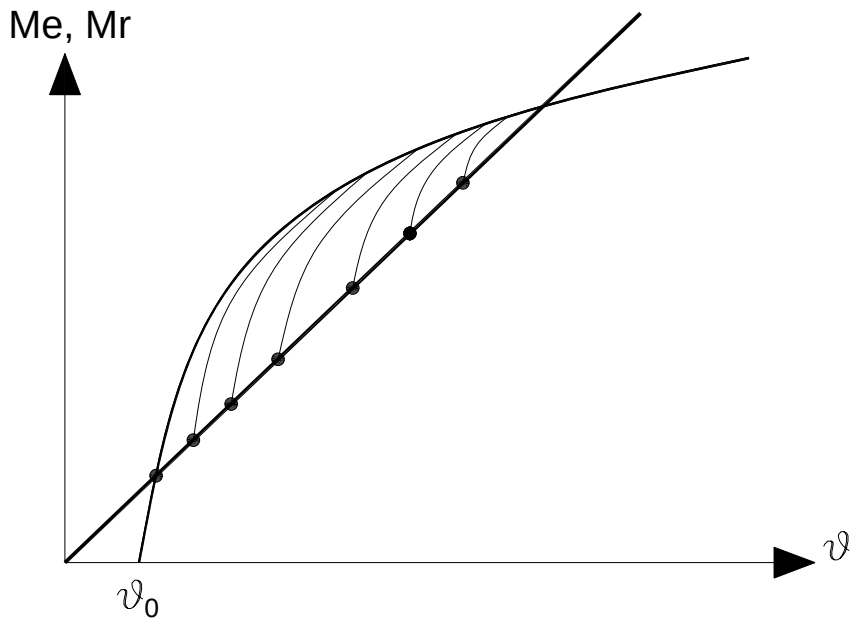

Figure 3.24. Rotational creep hardening

3.5.3 Creep rates

It is worth noting that the creep rates will increase as any load combination approaches a 'bearing capacity' failure state. In this view any bearing capacity failure is, in fact, a state at which the creep rate becomes infinite. A simple way of achieving this for vertical creep, could be (for a constant vertical load *W*) to define

$$R = \frac{W}{V_{\max}} \tag{3.44}$$

and introduce R in Equation 3.42

$$\frac{w(t)}{w(t=0)} = \frac{w}{w_0} = 1 + \xi_w(t)\,\frac{R}{1-R} \tag{3.45}$$

$\frac{R}{1-R}$ being a function that becomes infinite, quite abruptly, as R approaches 1, in addition for R = 0 , $\frac{w}{w_0} = 1$; R = 1 , $\frac{w}{w_0} = \infty$; R = 1/2 , $\frac{w}{w_0} = (1 + \xi)$, all of which are reasonable.

A creep rate can be introduced similarly into the rotational creep process. As the external moment ($M=Wh\ \theta$) increases due to rotational creep then, again, according to Equation 3.45, this rate needs to become infinite when the moment load path intersects the parabolic failure envelope at $M = Wh\theta_f = M_f$, say, where θ_f is the inclination of the tower at the onset of bearing capacity failure and

$$\frac{M_f}{2R} = 4\,mmoR\,(1-R)\,V_{\max} \tag{3.46}$$

If we further assume (being probably the simplest plausible assumption) that $\xi_w(t)$ is applicable to all creep processes:

$$\xi_w(t) = \xi_\theta(t) = \xi(t) \tag{3.47}$$

we can then write, analogously to equation Equation 3.45 (with r = M(t)/M$_f$ = M/M$_f$ = (θ/θ_f), r is not constant and N an unknown, arbitrary, dimensionless multiplier),

$$\frac{\theta}{\theta_0} = N\,\frac{w}{w_0}\left(1+\frac{r}{1-r}\right) = N\,\frac{w}{w_0}\,\frac{1}{1-r} = N\,\frac{w}{w_0}\,\frac{\theta_f}{\theta_f-\theta} \tag{3.48}$$

The calibration and validation of such a model would have to be done using field data. Unfortunately only very frugal campanile-creep data exist.

In fact the model provides a reasonable fit to the available Pisa tower creep data using R = 0.5; N = 4÷3; w_o = 1÷1.3 m; θ_o = 1÷1.5°.

The implications of a such an analysis for the stability of equilibrium of towers is discussed in Chapter 4.

CHAPTER 4

A contribution to stability analysis of towers

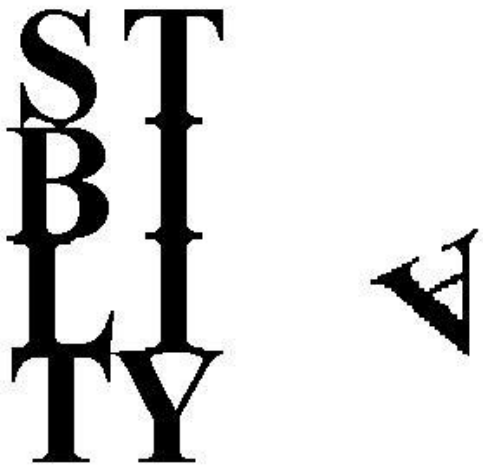

Figure 4.1. Minimalist concrete poetry, “Stability”. Clamente Padin

"Imagination is more important than knowledge"
Albert Einstein

Introduction

—In this chapter a comprehensive analytical tool is introduced that can deal with the two major collapse mechanisms of towers foundations, bearing capacity failure, due to lack of soil strength, and instability of equilibrium, due to lack of soil stiffness. Both of these problems, are tackled using a work-hardening plasticity model for surface footings. Such an analysis provides not only a complete framework within which both possible collapse mechanisms can be assessed but also a prediction of which of them is most likely to occur. The analysis will be developed in the form of a Mathematica notebook in the following chapter (Chapter 5) in relation to two case histories: Pisa Tower and Santo Stefano bell tower.

4.1 Stability of equilibrium of towers via strain hardening plastic soil models

4.1.1 Problem setting up & definition of stability

The instability of equilibrium of towers has been, up to now, theoretically treated in different ways, which differ substantially from the model adopted herein to describe the connection between soil and structure. Different analyses have been carried out by Hambly (1985), Cheney *et al.* (1991), Lancellotta (1993), Desideri & Viggiani (1994), Como (1994); see Section 2.2.4, in Chapter 2 for details.

In a stability of equilibrium analysis the tower is modelled as rigid bar, resting on a support in which the deformability of the system is concentrated (Figure 4.2).

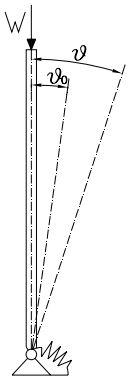

Figure 4.2. Rigid bar column

The equilibrium condition for the reference column in Figure 4.2 imposes an external (i.e. overturning) moment (*Me*) equal to the reaction of the restrain ($Mr=f(\theta-\theta_0)$), hence

$$M_e = M_r \Rightarrow W\, h \sin\theta = M_r(\theta - \theta_0) \tag{4.1}$$

Note that h is the height of the centre of gravity of the structure above its base, θ is the total rotation of the tower from the vertical position and θ_0 an initial imperfection of the system. Assuming for small rotation $\sin\theta \simeq \theta$, an assumption clearly acceptable in the case of a tower, for which 10° is already a very high inclination, the equilibrium condition becomes:

$$\boxed{Wh\vartheta = \mathrm{M_r}\,(\vartheta - \vartheta_0)} \tag{4.2}$$

The initial tilting θ_0 could be due to either eccentricity of the tower on its base or an initial inclination developed during construction; it is impossible to define a precise value of θ_0, but it must be considered very small and present in all real cases. This initial imperfection is not associated with the resisting moment (i. e. the rotational stiffness of the foundation), since the M_r curve is a function of the absolute rotation ($\Delta\theta=\theta-\theta_0$) of the tower.

The stability analysis can be directly conducted using the graphical solution suggested for the first time by Cheney in 1991. The relevant plane is the M-θ, where M_e and M_r can be simultaneously plotted, and, in particular, M_e is a line with (Wh) slope, and M_r a curve (Figure 4.3, *a)*).

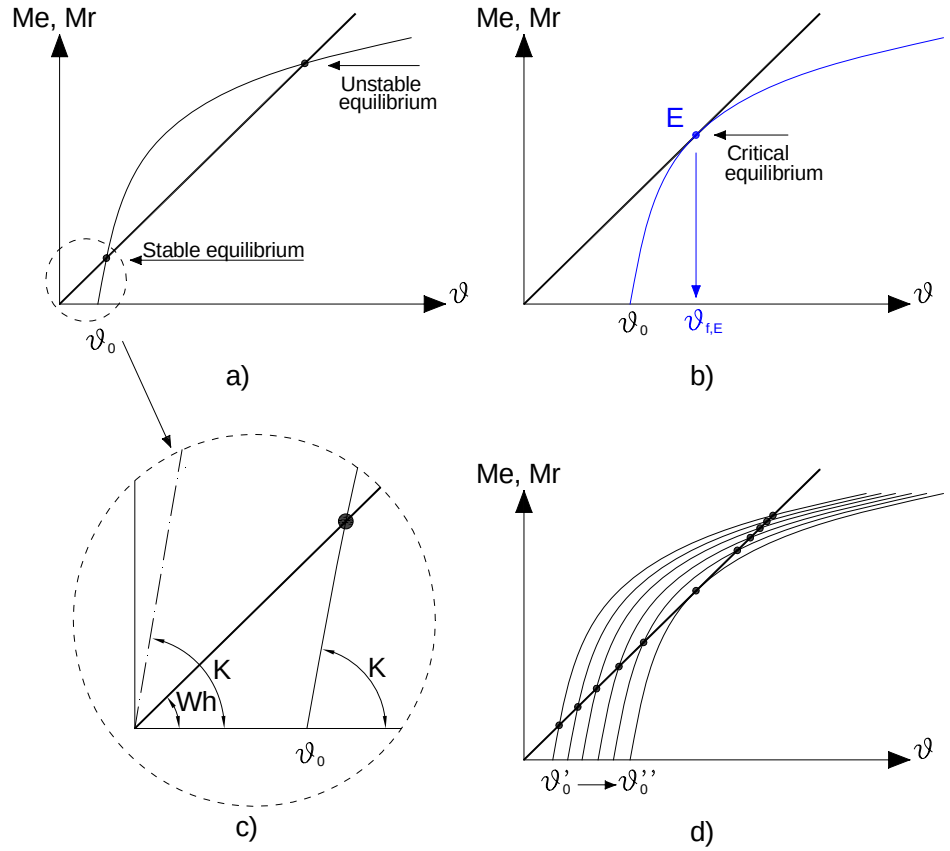

Figure 4.3. Analysis of stability in the M-θ plane: "*stability analysis of a leaning tower*". a) Stable and unstable equilibrium condition. b) Critical equilibrium condition. c) Detail of the relation between the external moment slope (Wh) and the initial rotational stiffness of the foundation (K). d) Translation of the M-θ curve due to creep.

If the initial slope of the M_r curve (K) is equal to or greater than the slope (Wh) of the external moment load path M_e, then M_e and M_r never intersect and equilibrium is impossible from the beginning of the construction of the tower (Figure 4.3, *c)*). On the contrary, if $K < Wh$,

then, for a given small θ_0, equilibrium can occur at two points on the M_r curve (Figure 4.3, *a)*), depending upon loading history

- *Stable equilibrium:* $\frac{dM_r}{d\theta} > \frac{dM_e}{d\theta}$

  for small increase in θ, M_r increases faster than M_e.
- *Unstable equilibrium:* $\frac{dM_r}{d\theta} < \frac{dM_e}{d\theta}$

  for small increase in θ, M_r increases slower than M_e.

The maximum value of M_e, that can be resisted, occurs when the M_e line is tangent to the M_r curve; the coordinates of the tangent point then define the critical condition for instability of equilibrium (point E, Figure 4.3, *b)*)

- *Critical equilibrium*

  $\frac{dM_r}{d\theta} = \frac{dM_e}{d\theta}$

Any situation in which M_e does not intersect M_r has no physical meaning.

Figure 4.3 *a)* could be interpreted as the picture of the condition of a tower at a specific, static, instant. In practice, due to the viscous behaviour of the soil, additional creep rotations will occur. The model can allow for progressive tilting, as Cheney et al. (1991) and Lancellotta (1993) suggested, considering them in the same way as initial rotation, therefore θ_0 will include not only the initial imperfection of the system ($\theta_{0\,\mathrm{ini}}$), but also any additional rotations due to creep ($\theta_{0\,\mathrm{creep}}$)

$$\theta_0 = \theta_{0\,\mathrm{ini}} + \theta_{0\,\mathrm{creep}} \tag{4.3}$$

It is important to note that the shape of the moment-rotation curve is not affected by creep deformations, it merely translates along the positive θ-axis (Figure 4.3, *d)* shows translation of the M-θ curve from $\theta_0' = \theta_{0\,\mathrm{ini}} + \theta'_{0\,\mathrm{creep}}$ to $\theta_0'' = \theta_{0\,\mathrm{ini}} + \theta''_{0\,\mathrm{creep}}$). Therefore the effect of creep is to reduce the factor of safety with respect to the critical initial angle θ_0.

However, the difficulty of defining the rotational stiffness ($dM_r(\theta)/d\theta$) of the soil foundation system must not be forgotten. This is the problem confronted in Section 4.1.2 via plasticity models.

4.1.2 Coupling of work hardening plasticity models with instability of equilibrium analysis for towers

Hambly in 1985 and again Cheney *et al.* in 1991, pointed out the importance of the knowledge of the rotational stiffness of the soil foundation system in the development of a proper stability of equilibrium analysis: the first author suggested using numerical codes, the second used experimental determinations (centrifuge tests). In this section the problem is solved by applying a work-hardening plasticity model for surface pads at the foundational level of the structure (sketch in Figure 4.4), as suggested in the past by Desideri & Viggiani (1994) and Como (1994).

The analysis has been developed in this Thesis for the Pisa Tower and for Santo Stefano bell tower, which are completely reported in Chapter 5. In both cases the complete analytical model proposed in Chapter 3 has been used to define the M-θ curves for the two systems, then the analysis has been performed following procedure described in the previous section.

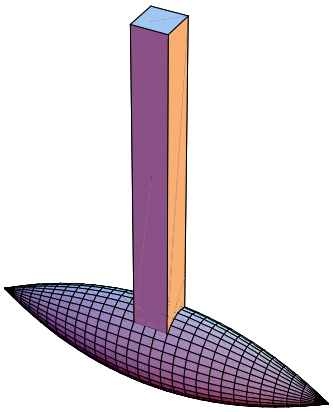

Figure 4.4. Rigid model tower on a work hardening plasticity model.

As previously pointed out in Chapter 3, Section 3.4, the model needs very simple parameter in input:

- $2R$: foundation width (equivalent diameter);
- γ': soil unit weight [kN/m^3];
- C_0': slope of the virgin compression curve;
- C_r': slope of the reloading curve;
- OCR: overconsolidation ratio;
- n: overconsolidation ratio measured at a known depth;
- φ': angle of friction of the subsoil (uniform layer) [°];
- d: foundation embedment [m];
- L: length of the foundation ($L>2R$) [m];
- h_{ow}: depth of the water level (from the soil level) [m];

Then the significant *load path* for the tower must be imposed: i. e. the application of the vertical weight (W) of the tower and then the increase of moment due to tower rotation at constant vertical load. The integration of the model (see the Appendix for details) produced a numerical solution which could be interpolated with the augmented exponential function of Equation 4.4:

$$\boxed{M_r(\vartheta - \vartheta o) = p\,[1 - e^{-(q-r)(\vartheta-\vartheta o)}] + p\ r\ (\vartheta - \vartheta o)} \tag{4.4}$$

As an example the M-θ curve fortThe Pisa Tower is shown in Figure 4.5.

Note that this curve is load path dependent, consequently it can not be associated with a load path different from the one already described. In addition it must be pointed out that the shape of the curve is very closed to the output of experimental tests (centrifuge tests in Figure 2.33, in Chapter 2, from Cheney, 1991), which, in general, show progressive reduction of stiffness with increasing rotation and a residual stiffness of the foundation at large rotations.

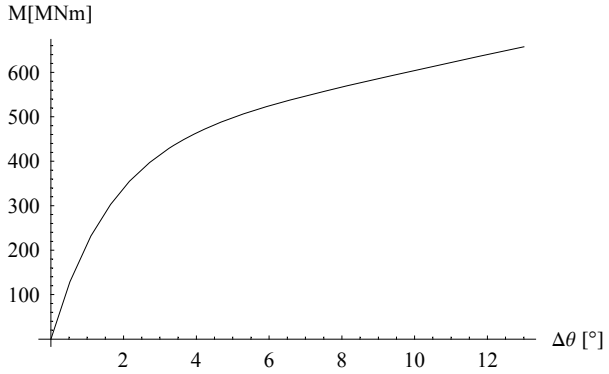

Figure 4.5. Example of (M-θ) curve, developed for the Pisa Tower via the plasticity model.

This curve can be compared (Figure 4.6) with the rotational stiffness suggested by Lancellotta in 1993 for the non-linear rotational spring (thick line). In that case the M_r was an exponential function (Section 2.2.4, Chapter 2), depending on the initial stiffness and the ultimate moment capacity of the structure. Lancellotta had no theoretically supported for his curve, but he did a an approximate empirical estimation of it. These curves differ not only in shape, but also by the major difference in the methodology used to generate them. Nevertheless, they are generally very similar.

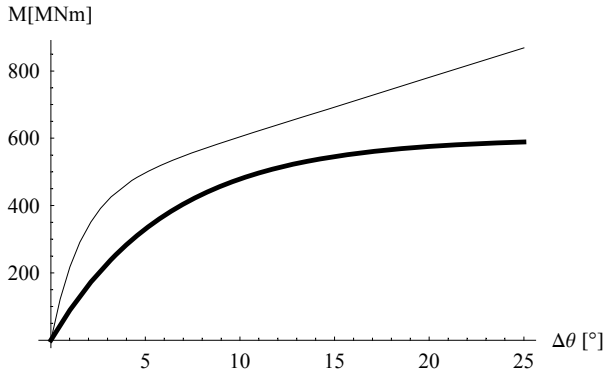

Figure 4.6. Comparison between the Pisa Tower (M-θ) curve by Lancellotta (1993), thick line, and the one from the plastic model, thin line.

Figure 4.7 shows the example of the stability analysis of the Pisa Tower in the M-θ plane, developed using the strain hardening plastic model (see Chapter 5 for details and discussion). The value of initial rotation, θ_0 (that incorporates all historic creep deformations), necessary to establish the position of the curve in the plane, can be assessed from the current value of rotation. In this way the problem of defining $\theta_{0\,\mathrm{ini}}$ has been overcome.

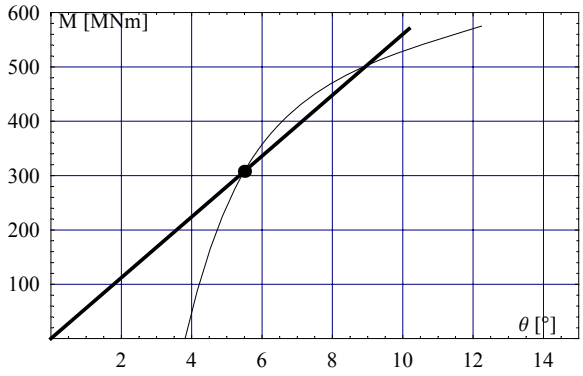

Figure 4.7. Stability of equilibrium analysis for the Pisa Tower.

4.1.3 Implications of a path dependent solution

The conventional procedure of structural instability analysis for path-independent systems is developed in the P-ϑ plane, with P vertical load acting on the column. This plane must be used very carefully since it implies the variability of the vertical load, while our plastic analysis is load-path dependent. An example of application in this plane is the Lancellotta (1993) analysis for the Pisa Tower (Figure 2.36, Chapter 2). In this plane the peak of the curve corresponds to the critical-equilibrium state. Points on the curve to the left of the peak therefore represent stable equilibrium conditions and those on the right of it, unstable conditions. In Lancellotta's analysis the non-linear rotational spring at the base of the tower is elastic and, consequently, reacts with a constant resisting moment whatever weight (P=W) is taken into account. This is the reason why the shape of the stability curves is correct. The analysis conducted via the plastic model can be transferred, in the P-ϑ plane, but with some restrictions.

Because the Mr curve is load-path-dependent each value of P relates to a different one (Figure 4.8). It is important to realize that these solutions are applicable to a specific tower, i.e. that even on the same soil foundation they are only valid for a specific set of (W, θ, h) values, consequently, the dashed curves in Figure 4.8 are not generally applicable. Only the points on them intersected by the P=W=constant load path are now valid. The first highlighted point (from the left) in Figure 4.8 represents the current state of the Pisa Tower, the second, peak of the critical P-θ curve, define the critical condition. When any type of load path dependent phenomenon is involved, the analysis could be more safely conducted in the M-θ plane (Figure 4.7), or in the P-θ plane (Figure 4.8), but pointing out that the only two valid points of the P-θ curve are the points lying on the green line (Figure 4.8), corresponding to the weight of the tower.

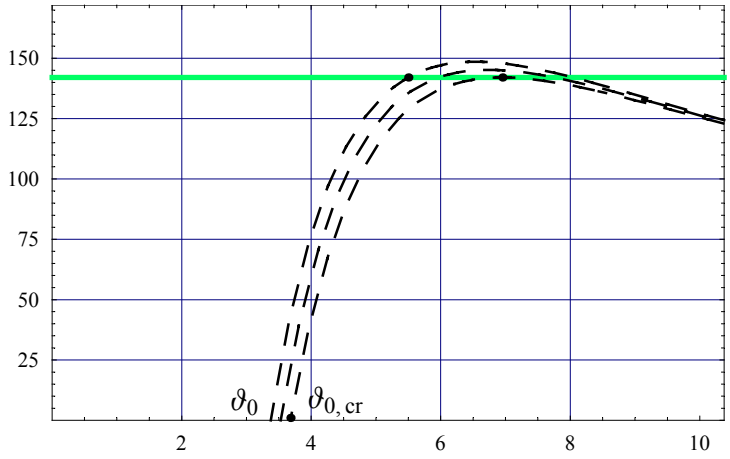

Figure 4.8. Stability of equilibrium analysis for the Pisa Tower in the *P-θ* plane, via the plastic model.

4.2 Bearing capacity

This Section refers to the bearing capacity analysis of foundations subjected to combined load developed in Section 2.1, Chapter 2. This is how an already very well understood problem, therefore nothing new will be added.

The knowledge of the failure envelope is sufficient to define the failure load conditions for a footing of radius R, subjected to a system of force resultants (V, H, M/2R). The significant load components in our analysis are the vertical load (V) and the moment (M), associated with a load-path as shown in Figure 4.9.

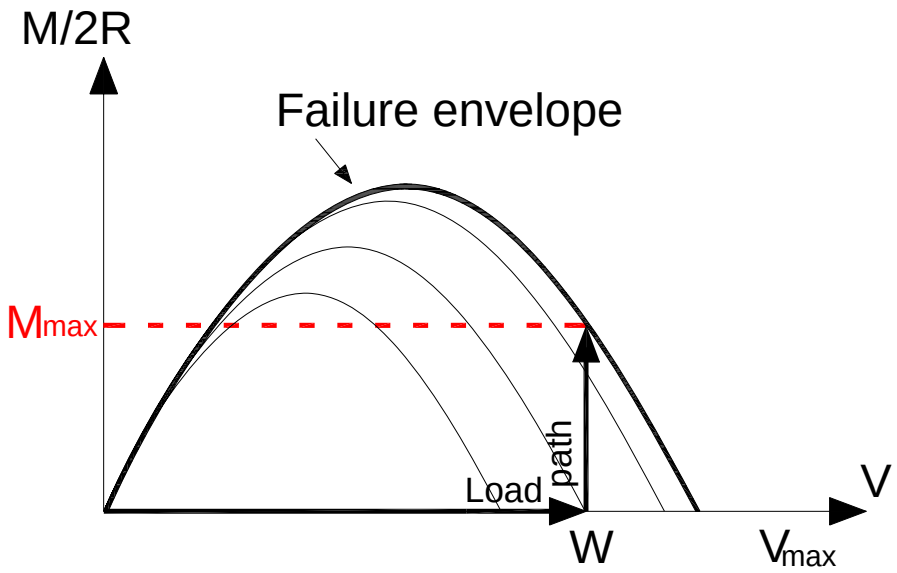

Figure 4.9. Significant load-path for a leaning tower.

The parameter that defines the size of the failure envelope is Vmax, which is taken to be the bearing capacity for a vertical central load, can be estimated using for example the Brinch Hansen (1970) formula.

With reference to the specific case of a leaning tower foundation, the maximum moment, M_{max}, of Figure 4.9, is the maximum moment that the tower foundation can support, at constant vertical load (W) and H=0. This provides the necessary information about soil resistance, which will be associated with the information about stiffness, in the following Section 4.3.

4.3 Rationalization of collapse mechanism predictions

The "*stability and strength analysis of leaning towers*" can be performed, in a quite rather elegant and intuitive way, in one single diagram in the M-θ plane. This can be achieved by means of strain hardening plasticity models, as explained in Section 4.1 and Section 4.2. In fact, starting from the stability of equilibrium analysis (Figure 4.3, *b)*), the information about bearing capacity failure can be added by incorporating the fact that the maximum moment (M_{max}, Figure 4.10) cannot be exceeded without the collapse of the tower due to bearing capacity failure. This value of the moment, plotted on the external moment load line, identifies the critical value of rotation (θ_f) for bearing capacity (Figure 4.10). Note that the M-θ curve, output of the applied plastic model, automatically includes the information about bearing capacity failure, since the load path must terminate when the maximum moment is reached (point B, Figure 4.10). This has been emphasized, in Figure 4.10, by outlining the part of the curve leading up to point B.

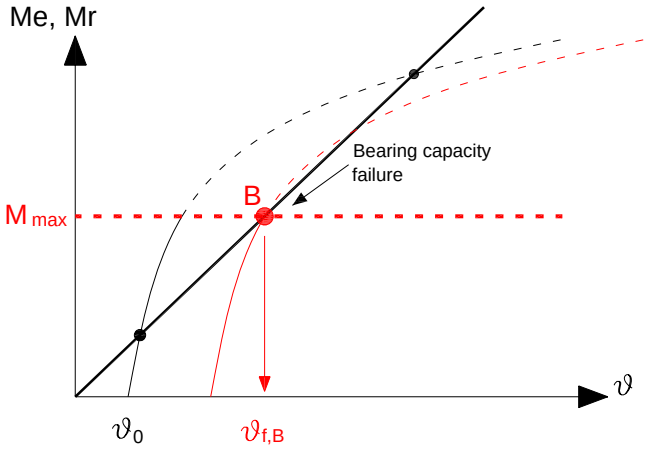

Figure 4.10. Bering capacity failure in the *M-θ* plane: "*strength analysis of a leaning tower*".

The superimposition of Figure 4.10 and Figure 4.3, *b)*, provides the predominant final failure mechanism. Two different conditions can occur:

- $\theta_{f,B} < \theta_{f,E}$, bearing capacity failure (Figure 4.11, *a)*)
- $\theta_{f,B} > \theta_{f,E}$, stability of equilibrium failure (Figure 4.11, *b)*)

Hence, the predominance of one mechanism over the other is governed by the translation of the M-*θ* curve along the *θ* axis, therefore, by the increase of creep rotations ($\theta_{0\,creep}$) with time.

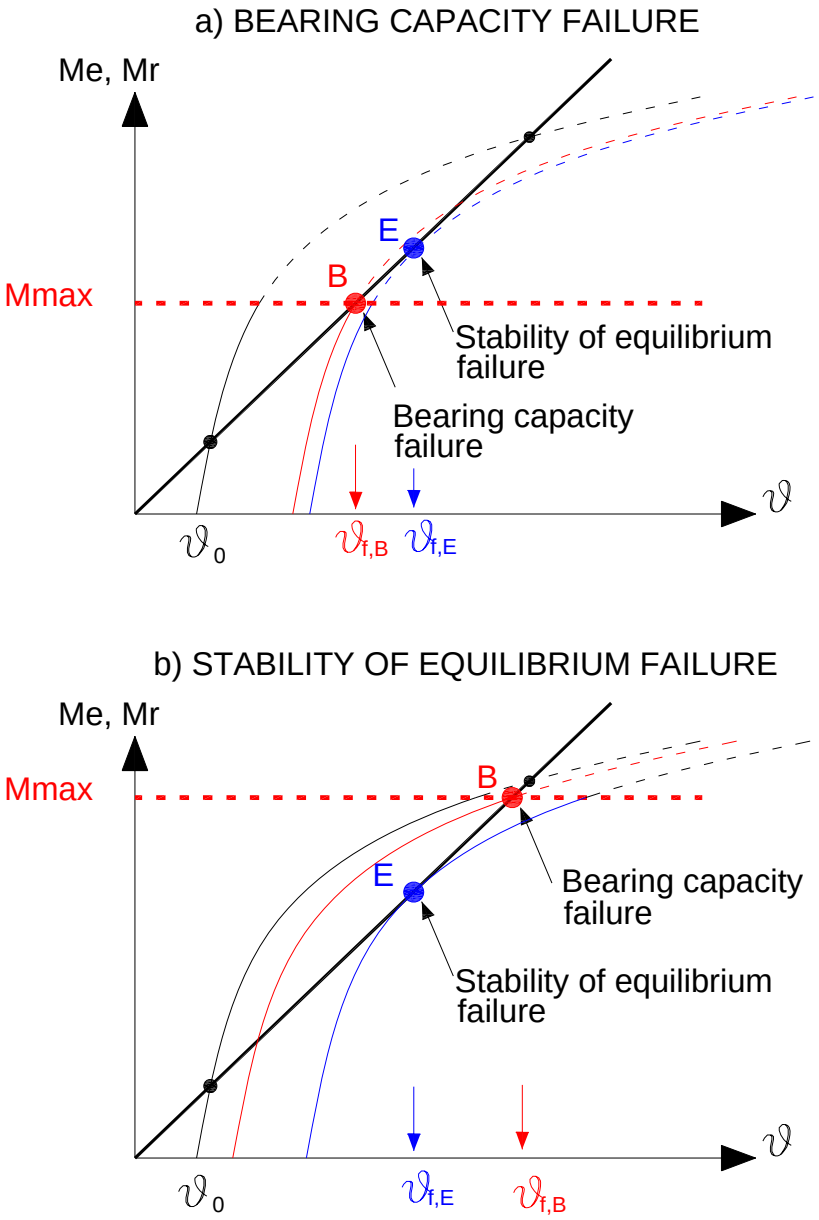

Figure 4.11. a) Bering capacity and b) stability of equilibrium failure in the *M-θ* plane: "*stability and strength analysis of a leaning tower*".

This proposed approach appears to be quite powerful, since it unifies stiffness and resistance problems, and allows inelastic theories to be avoid in stability of equilibrium analysis. Rules of the simpler static approach can be applied even if the analysis involves viscous phenomena.

4.4 Coupling creep with stability predictions

Coupling creep with stability predictions can be achieved very simply by incorporating the creep process in the plastic model, as suggested in Section 3.5, Chapter 3. In Figure 4.12, the two different interpretations of the failure condition for instability of equilibrium, are compared. In the 'old' one, described in Section 4.1.1, creep is incorporated as an initial rotation and point E_1 corresponds to the failure state. On the other side, according to the 'new' creep model, the failure condition can be again defined by the tangency between the external moment line and the M-θ curve, but with the different evolution of the curve. In fact, after the first load increment, in the $\delta M = W \cdot h \cdot \delta\theta$ series, the stiffness relevant to stability calculations is not the decreasing stiffness which occurs under 'rapidly' increasing instantaneous load (as considered in the 'old' analysis), but an increased one, related to the reloading stiffness. Instability will therefore not be a hazard until the 'virgin' stiffness curve is rejoined, in point E2, where the campanile will then collapse.

This interpretation of the effect of creep is totally different from the previous one, in which the creep can only have a detrimental effect on stability, whereas, this 'new' model, provides an explanation of how unexpectedly large rotations (as at Pisa) might be accommodated without collapse (but, nevertheless, with extensive periods of essentially neutral equilibrium).

If a reliable creep function $\xi(t)$ is defined, the foregoing analysis does, of course, also predict the time that the tilting/creeping structure will take to arrive at its collapse state. Note that the new improved collapse state, represented by E2, is safer, in terms of magnitude of rotation ($\theta_{f,E1} < \theta_{f,E2}$) and, consequently, in terms of time, but the fact that creep rates (Section 3.5.5, Chapter 3) increase when failure is approached, reduces the benefit of the increment of rotation magnitude at failure.

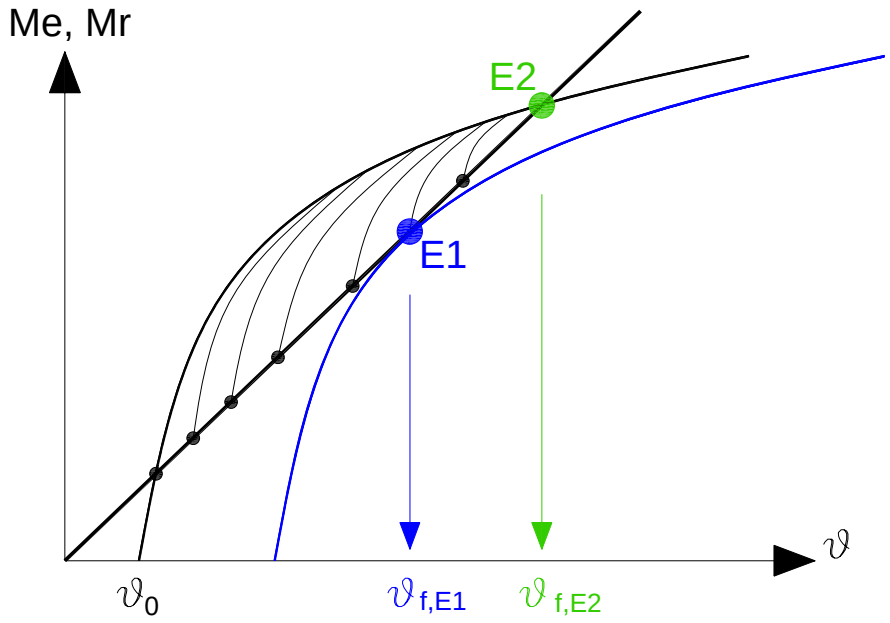

Figure 4.12. Rotational creep hardening.

4.5 Conclusion: the all in one diagram

The proposed methodology provides a new methodology for developing the stability and strength analysis of towers. A complete representation of the whole solution is shown in Figure 4.13 by a 4 quadrant picture. This is a comprehensive diagram in which the top-right quadrant represent the load state evolution (load-path) with the correspondent development of the yield surface; the bottom-right quadrant shows the vertical creep hardening; the top-left quadrant the rotational creep hardening with the stability of equilibrium and bearing capacity analysis.

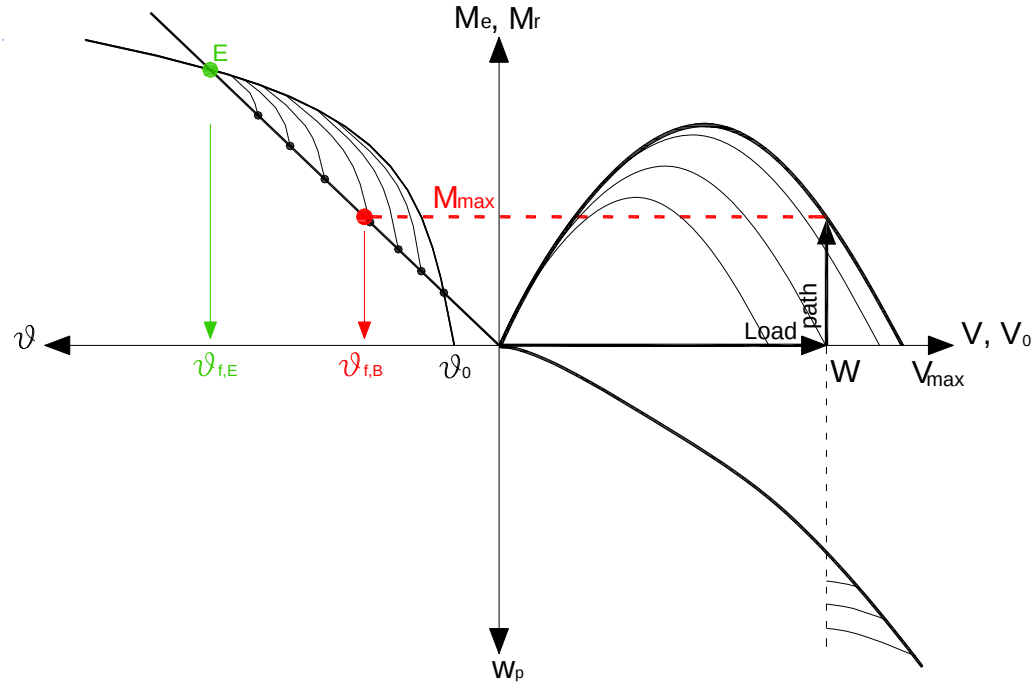

Figure 4.13. All in one diagram

PART III - *Applications to real cases*

CHAPTER 5

Using *Mathematica* in soil-structure interaction

Introduction

—In this final chapter the *stability and strength analysis of leaning towers* will be developed in the form of a *Mathematica notebook,* in relation to two case histories: Pisa Tower and Santo Stefano bell tower. Data used to perform the analyses (structural features and foundation ground soil characteristics of the towers) have already been described in Chapter 1. In the first section of this chapter there are some simple instructions for using a *Mathematica* notebook. The notebooks results are then discussed for the two cases studied in Section 5.2, for Pisa Tower, and 5.3, for Santo Stefano Bell Tower. As an example, a *cd,* with the two Notebooks and a free *Mathematica player* package, is attached to the thesis. These notebooks are also printed in Appendix B. The program does not enable the codes to be run but has been added in order to demonstrate the functionality of the notebook. The *Mathematica* code can perform numerical calculations, graphical visualization of results and, at the same time, editing of the text. Indeed, the whole thesis has been written using *Publicon* (a program that edits technical documents) and most of the diagrams shown in the text have been plotted using the code. In this chapter the intention of the author is not just to show the output of the proposed methodology, but also to point out the extensive use which can be made of the Wolfram code (*Mathematica*) in soil structure interaction analyses.

5.1 The *Mathematica Notebooks*

5.1.1 Basic instructions

'*Notebook*' is the name associated with documents developed using *Mathematica*. They are a single environment in which calculations, text, graphics, and other elements are combined. Each one of these elements is contained in cells, which are indicated by brackets on the right side of the document. As an example this cell, written with *Publicon*, is a text cell. An input cell is evaluated by pressing SHIFT+ENTER. Mathematica evaluates the input and gives back the result in an output cell underneath. Cells can be grouped together. When groups of cells are closed only the first cell of the group is displayed, whereas, all the other are hidden. All the cells belonging to a group can be displayed by clicking twice on the brackets on the right. These basic instructions will enable the reader to browse the explanatory notebooks presented in the attached *cd.* The *cd* also includes the *Mathematica player* (a free package, downloaded from the official web site: http://www.wolfram.com/products/player/) which must be installed in order to display the notebook.

5.1.2 Notebook contents

The Pisa and Santo Stefano *Notebooks* are accessible through the attached *cd* and Appendix B (a fully-opened printing of the two notebooks). They are a new proposal for performing soil-structure interaction analyses in one independent but complete environment (the *Notebook*), comprising text, calculations and graphic outputs. The elaborations are presented inside the Notebooks, whereas the results of the analyses are discussed in the two sections below.

5.2 Pisa Tower

5.2.1 The complete output of the strain hardening plastic soil model

The whole strain hardening plastic soil model, described and expanded in Chapter 3, has been applied to and solved for the Pisa Tower. The hardening law (based on the methodology suggested in Chapter 3) is plotted in Figure 5.1 and expressed by the exponential equation below which predict the vertical plastic displacement under a vertical central load of the Pisa Tower foundation (see the Notebook for the input parameters).

$$V_0 = 433\,(1 - e^{-0.21\,w_p}) \tag{5.1}$$

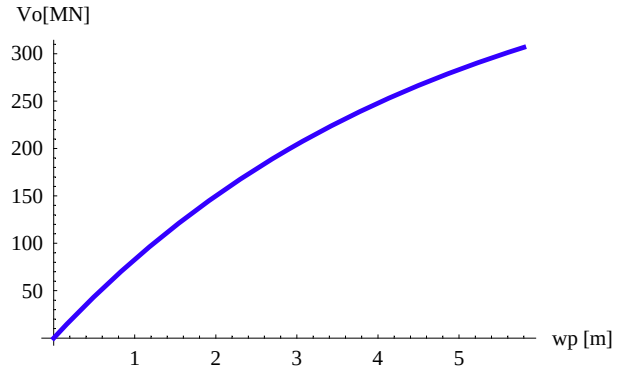

Figure 5.1. Hardening law for the Pisa Tower.

The output of a strain hardening plastic model for surface foundations, which develops the M-θ curve, also provides the vertical settlement. The complete output of the model is plotted in Figure 5.2, which shows the results of the model, from the V-w input of Figure 5.1 and for the specific load path of the Pisa Tower. The latter is characterized by the application of the weight (W=142 MN) of the tower (at constant null moment) followed by moment increments (δM= W·h·$\delta\theta$) under constant vertical load V=W, up to bearing capacity failure. The the bottom-right quadrant of Figure 5.2 shows an initial vertical settlement of 1.9 m, which include the immediate and consolidation settlement. This value is reasonable since the Tower is supposed to have subsided vertically by c. 2.5-3 m.

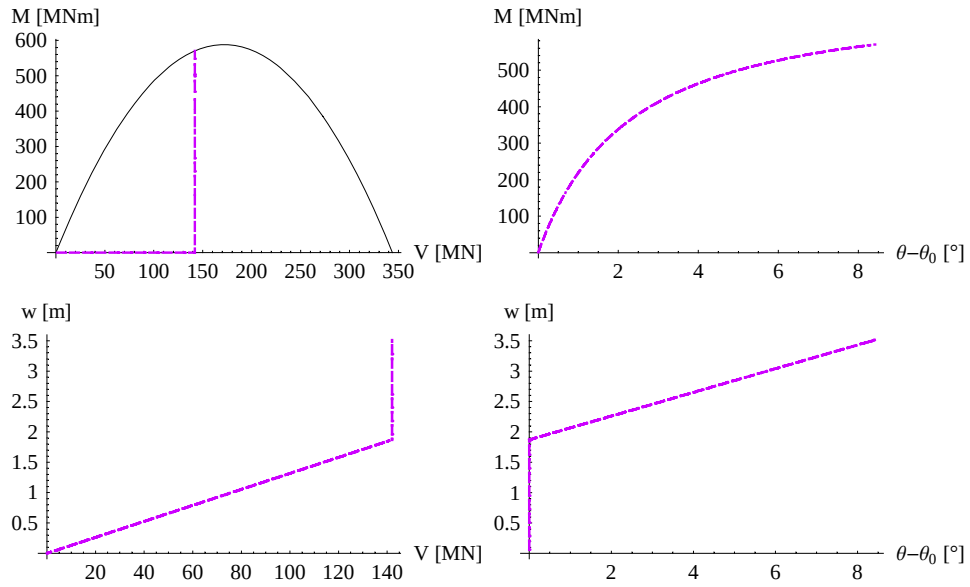

Figure 5.2. Complete output of the expanded (see Chapter 3) strain hardening plastic model for surface foundations, for the relevant Pisa Tower load-path.

5.2.2 Bearing capacity

The failure load conditions for a footing of diameter 2R, subjected to a system of force resultants (V, H, M/2R), can be defined once the failure envelope is known. The significant load components in our analysis are the vertical load (V) and the moment (M), associated with a load-path as shown in Figure 5.3 by the violet dashed line.

The size of the failure envelope is fixed by Vmax, which is taken to be the bearing capacity for a vertical central load of the Pisa Tower foundation. It has been estimated using the Brinch Hansen (1970) formula (see the *Notebook* for the input parameters and elaborations). This evaluation of the bearing capacity refers to drained conditions and shows that the increment of the moment due to additional rotation brings the foundation closer to the failure envelope. This has not been displayed in Figure 5.3 but will be displayed in the M-θ plane.

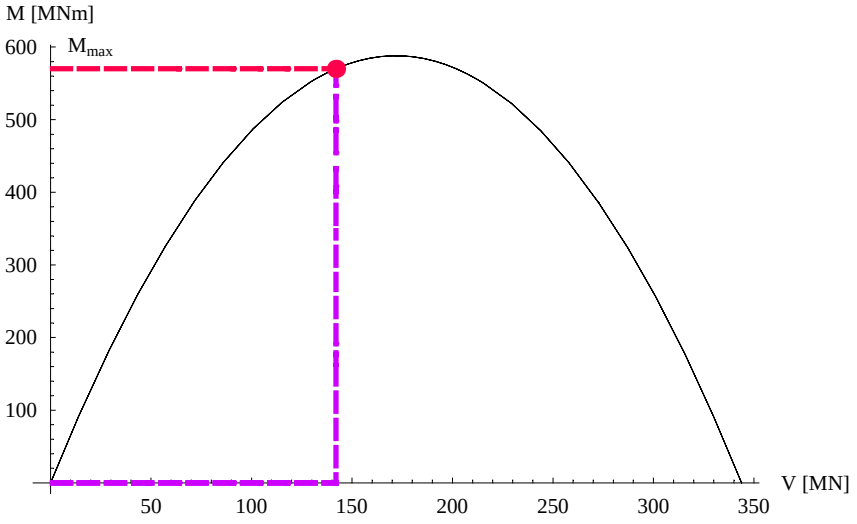

Figure 5.3. Significant load-path and bearing capacity for combined loading for the Pisa Tower.

5.2.3 Stability of equilibrium

Figure 5.4 shows the stability analysis of the Pisa Tower in the *M*-θ plane, developed using the strain hardening plastic model (the methodology is described in Chapter 4). The value of initial rotation, θ_0, enables the *M*-θ curve to be calibrated on the current value of rotation: $\theta_{current} = 5.5°$ is the actual rotation of the tower, which correspondent to an external moment, $M_{e,current}$=308 MNm (black point in Figure 5.4). The initial rotation, $\theta_{0\,ini,current}$, incorporating all historic creep deformations, and calibrated on ($\theta_{current}$, $M_{e,current}$) is 3.8°. This assesses the position of the curve in the plane, whereas the additional rotation necessary for instability of equilibrium failure is established by the tangency condition in point E (Figure 5.4). The coordinates of this failure point are (θ_{fE}, M_{fE})=(7.5, 422), which correspond to an initial rotation $\theta_{0\,ini,E} = 4.4°$.

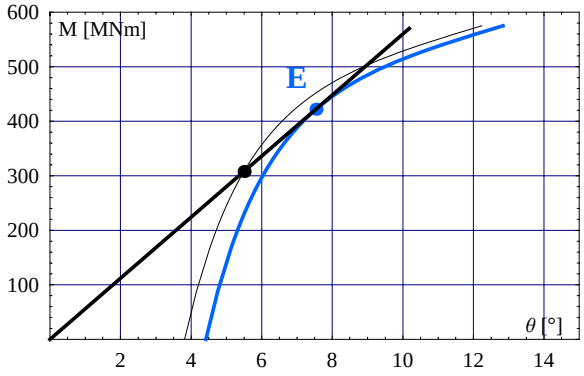

Figure 5.4. Stability of equilibrium analysis of the Pisa Tower

5.2.4 Collapse mechanism prediction

The Stability and strength analysis of the Pisa Tower is shown in Figure 5.5. This figure combines both the collapse mechanisms of the foundation and clearly shows which one occurs first. Obviously the predominant collapse mechanism is the one which corresponds to the smallest rotation. In this case the stability of equilibrium failure (point E) occurs for rotations smaller than those necessary to reach bearing capacity failure (point B). Quite easily a time scale may be associated to the rate of rotation and a prediction of the collapse time could be made.

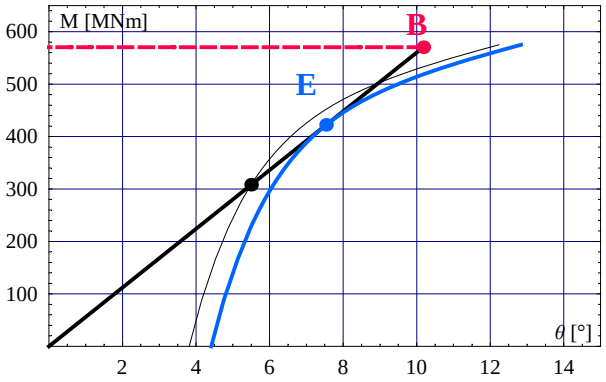

Figure 5.5. Stability and strength analysis of the Pisa Tower

5.2.5 Interpretation of the soil extraction intervention

This methodology may be a useful tool for the study of the influence on the stability of the tower of the soil extraction intervention, carried out from the 1999 to the 2001 on the Pisa Tower. The intervention caused a reduction of the inclination of $^1/_2$ degree. From the stability point of view this recovery in the inclination has moved the tower away from the instability condition, because the new current condition of rotation (point B' in Figure 5.6) is more distant from the tangency condition (point E in Figure 5.4) than the previous (point A in Figure 5.6). Since the model is rigid in unloading then the recovery must be interpreted as a recovery of the initial rotation. The point correspondent to the Tower situation will then move on the external moment line (it is shown by the A-B-B' schematic path in Figure 5.6) and the M-θ curve translated. During reloading the model will not predict any additional plastic rotation or settlement until the point A (Figure 5.6) is reached again. This interpretation is a simple example of how the methodology can be useful for the study of the evolution of the stability condition of a tower subjected to remedial measures.

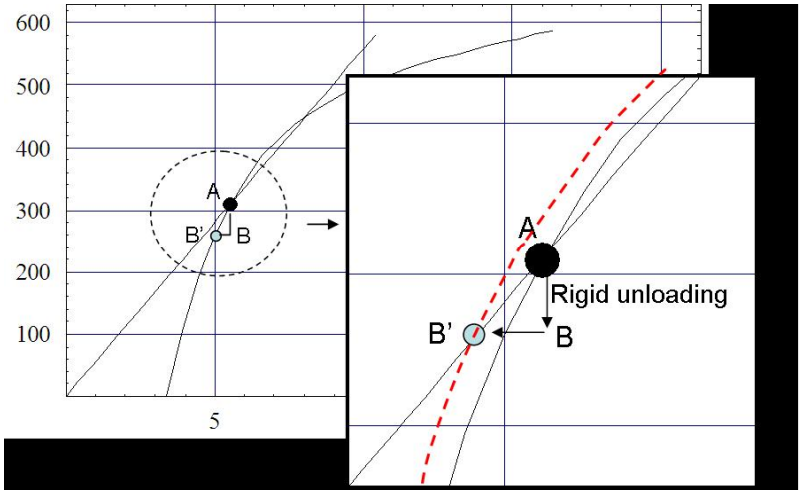

Figure 5.6. Interpretation of the soil extraction intervention

5.3 Santo Stefano bell tower

5.3.1 The complete output of the strain hardening plastic soil model

The whole strain hardening plastic soil model, described and expanded in Chapter 3, has also been applied to and solved for the Santo Stefano bell tower. The hardening law (based on the methodology suggested in Chapter 3) is plotted in Figure 5.7 and expressed by the exponential equation below which predict the vertical plastic displacement under a vertical central load of the Santo Stefano foundation (see the Notebook for the input parameters).

$$V_0 = 109\,(1 - e^{-0.5\,w_p}) \tag{5.2}$$

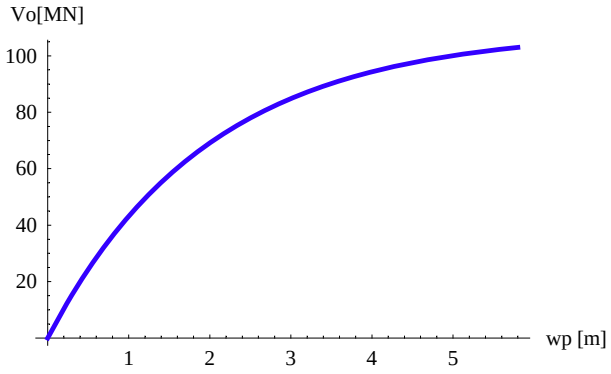

Figure 5.7. Hardening law for the Santo Stefano bell tower.

The output of a strain hardening plastic model for surface foundations, which develops the M-θ curve, also provides the vertical settlement. The complete output of the model is plotted in Figure 5.8, which shows the results of the model, from the V-w input of Figure 5.7 and for the specific load path of the Santo Stefano bell tower. The latter is characterized by the application of the weight (W=35 MN) of the tower (at constant null moment) followed by moment increments (δM= W·h·$\delta\theta$) under constant vertical load V=W, up to bearing capacity failure. The the bottom-right quadrant of Figure 5.8 shows an initial vertical settlement of c. 0.8 m, which include the immediate and consolidation settlement.

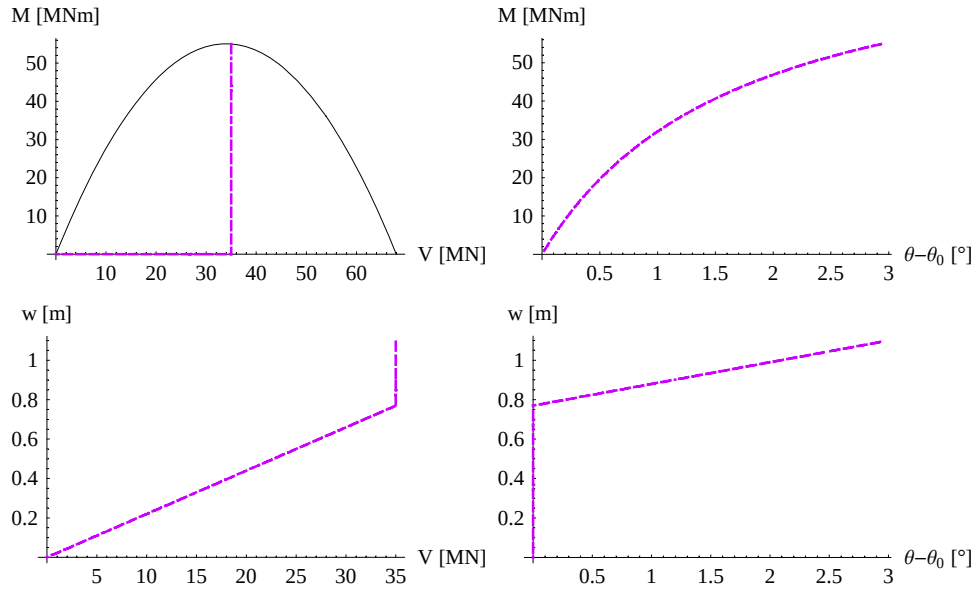

Figure 5.8. Complete output of the expanded (see Chapter 3) strain hardening plastic model for surface foundations, for the relevant Santo Stefano load-path.

5.3.2 Bearing capacity

The failure load conditions for a footing of diameter 2R, subjected to a system of force resultants (V, H, M/2R), can be defined once that the failure envelope is known. The significant load components in our analysis are the vertical load (V) and the moment (M), associated with a load-path as shown in Figure 5.9 by the violet dashed line.

The size of the failure envelope is fixed by Vmax, which is taken to be the bearing capacity for a vertical central load of the Santo Stefano foundation. It has been estimated using the Brinch Hansen (1970) formula (see the *Notebook* for the input parameters and elaborations). Note that the depth of embedment is calculated from the bottom of the canal, 1 m of embedment can be assumed, plus 2/3 of the length of the short wooden piles (2.7 m).

This evaluation of the bearing capacity refers to drained conditions and shows that the increment of the moment due to additional rotation bring the foundation closer to the failure envelope. This has not been displayed in Figure 5.9 but will be displayed in the M-θ plane.

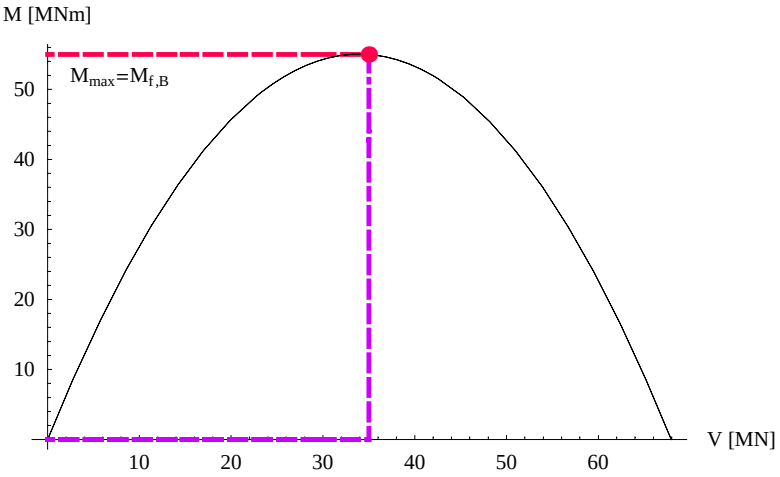

Figure 5.9. Significant load-path and bearing capacity for combined loading for the Santo Stefano bell tower.

5.3.3 Stability of equilibrium

Figure 5.10 shows the stability analysis of the Santo Stefano bell tower in the *M-θ* plane developed using the strain hardening plastic model (the methodology is described in Chapter 4). The analysis refers to the tower rotation in 1900, which was 2.2° ($=\theta_{current}$), before the construction of buttresses. In fact, in order to asses the current safety level of the tower, further investigations are required to suitably calibrate the proposed model to allow for the role played by the buttresses. The value of rotation in 1900 corresponds to an external moment, $M_{e,current}$=33.5 MNm (black point in Figure 5.10). The initial rotation, $\theta_{0\,ini,current}$, incorporating all historic creep deformations, and calibrated on ($\theta_{current}$, $M_{e,current}$) is 1.13°. This assesses the position of the curve in the plane, whereas the additional rotation which bring to the instability of equilibrium failure is established by the tangency condition in point E (Figure 5.10). The coordinates of this failure point are (θ_{fE}, M_{fE})=(2.56, 39), which correspond to an initial rotation $\theta_{0\,ini,E} = 1.17°$.

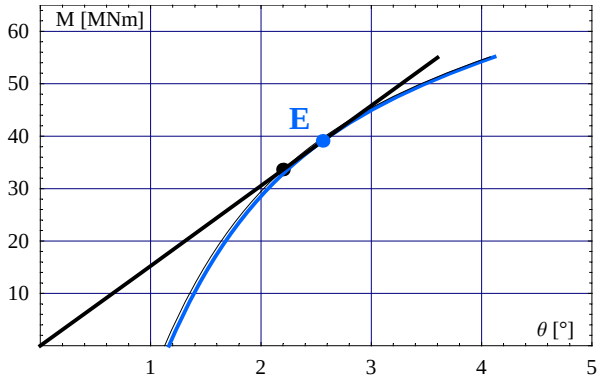

Figure 5.10. Stability of equilibrium analysis of the Santo Stefano bell tower.

5.3.4 Collapse mechanism prediction

The Stability and strength analysis of the Santo Stefano bell tower is shown in Figure 5.11 This figure combines both the collapse mechanisms of the foundation and clearly shows which one occurs first. Obviously the predominant collapse mechanism is the one which corresponds to the smallest rotation. In this case the stability of equilibrium failure (point E) occurs for rotations smaller than those necessary to reach bearing capacity failure (point B). In conclusion the analysis shows that at the beginning of the last century, before the construction of buttresses the stability condition of the Santo Stefano bell tower was very precarious, in fact, even if the bearing capacity failure, in 1900, was sufficiently remote, instability of equilibrium was nearly reached (superimposition of the black point over the blue in Figure 5.11). This demonstrates the crucial role played by buttresses, notwithstanding that further investigations are required to suitably calibrate the proposed model to allow for their effect.

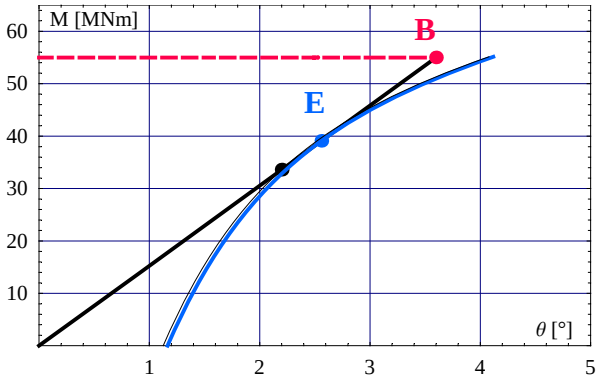

Figure 5.11. Stability and strength analysis of the Santo Stefano bell tower.

Conclusion

Introduction

—The thesis is concerned with the stability analysis of leaning towers, in relation to two possible distinct collapse mechanisms: (1) bearing capacity failure, due to lack of strength of the soil and (2) instability of equilibrium, due to lack of foundation stiffness. These problems have both been tackled using a work-hardening plasticity model for surface footings and developing an integrated approach between these two problems. Analytical techniques have been expanded and developed in the two main areas outlined in the research objectives: foundation modelling and soil structure interaction. In the sections below the main findings of the thesis are summarised, and some possible directions for the future work presented.

C.1 Summary of contributions

C.1.1 Foundation modelling

Analytical contributions to the specific performance of towers have been achieved by introducing new formulations in the original structure of work-hardening plasticity models for surface footings. Such extensions have been concerned with:

- **Hardening law**
  A new method of estimating a vertical stiffness curve from oedometer tests, following an augmented form of the Butterfield compression model (in the "log v-log p'" plane), has been developed. The potential of the suggested expression resides in the simplicity of the input parameters, which can be obtained from standard geotechnical survey data. The formulation, developed for towers, can easily be used for all type of foundations.

- **Scaled hardening**
  From an inspection of tests reported in the Gottardi (1992) PhD Thesis, it is evident that the application of the strain hardening law directly in terms of (V_0 , w_0) is not adequate. In fact, the experimental data shows clearly that if the vertical centreline load versus vertical displacement curve is used as the hardening function the predicted vertical displacement components are much too large. By analogy with Critical State

Soil Mechanics it underlines the fact that for the surface pads the value of the vertical displacement does not depend solely on the current value of the hardening parameter (*Vo* in the present case), but also on the value of the current load. A linear scaling of the hardening, depending on the ratio between the current vertical load (*V*) and the hardening parameter (V_o), is supported by the experimental evidences. This provides a simple, improved prediction of *w* (and, in conjunction with the plastic potentials *g*, predictions of *u* and θ). Again, experimental data departs slightly from the simplest model, and to obtain an excellent interpretation of Gottardi (1992)'s data involves scaling by a factor of about 0.9. This suggests that the simplest possible form of all the (f, g, V_o) functions can provide pratically adequate estimates of displacements.

- **Plastic Potentials**

  A "*universal load-path*" plastic potentials (*g*) for surface pad foundations has been developed, based on simple geometric shapes (i.e. 3D rotated ellipsoids and paraboloids) centred on the (*M/2R, H, V*) origin (0,0,0). The simplest possible useful form of the functions has been investigated, in order to fit laboratory data. These forms provided practically adequate estimates of post-consolidation displacements due to applied (*M/2R, H, V*) loading, whereas slightly elaborated forms have been necessary in order to interpret more precise data from laboratory experiments. Two plastic potential surfaces have been proposed: for '*radial*' load paths *g* takes the form of a *semi-ellipsoid,* for '*tangential*' load paths the basic form of g is a simple *paraboloid,* with its apex on the V axis. Both plastic potentials necessarily have geometrically similar, inclined elliptic cross-sections, perpendicular to the *V* axis, identical to *f*, in order to preserve associated flow in such planes. Contrary to the usual practice, *g* will not necessarily be either "shifted" or "scaled" to pass through the current load point. Rather, *load-paths will be extended* to the point where they intersect *g*. A validation of both plastic potential equations and superimposition of radial and tangential load paths has been demonstrated by reproducing some of Gottardi (1992) multi-load path results.

Such models has been analysed numerically using a standard numerical solution for systems of differential equation. This numerical solution, implemented in *Mathematica,* consists on a program that was used to perform retrospective simulations of several footing experimens and to elaborate the analysis of Pisa Tower and Santo Stefano bell tower.

Although these contributions to the foundation modelling have been developed specifically for studying tower behaviour, they nevertheless also represent a significant advance in the response analysis of surface pads.

- **Creep**

  The creep process has been incorporate in the foregoing foundation model in order to obtain a useful and realistic representation of the response of campanile over time. Using the model developed by Bjerrum in the 7th Rankine Lecture, a new vertical and rotational creep hardening formulation has been proposed. The creep model has to be able to account for the rate increasing as any load combination approaches a ‘bearing capacity‘ failure state. This additional model extension has general validity and has been particularly useful in the interpretation of stability of equilibrium evolution for tower subjected to such viscous processes.

C.1.2 Soil-structure interaction: rationalisation of collapse mechanisms prediction

The two possible distinct failure mechanisms, relevant to a stability analysis of the tower, (1) bearing capacity failure, due to lack of strength of the soil and (2) instability of equilibrium, due to lack of foundation stiffness, have been tackled using a work-hardening plasticity model for surface footings. The great potential of this approach is to combine, within a single analysis, stiffness and strength evaluations. Central to the stability analysis is the definition of the rotational stiffness of the foundation (i.e. curve M-θ), which can be used to limit the admissible moment load for the resistance of the foundation, but can be also used to evaluate the global equilibrium of the soil-foundation-structure system. Appling the model expansions (multiple plastic potentials, improved hardening law and scaling of the hardening) an improved methodology has been developed. The approach is based on the Cheney et al. methodology, in the M-θ plane, which has been improved to take into account the bearing capacity of the foundation in a single diagram. The use of the P-θ plane in the stability of equilibrium analysis has been abandoned, since the incorporation of a plastic model invalidates the use of this plane. The final achievement is the coupling of the creep and stability predictions. This has been accomplished by incorporating the creep process in the plastic model. The improved formulation can explain how unexpectedly large tower rotations might be accommodated without collapse.

The modelling of towers is challenging, its complexity arising from the interaction between a number of different phenomena. Only with confidence in the contribution from each component can one have confidence in the final result. In this thesis, several extensions of existing analitical techniques have been combined to generate what is believed to be a significant contribution to the modelling of a tower foundation.

C.2 Suggestions for future work

C.2.1 Creep

Much of the basic creep model is now available, and applicable to the stability analysis of towers. The calibration and validation of such a model will have to be done using field data but, unfortunately, only very frugal campanile-creep data exist. The collection of such data is possible and would enable a significant advance to be made.

C.2.2 Animated *Mathematica* Notebook

Wide use of the *Mathematica* code has been made throughout the thesis. The use of the same program in data elaboration, writing up, numerical simulation, graphical output, etc, represents an innovation which enables all aspects of soil-structure interaction problems to be handled in a consistent way. An idea in the further develop of the this work is to create an animated *Mathematica* notebook that could demonstrate tower behaviour, from the beginning of the construction up to a real-time animation of the collapse and subsequent disintegration of a specific tower.

References

Bazant, Z. P., & Cedolin, L. (1991). *Stability of Structures*. New York: Oxford University Press.

Bjerrum, L. (1967). *Engineering geology of Norwegian normally-consolidated marine clays as related to settlements of buildings. Seventh Rankine Lecture*. Géotechnique, **17**, 81–118.

Brinch-Hansen, J. (1970). *A revised and extended formula for bearing capacity*. The Danish Geotechnical Institute, Copenhagen. Bull. N. 28.

Butterfield, R. (1997, October). *Benefit without Cost in a Mechanics Laboratory*. Journal of Engineering Education, **86**(4).

Butterfield, R. (1979). *A natural compression law for soils*. Géotechnique, **29**(3), 469–480.

Butterfield, R. (1981). *Another look at gravity platform foundations*. Conf. of SMFE in offshore technology, **Udine**(CISM), 259–261.

Caquot, A., & Kérisel, J. (1966). *Traité de mécanique des sols*. Paris: Gauthier-Villars.

Casoni, G. (1851). *Sopra un singolare apparato di fondazione scoperto nell'occasione che fu disfatta un'antica torre in Venezia. Memoria del M. E. Ingegn. Giovanni Casoni*. Venezia: Istituto Veneto.

Cheney, J., Abghari, A., & Kutter, B. L. (1991). *Stability of leaning towers* . J. ASCE-GED, **CXVII**(2), 297–318.

Como, M. (1993). *Plastic and Visco-Plastic Stability of Leaning Towers*. Atti del Convegno Internazionale in memoria di Giulio Krall Fisica Matematica e Ingegneria delle Strutture: rapporti e compatibilità, **Isola d'Elba**(Italia), 191–214.

Das, B. M. (1995). *Principles of Foundation Engineering*. Boston: PWS Publishing Company.

DeBeer, E. E. (1970). *Experimental determination of the shape factors and the bearing capacity factors on sand*. Géotechnique, **20**(4), 387–411.

Desideri, A., Russo, G., & Viggiani, C. (1997, Gennaio-Marzo). *La stabilità di torri su terreno deformabile*. RIG, **1**, 5–21.

EN. (1998). *Eurocode 8: Design of structures for earthquake resistance*.

Ferretti, D., Iori, I., & Morini, M. (2002). *La stabilità delle strutture. Il caso delle costruzioni in cemento armato*. Milano: McGraw-Hill.

Gottardi, G. (1992). *Modellazione del comportamento di fondazioni superficiali su sabbia soggette a diverse condizioni di carico* (Doctoral Dissertation, Scuola di Dottorato di Torino, Genova, Padova e Milano)

Gottardi, G., & Houlsby, G. T. (1995). *Model tests of circular footings on sand subjected to combined laods*. Department of Engineering Science, Oxford University, Oxford . OUEL 2071/95.

Gottardi, G., Houlsby, G. T., & Butterfield, R. (1999). *Plastic responce of circular footings on sand under general planar loading*. Géotechnique, **49**(4), 453–469.

Gourvenec, S. (2004). *DESIGN CONSIDERATIONS FOR OFFSHORE SHALLOW FOUNDATIONS*. Retrieved 2006 from: http://www.cofs.uwa.edu.au .

Habib, P., & Puyo, A. (1970). *Stabilite des foundation des constructions de Grande Hauteur*. Annales ITBTP, pp. 117-124: in French.

Hambly, E. C. (1984, 11 30). *Oil rigs dance to Newton's tune*. Draft discourse to royal institution, February 8th 1985, 1–41.

Hambly (1985, March). *Soil buckling and the leaning instability of tall structures*. The Structural Engineer, **63A**(3), 77–85.

Heyman, J. (1992). *Leaning Towers*. Meccanica, **27**(3), 153–159.

Houlsby, G. T., & Cassidy, M. J. (2002). *A plasticity model for the behaviour of footings on sand under combined loading*. Géotechnique, **52**(2), 117–129.

Koiter, W. T. (1953). *Stress-strain relations, uniqueness and variational theorems for elastic-plastic materials with a singular yield surface*. Quart. Appl. Math, **11**, 350–354.

Lancellotta, R. (1993). *Stability of a rigid column with non linear restraint*. Géotechnique, **43**(2), 331–332.

Marchi, M., Gottardi, G., & Lionello, A. (2006). *Sulle fondazioni dei campanili a Venezia*. In . <Last> (Ed.), *Fifth National Symposium of Researchers in Geotechnical Engineering* (pp. 177–192). Bari: Helvenius.

Meyerhof (1963). *Some recent research on the bearing capacity of foundations*. Can. Geotech. J., **1**(1), 16–26.

Nova, R., & Montrasio, L. (1991). *Settlements of shallow foundations on sand*. Géotechnique, **41**(2), 243–256.

Nova, R., & Montrasio, L. (1995). *Un'analisi di stabilità del capanile di Pisa*. Rivista Italiana di Geotecnica , **2**, 83–93.

Opera Primaziale Pisana., *Pisa Tower Official website*. Retrieved 27/12/2007 from http://torre.duomo.pisa.it/

Pepe, M. (1995). *La torre pendente di Pisa. Analisi teorico sperimentale della stabilità dell'equilibrio*. PhD Thesis, **Politecnico di Torino**.

Ricceri, G., Mazzucato, A., & Soranzo, M. (1992). *Interazione terreno-struttura per alcuni antichi monumenti*. Istituto di costruzioni marittime e di geotecnica, Università di Padova

Simonini, P., & Cola, S. (2000). *Use of piezocone to predict maximum stiffness of Venetian soils*. Journal of Geotechnical and geoenvironmental Engineering, ASCE, **126**(4), 378–382.

Terzaghi, K. (1943). *Theoretical soil mechanics* . New York: John Wiley and Sons.

Various Authors. (2006). *La Torre restituita: gli studi e gli interventi che hanno consentito la stabilizzazione della torre di Pisa*. Roma: Istituto poligrafico e zecca dello Stato, Libreria dello Stato.

Vesic, A. S. (1975). *Bearing capacity of shallow foundations*. In Foundation Engineering Handbook. New York: Winterkorn e Fang (Eds.), **Cap. 3**, 121–147.

Wolfram, S. (1999). *The Mathematica Book. Version 4*. Cambridge: Cambridge University Press.

Zuccolo, G. (1975). *Il restauro statico nell'architettura di Venezia*. Istituto Veneto di Scienza Lettere ed Arti, **Venezia**(in Italian).

A P P E N D I X A

Implementation of models in *Mathematica*

Introduction

—In this appendix the implementation of the model is developed

A.1 General plastic load-displacement relationship

The model is thus one of the strain-hardening plasticity type.

The precise form of the hardening law is specified by a relationship between the size of the yield (V_0) surface and the plastic vertical deformation (w^p). The form of the strain-hardening expression can be determined from a vertical load–penetration curve, since for pure vertical loading $V_0 = V$.

In general:

Hardening law

$Vo = \mathcal{F}o[w^p]$

The yield surface can be in a nonspecific manner expressed as follows, where V_0 is the parameter that defines the size of the yield surface. Within the yield surface, where the deformation is assumed as elastic, the behavior can be specified by a set of *elastic moduli*.

Yield surface

$f = (V,\ M,\ H,\ V_0,\ \text{etc} ...)$

In the (M/2R, H) plane an associated flow rule is found to model the ratios between the plastic displacements well, but this is not the case in the (V, M/2R) or (V, H) planes. A plastic potential different from the yield surface must therefore be specified. Since the expression of the plastic potential is not crucial for the following analysis, now we can leave it general

Plastic potential

$g(V,\ M,\ H,\ V_0,\ \text{etc} ...)$

We can define the relation between incremental plastic displacements and increment of load for shallow foundations:

- Increment of plastic displacement vector: $\delta q^p = \begin{pmatrix} \delta \mathrm{w}^p \\ \delta \theta^p \\ \delta \mathrm{u}^p \end{pmatrix}$

- Increment of load vector: $\delta Q = \begin{pmatrix} \delta \mathrm{V} \\ \delta \mathrm{M} \\ \delta \mathrm{H} \end{pmatrix}$

The plastic displacement increments for a mechanism of plastic deformation related to the normal to the plastic potential at the current effective load state so that

$$\begin{pmatrix} \delta \mathrm{w}^p \\ \delta \theta^p \\ \delta \mathrm{u}^p \end{pmatrix} = \chi \begin{pmatrix} \frac{\partial g}{\partial V} \\ \frac{\partial g}{\partial M} \\ \frac{\partial g}{\partial H} \end{pmatrix} \tag{1.1}$$

Where χ is a variable scalar multiplier whose value will be derived subsequently from the assumed hardening characteristics of the soil.

In the most general case the change in size of the yield loci, that is change in Vo, is linked with increments of all the components of plastic incremental displacements according to the hardening rule

$$\delta V_o = \frac{\partial V_o}{\partial w^p} \delta \mathrm{w}^p + \frac{\partial V_o}{\partial \theta^p} \delta \theta^p + \frac{\partial V_o}{\partial u^p} \delta \mathrm{u}^p \tag{1.2}$$

The differential form of the yield loci (consistency condition) is

$$\frac{\partial f}{\partial V} \delta \mathrm{V} + \frac{\partial f}{\partial M} \delta \mathrm{M} + \frac{\partial f}{\partial H} \delta \mathrm{H} + \frac{\partial f}{\partial V_o} \delta \mathrm{V}_o = 0$$

$$\frac{\partial f}{\partial V} \delta \mathrm{V} + \frac{\partial f}{\partial M} \delta \mathrm{M} + \frac{\partial f}{\partial H} \delta \mathrm{H} = -\frac{\partial f}{\partial V_o} \delta \mathrm{V}_o \tag{1.3}$$

Combining Equation 3 and Equation 2

$$\frac{\partial f}{\partial V} \delta \mathrm{V} + \frac{\partial f}{\partial M} \delta \mathrm{M} + \frac{\partial f}{\partial H} \delta \mathrm{H} = -\frac{\partial f}{\partial V_o} \left(\frac{\partial V_o}{\partial w^p} \delta \mathrm{w}^p + \frac{\partial V_o}{\partial \theta^p} \delta \theta^p + \frac{\partial V_o}{\partial u^p} \delta \mathrm{u}^p \right) \tag{1.4}$$

Substituting terms of Equation 1.1 in Equation 4

$$\frac{\partial f}{\partial V} \delta \mathrm{V} + \frac{\partial f}{\partial M} \delta \mathrm{M} + \frac{\partial f}{\partial H} \delta \mathrm{H} = -\frac{\partial f}{\partial V_o} \left(\frac{\partial V_o}{\partial w^p} \chi \frac{\partial g}{\partial V} + \frac{\partial V_o}{\partial \theta^p} \chi \frac{\partial g}{\partial M} + \frac{\partial V_o}{\partial u^p} \chi \frac{\partial g}{\partial H} \right) \tag{1.5}$$

Equation 5 yields an expression for the scalar multiplier χ

$$\chi = \frac{\frac{\partial f}{\partial V} \delta \mathrm{V} + \frac{\partial f}{\partial M} \delta \mathrm{M} + \frac{\partial f}{\partial H} \delta \mathrm{H}}{\frac{\partial f}{\partial V_o} \left(\frac{\partial V_o}{\partial w^p} \frac{\partial g}{\partial V} + \frac{\partial V_o}{\partial \theta^p} \frac{\partial g}{\partial M} + \frac{\partial V_o}{\partial u^p} \frac{\partial g}{\partial H} \right)} \tag{1.6}$$

Substituting Equation 6 in Equation 1.1

$$\begin{pmatrix} \delta w^p \\ \delta\theta^p \\ \delta u^p \end{pmatrix} = -\frac{1}{\frac{\partial f}{\partial V_o}\left(\frac{\partial V_o}{\partial w^p}\frac{\partial g}{\partial V} + \frac{\partial V_o}{\partial \theta^p}\frac{\partial g}{\partial M} + \frac{\partial V_o}{\partial u^p}\frac{\partial g}{\partial H}\right)}$$

$$\left(\begin{array}{cc|cc|cc} \frac{\partial f}{\partial V} & \frac{\partial g}{\partial V} & \frac{\partial f}{\partial M} & \frac{\partial g}{\partial V} & \frac{\partial f}{\partial H} & \frac{\partial g}{\partial V} \\ \hline \frac{\partial f}{\partial V} & \frac{\partial g}{\partial M} & \frac{\partial f}{\partial M} & \frac{\partial g}{\partial M} & \frac{\partial f}{\partial H} & \frac{\partial g}{\partial M} \\ \hline \frac{\partial f}{\partial V} & \frac{\partial g}{\partial H} & \frac{\partial f}{\partial M} & \frac{\partial g}{\partial H} & \frac{\partial f}{\partial H} & \frac{\partial g}{\partial H} \end{array}\right)\begin{pmatrix} \delta V \\ \delta M \\ \delta H \end{pmatrix} \tag{1.7}$$

Once fixed *f*, *g*, and Vo, Equation 7 can be numerically solved to obtain a complete solution for displacements for any load path.

A compact form of Equation 7 is

$$\delta q^p = -\frac{1}{H}[\mathrm{Mat}]\,\delta Q \tag{1.8}$$

Since in our case hardening depends only on w^p, and not on θ^p and u^p

$$Vo = \mathcal{F}o[w^p] \Longrightarrow H = \frac{\partial f}{\partial V_o}\frac{\partial V_o}{\partial w^p}\frac{\partial g}{\partial V}$$

A.2 Integration of the model

A numerical solution has been realized using the program '*Mathematica 5.0*'. The solution has been developed using the command *NDSolve* which finds a numerical solution to a system of ordinary differential equations.

The Mathematica function NDSolve is a general numerical differential equation solver. It can handle a wide range of ordinary differential equations (ODes). In a system of ordinary differential equations there can be any number of unknown functions, but all of these functions must depend on a single "independent variable", which has to be the same for each function (Wolfram, 1999).

The main program developed to perform the tests predictions shown in Chapter 3, section 3.3, has been formulated in terms of displacements. The independent variable used to perform the calculation has been w_p. The validity of this solution applied to load controlled tests has been assessed by developing a similar program in which the independent variable was the load (i. e. *H*, *M*, or *V*). Figure A.1 shows a comparison of the two type of solution: the violet line is the displacement-controlled solution, the green line is the load-controlled solution. The output of the program was the same in both simulations done for the same test. This result has validated the applicability of a displacement-controlled solution in the simulation of load-controlled tests.

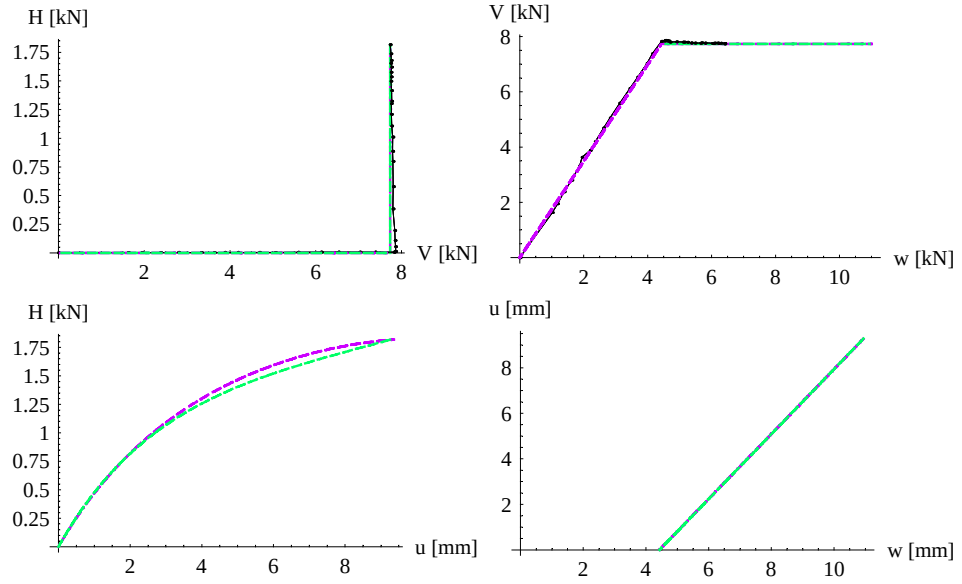

Figure A.1 Comparison of two type of solution: a displacement-controlled solution (*violet line*), a load-controlled solution (*green lin*e).

A P P E N D I X B

Pisa Tower & Santo Stefano bell tower *Notebooks*

Introduction

—This appendix shows a fully-opened printing of the Pisa Tower and Santo Stefano bell tower notebooks. The two notebooks are accessible also from the attached cd.

B.1 Pisa Tower *Notebook*

Stability and strength analysis of the Pisa Tower

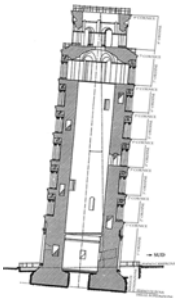

Introduction

— The following code performs a stability and strength analysis of the leaning Tower of Pisa: a bearing capacity analysis (foundation not strong enough) is coupled with one for instability of equilibrium (foundation not stiff enough). For the input data see Chapter 1, for the underlying theoretical analysis see Chapter 3 and Chapter 4 and for notebook instructions and discussion of results see Chapter 5 of the thesis.

CHARACTERISTICS OF THE TOWER

The characteristics of the Pisa Tower are extensively reported in Section 1.1, Chapter 1, and summarised below:

Properties
The height of the building from its foundations to the belfry is c.60m;
-The ring-shaped foundation has an external diameter of 19m;
-The Tower weight c.142 MN;
-The Tower is shaped like a hollow cylinder formed by two concentric walls (in marble blocks) which contain mortar and other matter;

Rotations and Settlements
- The Tower has subsided vertically by c. 2.5m÷3m since the beginning of its construction in 1173.
- The differential settlement is 1.89m; this means that the extreme north and south edges have subsided by 1.86m and 3.75m respectively.
- The inclination measured in 1911 was 5°14'46".
- The inclination measured in 1993 was 5°33'36".
- The rate of rotation of the Tower has accelerated from 4" per year in the 1930s to 6" per year at the end of the 1980s.

Stratigraphy
- Between ground level and a depth of about 10 m (complex A): sands and silts with irregular stratification with a prevalence of clayey-silts under the southern part of the Tower (it is claimed that this is the underlying cause of the inclination of the monument).
- Between 10m and circa 40m depth (complex B): soil composed primarily of soft clays with an intervening layer of sand. The upper surface of the clay, more or less horizontal over all of the square, is depressed by more than two metres underneath the Tower; this is a deformation induced over the

centuries by the weight of the Tower. This fact leads to the estimation that the overall subsidence of the Tower has been between 2.5 and 3 metres.

ANALYSIS

Input parameters

Properties (geometry and weight of the foundation/tower)

WT: weight of the tower [MN];
hG: height of mass gravity center of the tower [m];
(2R): length of the foundation of the tower (*2R* is indicated by *RR* in the code) [m];
d: depth of the foundation [m];
Di, *De*: internal and external diameter of the ring-shaped foundation [m];
hw: depth of the water level (from the soil level) [m];

```
WT = 142; hG = 22.6;  d = 3; hw = 3; De = 19; Di = 4.5; RR = De;
```

Soil proprieties

ϕ: angle of friction (NB for the long term we must always take c'=0 kPa) [°];
γ_{sat}: saturated unit weight [kN/m^3];
γ_{dry}: dry unit weight [kN/m^3];
γ_w: water unit weight [kN/m^3];
C'0: compression parameter;
C'0/C'r: ratio between compression parameters;
n: parameter defined from the value of OCR at a known depth (Equation 3.14, Chapter 3);

```
ϕ = 26;  γdry = 15; γsat = 20; γw = 10;
Co = .08; CoCrratio = 8 ; n = 16;
```

Hardening law

The hardening law for the Pisa Tower is developed in the embedded code (based on the methodology suggested in Chapter 3) and plotted in Figure 1. The solution of this code can be interpolated to provide the exponential expression below

$$V_0 = A(1 - e^{-B w_p})$$

```
Show[VowocurvePLOT]
```

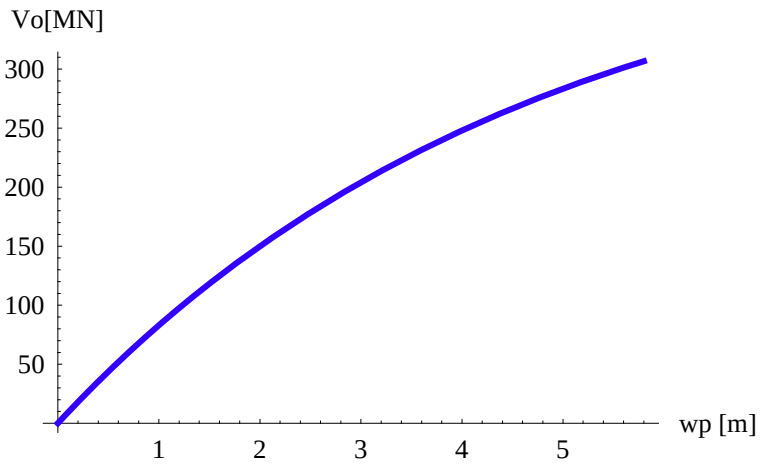


```
- Graphics -
```

Figure 1. Hardening law for the Pisa Tower.

The values of the parameters in V_0 equation are:

```
A
```

```
432.606
```

```
B
```

```
0.212778
```

The complete output of the model

The output of a strain hardening plastic model for surface foundations, which develops the M-θ curve, also provides the vertical settlement. The complete output of the model is plotted in Figure 2, which shows the results of the model, from a V-w input, for a specific load path. A typical tower load path is characterized by the application of the weight (W) of the tower (at constant null moment) during construction followed by moment increments (δM= W·h·$\delta\theta$) under constant vertical load V=W.

The following code solves the model for the Pisa Tower, i. e. firstly the weight of the tower is applied (W=142 MN) at constant null moment (M=0), then the moment is increased incrementally (δM=W·h·$\delta\theta$), at constant V=W, up to bearing capacity failure.
As explained in Chapter 3 the equations of the model depend on the geometry of the system, the soil properties and, in particular, the vertical centreline load capacity of the soil-foundation system (V_{max}, calculated in the embedded code).

```
Show[GraphicsArray[{{VM, ∂Mp}, {wV, ∂wp}}],
 GraphicsSpacing → .005]
```

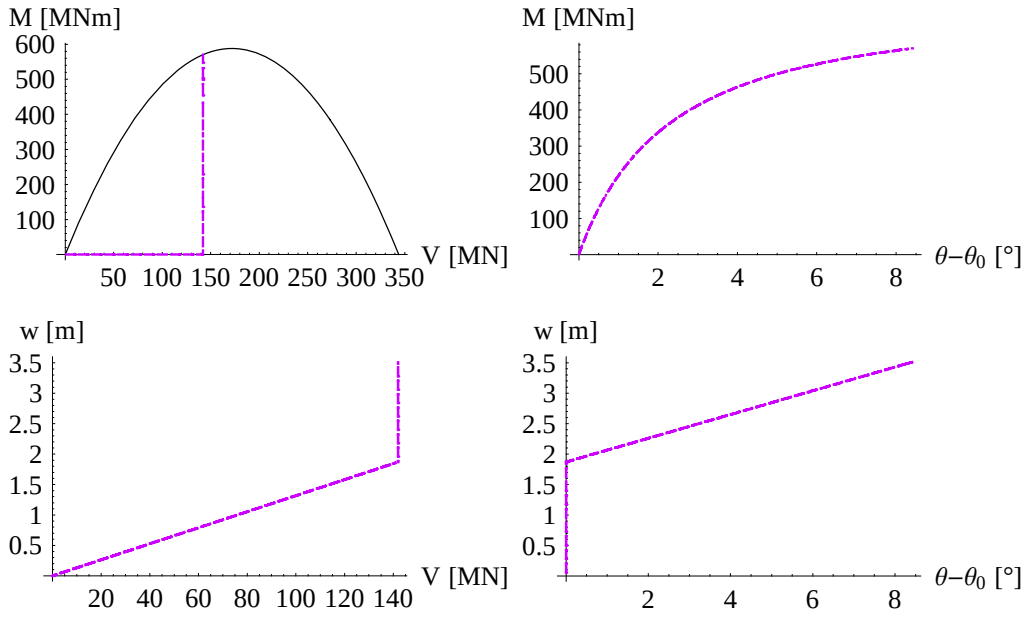


```
- GraphicsArray -
```

Figure 2 Complete output of the expanded (see Chapter 3) strain hardening plastic model for surface foundations, for the relevant Pisa Tower load-path.

M-θ curve

The M-θ curve has been deduced from the strain hardening plastic model for surface foundations, expanded as explained in Chapter 3. The rotational stiffness of a surface pad is *load path dependent*, consequently every specific load path generates a different curve. The output of the code is a numerical solution which can be interpolated to provide an augmented exponential expression:

$$M_r = p\,[1 - e^{-(q-r)(\vartheta-\vartheta_0)}] + p\,r\,(\vartheta - \vartheta_0)$$

The interpolating function for *M-θ* (Figure 3), from the numerical solution, is developed in the embedded code.

```
MθPLOTModExp = Plot[ MθcurveModExp[Δθ], {Δθ, θini, θpmax},
  AxesLabel → {"Δθ [°]", "M[MNm]"}, AxesOrigin → {0, 0},
  PlotStyle → {Hue[.95], Thickness[.01]}]
```

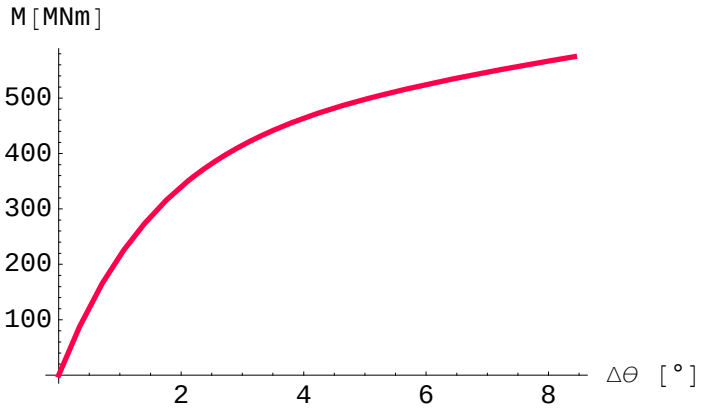


```
- Graphics -
```

Figure 3 M-θ curve for the Pisa Tower, from the strain hardening plastic model for surface pads.

The values of the parameters in M_r equation are:

```
p
```

```
429.346
```

```
q
```

```
0.660509
```

```
r
```

```
0.040924
```

Note that the final curve (M-ϑ curve ≡ Mr: resisting moment developed by the foundation during the rotation) is a non-linear function of $\Delta\theta = \theta\text{-}\theta_0$. Figure 4 shows that ϑ is the total rotation of the foundation from the vertical position, ϑo is an initial imperfection (due to either eccentricity or initial inclination developed during construction) and not associated with the resisting moment, whereas $\Delta\theta=(\vartheta\text{-}\vartheta o)$ is the absolute rotation associated with the resisting moment.

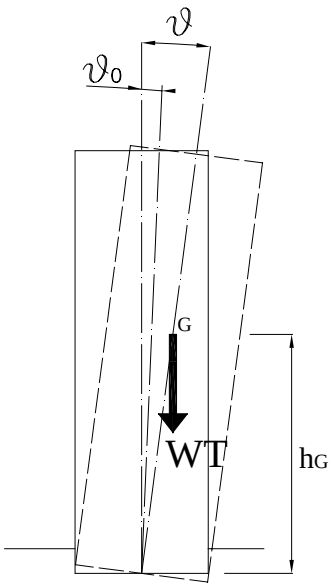

Figure 4 Sketch of a tower.

Strength analysis - Bearing capacity

The maximum moment, $M_{f,B}$ [MNm] (Figure 5) that the tower foundation can support, at constant vertical load (W) and H=0 is calculated in the embedded code.

```
VMbcap = Show[VMbearcap, parabolaVmax,  VM, VMini,
  Graphics[{Hue[.95], PointSize[0.025], pMVbc}],
  AxesLabel → {"V [MN]", "M [MNm]"},
  TextStyle → {FontFamily → "Times", FontSize → 10},
  Epilog → {Text["Mmax=Mf,B", {10, .3}, {-1, -25},
     TextStyle → {FontFamily → "Times", FontSize → 10}]}]
```

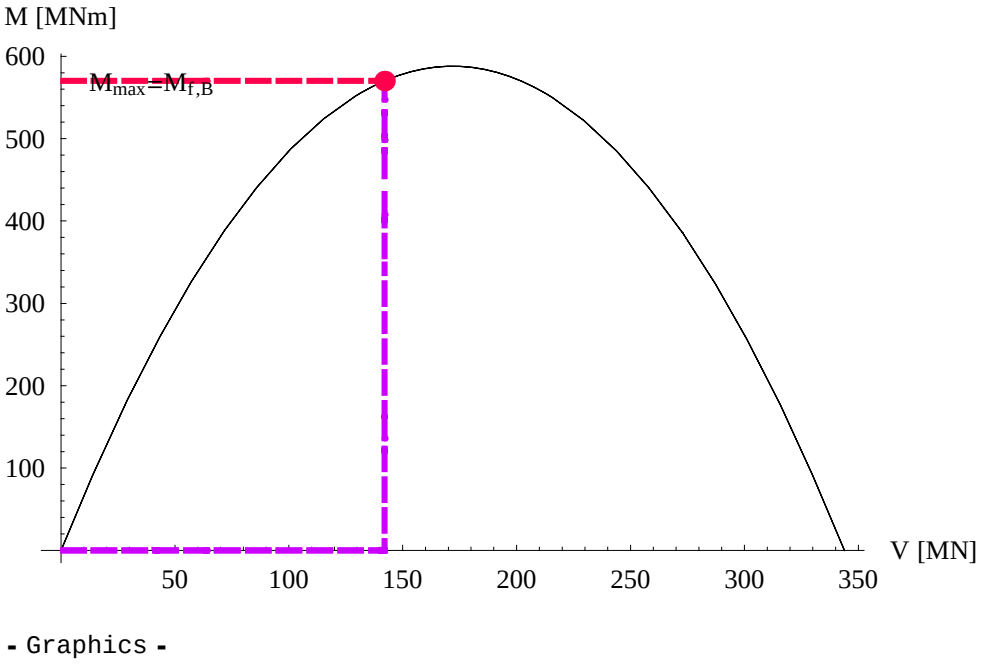

Figure 5 Bearing capacity failure in the *M-V* plane for the Pisa Tower

The values of $M_{\max}$ (=$M_{f,B}$ [MNm]) is:

```
MfB
```

```
570.164
```

This maximum value of the moment ($M_{f,B}$) corresponds to a rotation ($\theta_{f,B}$ [°]):

```
ϴfB
```

```
10.1795
```

Stability analysis - Stability of equilibrium

The equilibrium condition for an arbitrarily tilted tower can be derived by equating the external overturning (M_e=W h_G sinϑ) and resisting ($M_r(\vartheta\text{-}\vartheta_0)$) moments:

$$\mathrm{M_r}\,(\vartheta - \vartheta\mathrm{o}) = \mathrm{W}\,h_G\,\sin\vartheta$$

Assuming for small rotation θ, $\sin\theta \simeq \theta$ (in the case of a tower, for which 10° is already a very high inclination this assumption is clearly acceptable) and the resisting moment to be equal to the augmented exponential function ($M_r(\vartheta\text{-}\vartheta_0)$), which interpolates the results of the model, the equilibrium condition becomes:

$$\mathrm{p}\,[1 - e^{-(\mathrm{q}-\mathrm{r})\,(\vartheta-\vartheta\mathrm{o})}] + \mathrm{p\ r}\ (\vartheta - \vartheta\mathrm{o}) = \mathrm{W}\,h_G\,\vartheta$$

Following the strategy suggested by Cheney *et al*. (1991), the instability of equilibrium analysis can be performed as follows. The equilibrium condition has a graphical solution, given by the intersection between the M_r curve and the M_e line, as shown in Figure 6 for the case of the Pisa Tower. Equilibrium can occur at two points on the M_r curve, depending upon loading history. The first is a stable equilibrium because for small increase in θ, M_r rises faster than M_e. The second is unstable. The maximum value of M_e that can be resisted occurs when the M_e line is tangent to the M_r curve; the coordinates of the tangent point then define the critical condition for instability of equilibrium.

Cheney *et al*. (1991) suggested that the effect of progressive tilting can be considered as an increase in the θ_0 value with time, which cause a translation of the M_r curve in the M-θ plane. The value of θ_0 (= $\theta_{0,\mathrm{creep}} + \theta_{0,\mathrm{ini}}$) will then include not only the initial imperfection of the system ($\theta_{0,\mathrm{ini}}$) but also any additional rotations due to creep ($\theta_{0,\mathrm{creep}}$). It's important to note that the moment-rotation curve is not affected by the creep deformations. Therefore the effect of creep is to reduce the factor of safety with respect to critical initial angle θ_0.
Figure 6 (generated from the embedded code) shows the result of the stability analysis of the Pisa Tower in the M-θ plane, developed using the strain hardening plastic model. The curve calibration (based on the current value of rotation of the tower: θ=5.5°, which corresponds to an external moment M_e=308MNm) gave the estimated value of the initial rotation: θ_0=3,8°. The coordinates of the tangent point which define the critical condition for instability of equilibrium $M_{f,E}$ [MNm] and $\theta_{f,E}$ [°] are:

```
MfE
```

```
422.162
```

```
ϴfE
```

```
7.53712
```

```
Show[ Graphics[{PointSize[0.025], p1}], Meplot,
 Mrplot, PlotRange → {{0, 15}, {0, 600}}, Frame → True,
 GridLines → Automatic, AxesLabel → {"Θ [°]", "M[MNm]"},
 TextStyle → {FontFamily → "Times", FontSize → 10},
 Epilog → {{ Text["M [MNm]", {1.5, .5}, {0, -22},
     TextStyle → {FontFamily → "Times", FontSize → 10}],
    Text["Θ [°]", {20.5, .5}, {10, -1},
     TextStyle → {FontFamily → "Times", FontSize → 10}]}}]
```

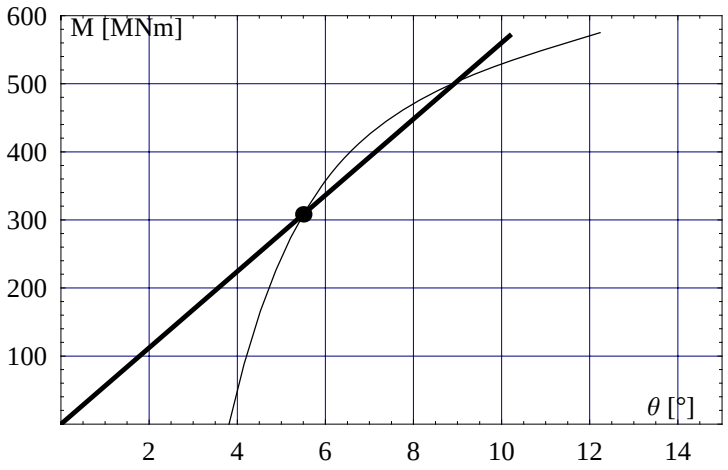

- Graphics -

```
Show[ Graphics[{PointSize[0.025], p1}],
 Graphics[{Hue[.6], PointSize[0.025], pfE}], MrplotfE,
 Meplot, Mrplot, PlotRange → {{0, 15}, {0, 600}},
 Frame → True, GridLines → Automatic,
 AxesLabel → {"Θ [°]", "M[MNm]"},
 TextStyle → {FontFamily → "Times", FontSize → 10},
 Epilog → {{Text["E", {7, .5}, {0, -13},
     TextStyle → {FontFamily → "Times", FontSize → 15,
       FontWeight -> "Bold", FontColor -> Hue[.6] }],
    Text["M [MNm]", {1.5, .5}, {0, -22},
     TextStyle → {FontFamily → "Times", FontSize → 10}],
    Text["Θ [°]", {20.5, .5}, {10, -1},
     TextStyle → {FontFamily → "Times", FontSize → 10}]}}]
```

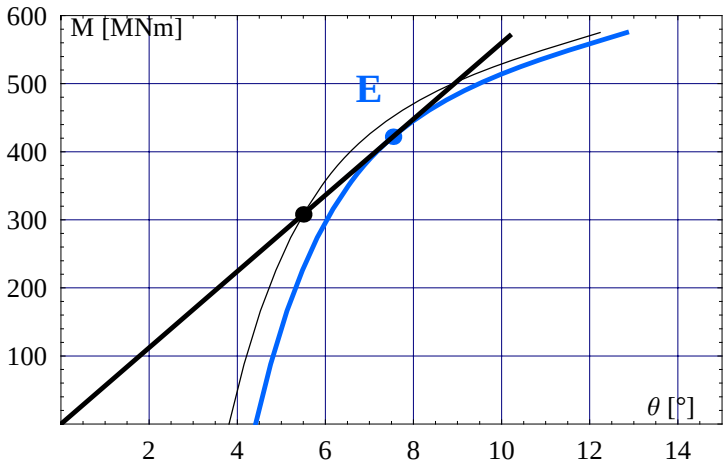


```
- Graphics -
```

Figure 6 Stability of equilibrium analysis of the Pisa Tower

Stability and strength analysis

The Stability and strength analysis of the Pisa Tower is shown in Figure 7. This figure combines both the collapse mechanisms of the foundation and clearly shows which one occurs first. In this case the stability of equilibrium failure (point E) occurs for rotations smaller than those necessary to reach bearing capacity failure (point B).

```
Show[ Meplot, VMbearcap, Graphics[{PointSize[0.025], p1}],
 Graphics[{Hue[.6], PointSize[0.025], pfE}],
 Graphics[{Hue[.95], PointSize[0.025], pMθbc}], MrplotfE,
 Mrplot, PlotRange → {{0, 15}, {0, 650}}, Frame → True,
 GridLines → Automatic, AxesLabel → {"θ [°]", "M[MNm]"},
 TextStyle → {FontFamily → "Times", FontSize → 10},
 Epilog → {{Text["E", {7, .5}, {0, -13},
     TextStyle → {FontFamily → "Times", FontSize → 15,
       FontWeight -> "Bold", FontColor -> Hue[.6] }],
    Text["B", {10, .5}, {0, -16}, TextStyle →
      {FontFamily → "Times", FontSize → 15,
       FontWeight -> "Bold", FontColor -> Hue[.95] }],
    Text["M [MNm]", {1.5, .5}, {0, -23},
     TextStyle → {FontFamily → "Times", FontSize → 10}],
    Text["θ [°]", {20.5, .5}, {10, -1},
     TextStyle → {FontFamily → "Times", FontSize → 10}]}}]
```

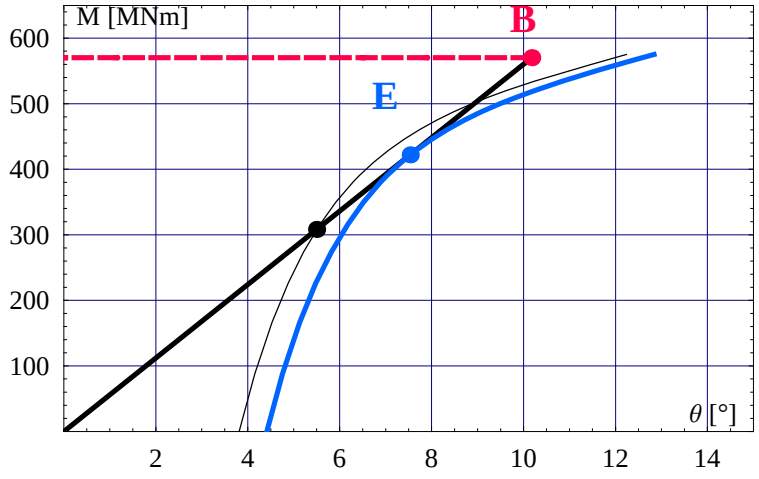


```
- Graphics -
```

Figure 7 Stability and strength analysis of the Pisa Tower

B.2 Santo Stefano bell tower *Notebook*

Stability and strength analysis of the Santo Stefano bell tower

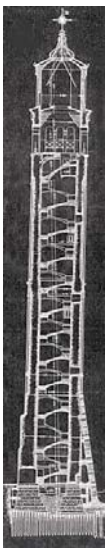

Introduction

— The following code performs a stability and strength analysis of the Santo Stefano bell tower: a bearing capacity analysis (foundation not strong enough) is coupled with one for instability of equilibrium (foundation not stiff enough). For the input data see Chapter 1, for the underlying theoretical analysis see Chapter 3 and Chapter 4 and for notebook instructions and discussion of results see Chapter 5 of the thesis.

CHARACTERISTICS OF THE TOWER

The characteristics of the Santo Stefano bell tower are extensively reported in Section 1.1, Chapter 1, and summarised below:

Properties

The height of the building from its foundations to the belfry is c.62m ($h_G \simeq$25m);
-The ring shaped foundation has an external width of 9m;
-The Tower weight c. 35 MN;

Rotations and Settlements

- The inclination measured in 2002 was 2.6°.
- The inclination measured in 1900 was 2.2° (before the buttresses construction).

Stratigraphy

- Between ground level and a depth of about 3,5 m: fill.
- Between 3.5m and circa 7.6m depth: soil composed primarily of silty clays (the foundation is posted at 4m depth, wooden pile are c. 2.5m long).
- Between 7.6m and circa 13m depth: soil composed primarily of silty sands with stratification with a prevalence of clayey-silts.

Buttresses carachteristics

The buttresses are 15 m long (15m/60m≃1/4 of the tower height), have a rectangular shaped concrete bed (4 m x 10 m) on piles, 3m long, which reach the sand layer.The buttresses of the foundation and the tower were intended to be rigidly connected but the in situ evidence shows that this was not completely achieved.

ANALYSIS OF THE ORIGINAL FOUNDATION 1450-1900

In 1904 Santo Stefano Bell Tower was reinforced constructing a system of buttresses. This Notebook performs the stability and strength analysis of the bell tower from its construction (in 1450) until the beginnig of the XX° century, before the buttresses construction. The analysis shows that, without the intervention, the bell tower would now be in a condition of incipient collapse.

Input parameters

Properties (geometry and weight of the foundation/tower)

WT: weight of the tower [MN];
h_G: height of the centre of gravity of the tower [m];
(2R): width of the foundation of the tower (*2R* is indicated by *RR* in the code) [m];
L: length of the foundation (*L>2R*) [m];
d: depth of the foundation (on the canal side) [m];
hw: depth of the water level (from the soil level) [m];

```
WT = 35; hG = 25; RR = 9; L = 9; d = 2.7; hw = 0;
```

Soil proprieties

ϕ: angle of friction (NB for the long term we must always take c'=0 kPa) [°];
γ_{sat}: saturated unit weight [kN/m^3];
γ_{dry}: dry unit weight [kN/m^3];
γ_w: water unit weight [kN/m^3];
C'0: compression parameter;
C'0/C'r: ratio between compression parameters;
n: parameter defined from the value of OCR at a known depth (Equation 3.14, Chapter 3);

```
ϕ = 27; γdry = 15; γsat = 20; γw = 10;
Co = .07; CoCrratio = 20 ; n = 20;
```

Hardening law

The hardening law for the Santo Stefano bell tower is developed in the embedded code (based on the methodology suggested in Chapter 3) and plotted in Figure 1. The solution from the code can be interpolated to provide the exponential expression below

$$V_0 = A\,(1 - e^{-B\,w_p})$$

```
Show[VowocurvePLOT, Vowoplot]
```

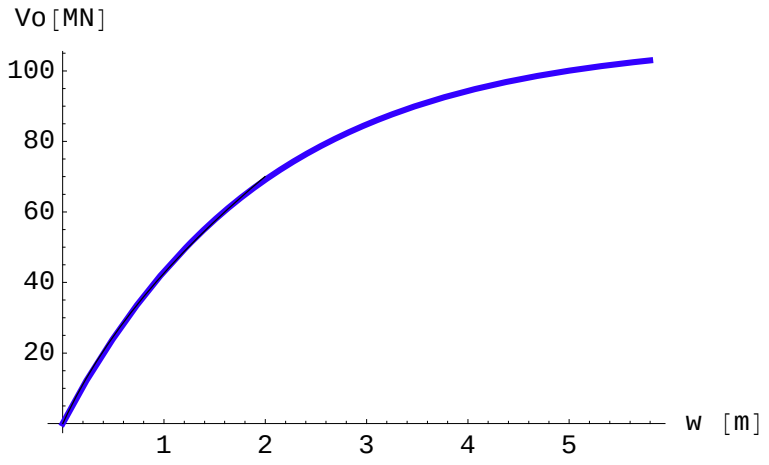


```
- Graphics -
```

Figure 1. Hardening law for the Santo Stefano bell tower.

The values of the parameters in V_0 equation are:

```
A
```

```
108.793
```

```
B
```

```
0.504433
```

The complete output of the model

The output of the strain hardening plastic model for surface foundations, which develops the M-θ curve, also provides the vertical settlement. Figure 2 shows the results of the model, from a V-w input, for a specific load path. A typical tower load path is characterized by the application of the weight (W) of the tower (at constant null moment) during construction followed by moment increments (δM= W·h·$\delta\theta$) under constant vertical load V=W.

The following code solves the model for the Santo Stefano bell tower, i. e. firstly the weight of the tower is applied (W=35 MN) at constant null moment (M=0), then the moment is increased incrementally (δM=W·h·$\delta\theta$), at constant V=W, up to bearing capacity failure.
As explained in Chapter 3 the equations of the model depend on the geometry of the system, the soil properties and, in particular, the vertical centreline load capacity of the soil-foundation system (V_{max}, calculated in the embedded code).

```
Show[GraphicsArray[{{VM, ∈Mp}, {wV, ∈wp}}],
 GraphicsSpacing → .005]
```

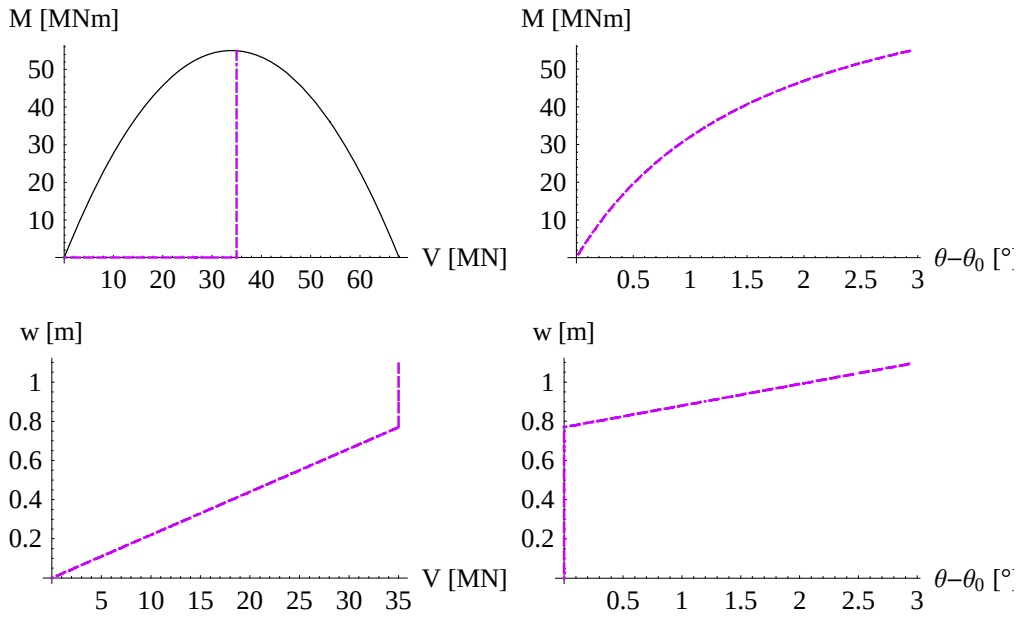


```
- GraphicsArray -
```

Figure 2 Complete output of the expanded (see Chapter 3) strain hardening plastic model for surface foundations, for the relevant Santo Stefano load-path.

M-θ curve

The M-θ curve has been deduced from the strain hardening plastic model for surface foundations, expanded as explained in Chapter 3. The rotational stiffness of a surface pad is *load path dependent*, consequently every specific load path generates a different curve. The output of the code is a numerical solution which can be interpolated to provide an augmented exponential expression:

$$M_r = p\,[1 - e^{-(q-r)(\vartheta-\vartheta_0)}] + p\,r\,(\vartheta - \vartheta_0)$$

The interpolating function for *M-θ* (Figure 3), from the numerical solution, is developed in the embedded code.

```
MΘPLOTModExp = Plot[ MΘcurveModExp[ΔΘ], {ΔΘ, Θini, Θpmax},
  AxesLabel → {"ΔΘ [°]", "M[MNm]"}, AxesOrigin → {0, 0},
  PlotStyle → {Hue[.95], Thickness[.01]}]
```

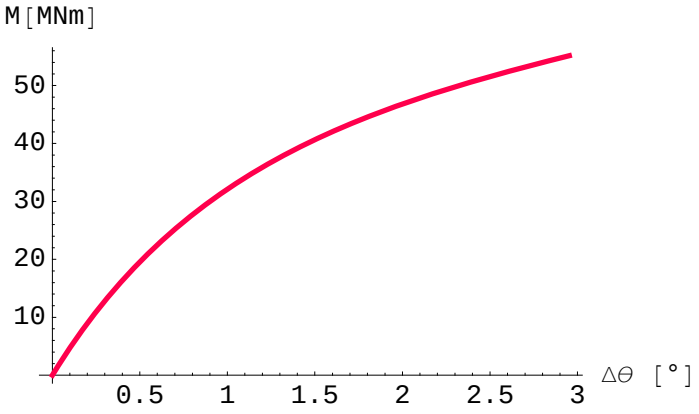


```
- Graphics -
```

Figure 3 M-θ curve for the Santo Stefano bell tower, from the strain hardening plastic model for surface pads.

The values of the parameters in M_r equation are:

```
p
```

```
40.3262
```

```
q
```

```
1.21194
```

```
r
```

```
0.138655
```

Note that the final curve (M-ϑ curve ≡ Mr: resisting moment developed by the foundation during the rotation) is a non-linear function of $\Delta\theta = \theta - \theta_0$. Figure 4 shows that ϑ is the total rotation of the foundation from the vertical position, ϑo is an initial imperfection (due to either eccentricity or initial inclination developed during construction) and not associated with the resisting moment, whereas $\Delta\theta = (\vartheta - \vartheta o)$ is the absolute rotation associated with the resisting moment.

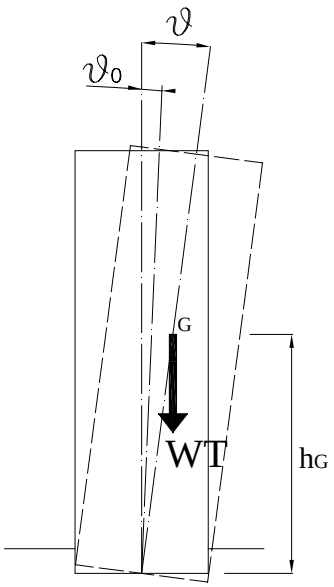

Figure 4 Sketch of a tower.

Strength analysis - Bearing capacity

The maximum moment, $M_{f,B}$ [MNm] (Figure 5) that the tower foundation can support, at constant vertical load (W) and H=0 is calculated in the embedded code.

```
VMbcap = Show[VMbearcap, parabolaVmax,  VM, VMini,
  Graphics[{Hue[.95], PointSize[0.025], pMVbc}],
  AxesLabel → {"V [MN]", "M [MNm]"},
  TextStyle → {FontFamily → "Times", FontSize → 10},
  Epilog → {Text["Mmax=Mf,B", {2, -0.1}, {-1, -25},
     TextStyle → {FontFamily → "Times", FontSize → 10}]}]
```

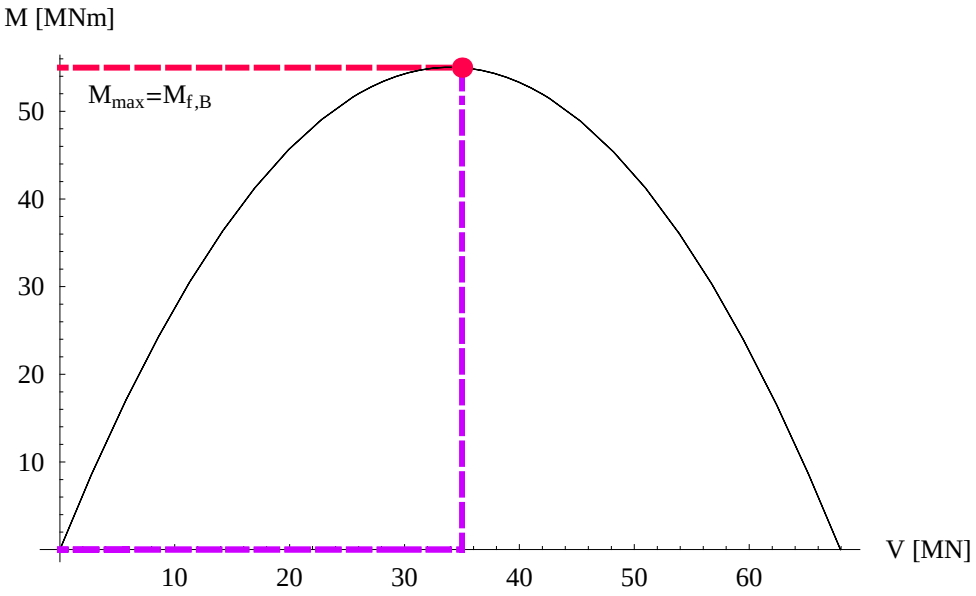


```
- Graphics -
```

Figure 5 Bearing capacity failure in the *M-V* plane for Santo Stefano

The values of $M_{\max}$ (=$M_{f,B}$ [MNm]) is:

```
MfB
```

```
54.9783
```

This maximum value of the moment ($M_{f,B}$) corresponds to a rotation ($\theta_{f,B}$ [°]):

```
ϴfB
```

```
3.60003
```

Stability analysis - Stability of equilibrium

The equilibrium condition for an arbitrarily tilted tower can be derived by equating the external overturning (M_e=W h_G sinϑ) and resisting ($M_r(\vartheta\text{-}\vartheta_0)$) moments:

$$\mathrm{M_r}\,(\vartheta - \vartheta\mathrm{o}) = \mathrm{W}\,h_G\,\sin\vartheta$$

Assuming for small rotation θ, $\sin\theta \simeq \theta$ (in the case of a tower, for which 10° is already a very high inclination this assumption is clearly acceptable) and the resisting moment to be equal to the augmented exponential function ($M_r(\vartheta\text{-}\vartheta_0)$), which interpolates the results of the model, the equilibrium condition becomes:

$$\mathrm{p}\,[1 - e^{-(\mathrm{q}-\mathrm{r})\,(\vartheta-\vartheta\mathrm{o})}] + \mathrm{p}\;\mathrm{r}\;(\vartheta - \vartheta\mathrm{o}) = \mathrm{W}\,h_G\,\vartheta$$

Following the strategy suggested by Cheney *et al*. (1991), the instability of equilibrium analysis can be performed as follows. The equilibrium condition has a graphical solution, given by the intersection between the M_r curve and the M_e line, as shown in Figure 6 for the case of the Santo Stefano bell tower. Equilibrium can occur at two points on the M_r curve, depending upon loading history. The first is a stable equilibrium because for small increase in θ, M_r rises faster than M_e. The second is unstable. The maximum value of M_e that can be resisted occurs when the M_e line is tangent to the M_r curve; the coordinates of the tangent point then define the critical condition for instability of equilibrium.

Cheney *et al*. (1991) suggested that the effect of progressive tilting can be considered as an increase in the θ_0 value with time, which cause a translation of the M_r curve in the M-θ plane. The value of θ_0 (= $\theta_{0,\mathrm{creep}} + \theta_{0,\mathrm{ini}}$) will then include not only the initial imperfection of the system ($\theta_{0,\mathrm{ini}}$) but also any additional rotations due to creep ($\theta_{0,\mathrm{creep}}$). It is important to note that the moment-rotation curve is not affected by the creep deformations. Therefore the effect of creep is to reduce the factor of safety with respect to critical initial angle θ_0.
Figure 6 (generated from the embedded code) shows the result of the stability analysis of the Santo Stefano bell tower in the M-θ plane, developed using the strain hardening plastic model. The curve calibration (based on the current value of rotation of the tower: θ=2.2°, which corresponds to an external moment M_e=33.6MNm) provided an estimate of the initial rotation: θ_0=1.1°. The coordinates of the tangent point which define the critical condition for instability of equilibrium $M_{f,E}$ [MNm] and $\theta_{f,E}$ [°] are:

```
MfE
```

```
39.1091
```

```
ϴfE
```

```
2.5609
```

```
Show[ Graphics[{PointSize[0.025], p1}], MrplotfE, Meplot,
 Mrplot, Graphics[{Hue[.6], PointSize[0.025], pfE}],
 PlotRange → {{0, 5}, {0, 65}}, Frame → True,
 GridLines → Automatic, AxesLabel → {"θ [°]", "M[MNm]"},
 TextStyle → {FontFamily → "Times", FontSize → 10},
 Epilog → {{Text["E", {2.35, 5}, {0, -10},
     TextStyle → {FontFamily → "Times", FontSize → 15,
       FontWeight -> "Bold", FontColor -> Hue[.6] }],
    Text["M [MNm]", {0.5, .4}, {-0.1, -23},
     TextStyle → {FontFamily → "Times", FontSize → 10}],
    Text["θ [°]", {6.75, 0.5}, {10, -1},
     TextStyle → {FontFamily → "Times", FontSize → 10}]}}]
```

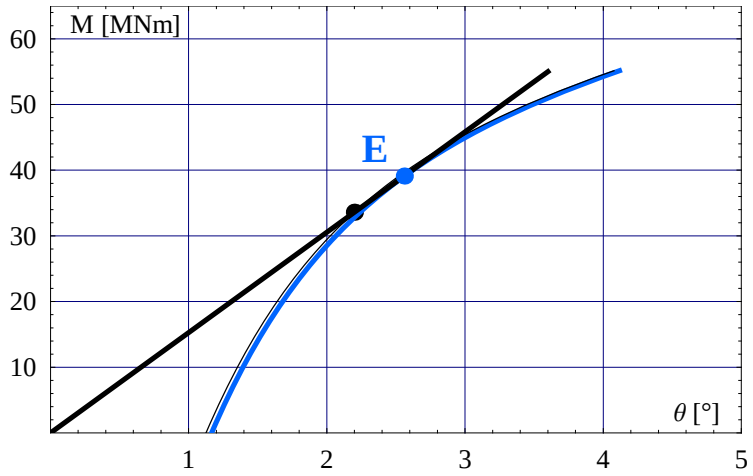


```
- Graphics -
```

Figure 6 Stability of equilibrium analysis of the Santo Stefano bell tower

Stability and strength analysis

The Stability and strength analysis of the Santo Stefano bell tower is shown in Figure 7. This figure combines both the collapse mechanisms of the foundation and clearly shows which one occurs first. In this case the stability of equilibrium failure (point E) occurs for rotations smaller than those necessary to reach bearing capacity failure (point B).

```
Show[ Meplot, VMbearcap, Graphics[{PointSize[0.025], p1}],
 Graphics[{Hue[.6], PointSize[0.025], pfE}],
 Graphics[{Hue[.95], PointSize[0.025], pMθbc}], MrplotfE,
 Mrplot, PlotRange → {{0, 5}, {0, 65}}, Frame → True,
 GridLines → Automatic, AxesLabel → {"θ [°]", "M[MNm]"},
 TextStyle → {FontFamily → "Times", FontSize → 10},
 Epilog → {{Text["E", {2.5, -3.5}, {0, -13},
     TextStyle → {FontFamily → "Times", FontSize → 15,
       FontWeight -> "Bold", FontColor -> Hue[.6] }],
    Text["B", {3.5, -1}, {0, -16}, TextStyle →
      {FontFamily → "Times", FontSize → 15,
       FontWeight -> "Bold", FontColor -> Hue[.95] }],
    Text["M [MNm]", {0.5, .4}, {0, -23},
     TextStyle → {FontFamily → "Times", FontSize → 10}],
    Text["θ [°]", {6.75, 0.5}, {10, -1},
     TextStyle → {FontFamily → "Times", FontSize → 10}]}}]
```

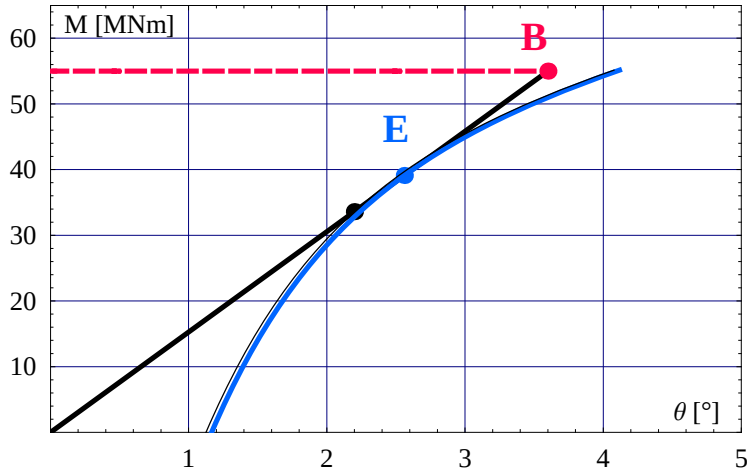

- Graphics -

Figure 7 Stability and strength analysis of the Santo Stefano bell tower